UNIVERSIDADE FEDERAL DO CEARÁ
CENTRO DE CIÊNCIAS
DEPARTAMENTO DE QUÍMICA ORGÂNICA E INORGÂNICA
PROGRAMA DE PÓS-GRADUAÇÃO EM QUÍMICA

CONCEIÇÃO REGINA FERNANDES ALVES

DEVELOPMENT OF CHITOSAN AND FLY ASH-BASED ZEOLITE COMPOSITES FOR WATER SOFTENING

FORTALEZA
2022

CONCEIÇÃO REGINA FERNANDES ALVES

DEVELOPMENT OF CHITOSAN AND FLY ASH-BASED ZEOLITE COMPOSITES FOR WATER SOFTENING

Dissertation presented to the Chemistry Post-Graduation Program of the Federal University of Ceará as a partial requirement to obtain the title of M.Sc. in Chemistry. Concentration area: Inorganic Chemistry.

Supervisor: Prof. Dr. Adonay Rodrigues Loiola

FORTALEZA

2022

Dados Internacionais de Catalogação na Publicação
Universidade Federal do Ceará
Biblioteca Universitária
Gerada automaticamente pelo módulo Catalog, mediante os dados fornecidos pelo(a) autor(a)

A478d Alves, Conceição Regina Fernandes.
Development of chitosan and fly ash-based zeolite composites for water softening / Conceição Regina Fernandes Alves. – 2022.
88 f. : il. color.

Dissertação (mestrado) – Universidade Federal do Ceará, Centro de Ciências, Programa de Pós-Graduação em Química, Fortaleza, 2022.
Orientação: Prof. Dr. Adonay Rodrigues Loiola.

1. Hard water. 2. Fly ash-based zeolite. 3. Chitosan. 4. Water softening. I. Título.

CDD 540

CONCEIÇÃO REGINA FERNANDES ALVES

DEVELOPMENT OF CHITOSAN AND FLY ASH-BASED ZEOLITE COMPOSITES FOR WATER SOFTENING

Dissertation presented to the Chemistry Post-Graduation Program of the Federal University of Ceará as a partial requirement to obtain the title of M.Sc. in Chemistry. Concentration area: Inorganic Chemistry.

Approved on: 04/02/2022.

EXAMINATORS

_____

Prof. Dr. Adonay Rodrigues Loiola (Supervisor)
Federal University of Ceará (UFC)

_____

Prof. Dra. Jeanny da Silva Maciel
Federal University of Ceará (UFC)

_____

Prof. Dr. Vinícius Patrício da Silva Caldeira
State University of Rio Grande do Norte (UERN)

To my beloved father, José, and mother, Regina (In memoriam).

To those who have always inspired me to move forward.

ACKNOWLEDGMENTS

Throughout the writing of this dissertation, I have received a great deal of support and assistance.

First, I would like to acknowledge the Coordenação de Aperfeiçoamento de Pessoal de Nível Superior – CAPES, for financing part of this study by the Finance Code 88887.372366/2019-00.

I would like to thank my supervisor, Dr. Adonay Loiola, whose expertise was fundamental in formulating the research questions. His insightful feedback motivated me to work harder to surpass all the difficulties, bringing this work to a higher level.

I would also like to thank the examination board, Dr. Vinícius Caldeira and Dr. Jeanny Maciel. I appreciate all the suggestions and new perspectives about the work.

I would like to acknowledge the assistance of Professor Ronaldo Nascimento, Professor José Sasaki, and Professor Felipe Bohn, for helping me in the characterization analyses.

To my colleagues at the Nanostructured Materials Laboratory, Armando Diego, Edipo Silva, Natália Porto, and Raquel Bessa, who always helped me creating new alternatives and to develop the research.

To my dear pupils Lara Ramos and Silvio Oliveira. Without the work of you two I would not finish this dissertation.

I am also grateful to Nadia Aline, Débora, Samuel, Natália, Ana Paula, Raquel, César, Iracema, Cristiano, Francisca, and Ravena, whose extended a great amount of assistance.

I am deeply grateful to all my friends, who helped me to keep moving forward and never giving up: Morgana, Janaine, Willan, Henrique, Allan, Michel, and Jonas.

I would also like to extend my deepest gratitude to Ingrid Azevedo, a friend who supported and motivated me to keep moving forward and has never doubted that I could accomplish whatever I try to do.

I am forever grateful to my lovely boyfriend, Victor Jucá. Without your love and support I would never be able to finish this work.

“A crítica válida presta um favor ao cientista.”
(SAGAN, CARL, 1995, p. 51).

RESUMO

Água dura é um termo utilizado para se referir a água com elevados teores de Ca^{2+} e Mg^{2+}. Em função principalmente da elevada capacidade de troca catiônica das zeólitas, esses materiais são amplamente utilizados como abrandadores de água. No entanto, restrições associadas à sua forma de pó, ou da forma compactada como pellets, fazem com que sua eficiência e reuso sejam comprometidos. Tais dificuldades podem ser superadas por meio da utilização de zeólitas apresentando estruturas hierarquizadas. O presente trabalho está centrado na obtenção de compósitos de zeólita NaA, com caráter magnético e não-magnético, e do biopolímero quitosana. A zeólita NaA foi sintetizada via rota hidrotérmica a partir de cinzas volantes oriundas da queima do carvão mineral, usadas como fonte principal de silício e alumínio. Os compósitos magnéticos e não magnéticos foram preparados por meio do gotejamento de solução de quitosana contendo a zeólita e/ou as partículas magnéticas, em solução coagulante básica. Os materiais obtidos foram caracterizados por meio das técnicas de difratometria de raios-X (DRX), espectroscopia de absorção na região do infravermelho (IV), microscopia de varredura eletrônica (MEV), análise termogravimétrica (TG) e magnetometria (VSM). Ensaios de abrandamento foram conduzidos por meio do contato de solução de Ca^{2+} 100 mg L^{-1} com diferentes massas de zeólita NaA. A produção dos materiais foi bem-sucedida, os compósitos tiveram as características da zeólita NaA preservada e boa dispersão dos cristais na matriz polimérica, assim como apresentam boa capacidade de remoção de íons Ca^{2+} do meio aquoso juntamente à facilidade de recuperação do material.

Palavras-chave: água dura; zeólita; quitosana; abrandamento.

ABSTRACT

Hard water is the denomination adopted to refer to the water with high Ca^{2+} and Mg^{2+} content. Due to the elevated cationic exchange capacity of zeolites, these materials are used as water softeners. However, restrains imposed from their powder form, and modified-packed form of pellets affects severely their efficiency in Ca^{2+} and Mg^{2+} capture. Such difficulty can be surpassed via the hierarchization of zeolitic structure. This work targets the production of magnetic and non-magnetic fly ash-based zeolite NaA composites using the biopolymer chitosan as matrix, and their application in water softening. The zeolite NaA was prepared using coal fly ashes as the main source of silicon and aluminum, via hydrothermal route synthesis. The magnetic and non-magnetic composites were prepared through the dripping of chitosan solution containing the zeolite NaA crystals, and/or magnetic particles from fly ashes into alkaline coagulant solution to obtain the beads The obtained materials were characterized using X-ray diffractometry (XRD), Fourier-transform infrared spectroscopy (FTIR), scanning electron microscopy (SEM), thermogravimetric analysis (TGA), and magnetometry (VSM). Water softening tests were performed by the contact of the materials with aliquots of Ca^{2+} solution at a concentration of 100 ppm. The characterization indicates the well succeeded synthesis of fly ash-based zeolite NaA, with the effective preparation of the composites. The softening tests showed the complete removal of Ca^{2+} from the aqueous media, confirming great potential of these material in water treatment.

Keywords: hard water; fly ash-based zeolite; chitosan; water softening.

LIST OF FIGURES

LIST OF TABLES

LIST OF ABBREVIATION AND SYMBOLS

CCSB	Cross-linked beads of chitosan with glutaraldehyde
CS	Chitosan
CSB	Beads of chitosan
D4R	Double 4-ring
DQAFQ	Analytical Chemistry and Physical Chemistry Department
DQOI	Organic and Inorganic Department
EDS	Energy-dispersive X-ray spectroscopy
FA	Fly-ash
FTIR	Fourier-transform infrared spectroscopy
GA	Glutaraldehyde
HF	Heavy fraction
ICSD	Inorganic Crystal Structure Database
LabPOA	Advanced Oxidative Processes Laboratory
LabPol	Polymers Laboratory
LRX	X-Ray Laboratory
LTA	Linde Type-A
MF	Magnetic Fraction
NMF	Non-Magnetic Fraction
PBU	Primary Building Unit
RO	Reverse Osmosis
SBU	Secondary Building Unit
SEM	Scanning Electron Microscopy
TGA	Thermogravimetric Analysis
UFC	Federal University of Ceará
VSM	Vibrating sample magnetometry
WSS	Water-soluble salts
XRF	X-ray fluorescence
ZA	Zeolite NaA

SUMMARY

1 INTRODUCTION

1.1 Water

Water is a remarkable, versatile substance, omnipresent in everything we produce, considered therefore the base of life.[1-3] Unfortunately, several anthropogenic environmental changes, including the expansion of urban areas, have transformed the demand for quality water in one of the greatest challenge of the modern society.[4-6] Although water is abundant on Earth, covering about 73% of its surface, only 3% of the hydrosphere is freshwater, occurring naturally in lakes, rivers, or underground.[7] Groundwater is the water that infiltrates into the ground through porous materials, filling pores and fractures, forming the aquifers.[8] It is one of the major freshwater suppliers worldwide, responsible for the drinking water access of nearly 33% of the world's population.[9; 10] Furthermore, different sectors such as industrial, agricultural, urbanization, food and energy security, environmental sustainability, and health are directly and highly dependent on water.[11] Thus, actions aiming at sustainable groundwater management have become extremely important.

1.1.1 Mineral composition of water

The mineral composition of water changes according to its source, the lithology of its origin region, and the interactions within the aquifer between chemical constituents, soil, rock, and gases.[12; 13] The imprudent exploitation of groundwater affects hydrodynamic and hydro-geochemical conditions of the aquifers, which cause an increase in the dissolution of salts.[14; 15]

Hard water is an environmental problem in different countries around the globe,[16; 17] and it depends on the concentration of dissolved cations, mainly calcium (Ca^{2+}) and magnesium (Mg^{2+}), in the medium.[18-20] The presence of calcium and magnesium ions dissolved in water is related to several problems such as corrosion and scaling.[21; 22] Table 1 presents the classification of water in terms of calcium carbonate ($CaCO_3$) equivalent.[23; 24]

Table 1 – Classification of water according to its hardness in function of $CaCO_3$ equivalent.

Classification of Water	$CaCO_3$ / mg L^{-1}
Soft	0 – 50
Moderately soft	50 – 100
Slightly hard	100 – 150
Moderately hard	150 – 200
Hard	200 – 300
Very hard	> 300

Source: Al-Hadidi, et al.[23]

Among the existent hard water treatment techniques, desalination is widely accepted as a viable technology of producing freshwater from saline water (seawater or underground brackish water) for drinking, agricultural, and industrial purposes,[25; 26] and has been practiced in over 150 countries around the world.[27]

1.1.2 Hard water treatment

The process of reducing the hardness of water is called softening.[28] Considering the importance to ensure an environmentally sustainable drinking water production and distribution in a cost-effective manner,[29] several water softening technologies are available and they vary in terms of hardness reduction, water consumption, maintenance requirements, residue production, and costs.[30] Table 2 exhibits a few of the technologies adopted in water softening process with some of their advantages and disadvantages.

One of the main processes for water softening is reverse osmosis (RO), which is adopted in about 80% of the total desalination plants for its high selectivity.[31; 32] However, the RO technology This technology when applied in the desalination of brackish waters is limited by salt scaling that causes membrane fouling, reducing the permeate flux and the membrane lifespan.[33] but there are disadvantages on its use such as these ions can precipitate as carbonates on the surface of the membrane, causing the fouling phenomena, and consequently, the water permeation capacity declines, decreasing the membrane lifespan and increasing the water treatment costs.[32; 34; 35]

In order to mitigate this problem, auxiliary processes that can improve the desalination performance including water softening and salt removal as a viable steps in desalination process.[25; 29] To overcome the difficulties related to RO membranes, new materials are being explored to increase the efficiency and accessibility of desalination processes.[17; 36]

Table 2 – Advantages and disadvantages of the main water softening techniques.

Softening method	Advantages	Disadvantages	References
Chemical precipitation	• Environmental compatibility; • Convenient operation; • High efficiency treatment.	• Waste production; • High equipment costs; • Demands plenty of chemical agents; • Production of large volume of sludge;	[20; 37-40]
Chemical reduction	• Superior selectivity when compared to conventional technology; • Applicable in a wide range of temperatures; • Moderate costs.	• Electrode deactivation. • Difficulty in operation control; • Possible catalyst fouling; • Sensitivity of the process to environmental conditions; • This process is limited due to the large amounts of waste sludge being produced; • High process cost; • Post-treatment needed.	[41; 42]
Flocculation	• High efficiency; • Simple technique.	• High costs; • Strict pH interval; • Temperature sensitivity; • Excessive sludge production.	[43; 44]
Ion exchange	• Fast, simple and economic process; • Ca^{2+} selectivity; • Low operational cost.	• High concentration of Na^{+}; • Further contaminant treatment is required.	[20; 25; 30; 45]
Membrane softening	• Highly effective method.	• Membrane fouling; • Elevated operational costs.	[20; 25; 46; 47]

Source: The author (2022).

1.2 Porous materials

Porous materials portray significant roles in our daily activities, being employed in important processes in many different fields including catalysis, separation, biomedicine, energy, insulation, and sensors.[48-50] Such versatility is result of the presence of voids, or pores, within their structure. that provides them different properties.[51-53] Given that the performance of these materials can be affected by pore characteristics, for instance pore size and distribution,[49] the development of advanced porous materials with well-defined structures has become a subject of scientific research.[54; 55]

The International Union of Pure and Applied Chemistry (IUPAC) categorizes the porous materials in three groups based on their pore diameter: macropore, porous size bigger than 50 nm, mesopore, porous size between 2 – 50 nm, and micropore, porous size smaller than 2 nm.[56; 57] The latter presents a subclassification, ultramicropores, to define materials with pore size smaller than 0.7 nm, and supermicropores for materials with pore size between 0.7 – 2.0 nm. Figure 1 presents a schematic representation in which the pore size of the three porous groups is compared.

Figure 1 – Schematic representation of pore size comparison: (a) synthetic porous materials with different classes of pore size, and (b) examples of structures with compatible dimensions of the porous materials.

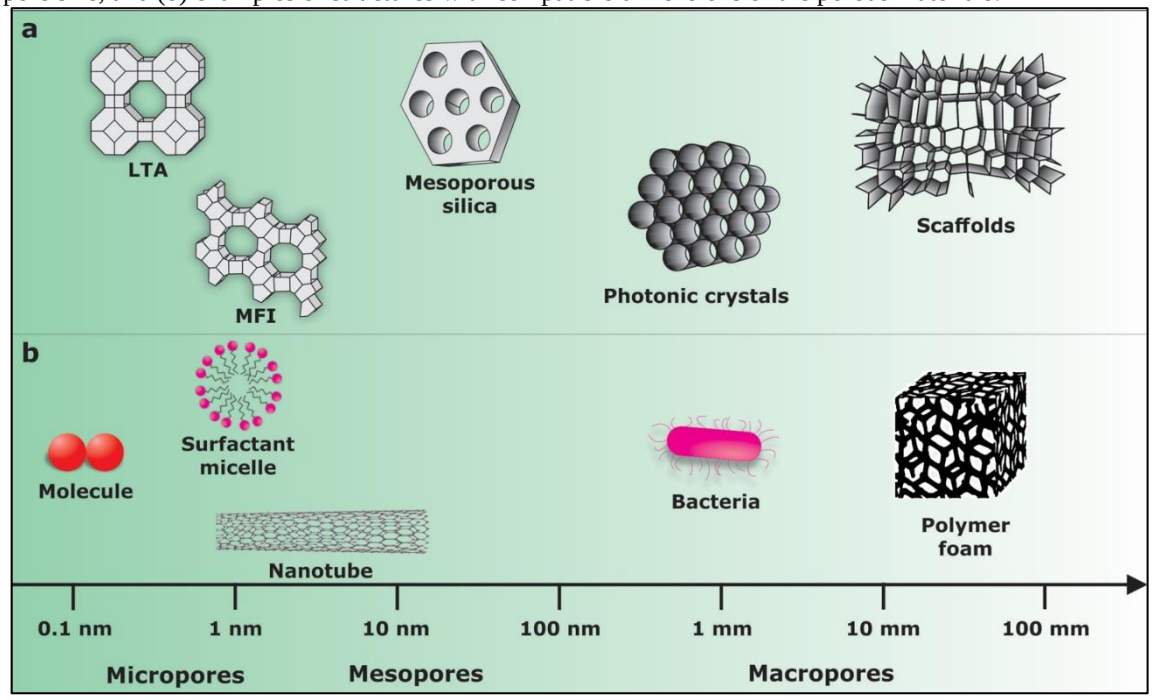

Source: The author (2022).

Nowadays, the syntheses of microporous materials can be carried out by means of a myriad of chemical and physicochemical strategies in order to obtain tailored materials, with

regular porosity, such as zeolites.[58] Zeolites are porous and crystalline aluminosilicates that either occur naturally or can be synthesized.[59] These materials have great potential as water softeners due to their unique properties like elevated porosity, high selectivity, high specific surface area, molecular sieving behavior, mechanical and thermal resistance, and ion exchange capacity.[60]

1.3 Zeolites

In 1756, the Swedish mineralogist Axel Fredrik Cronstedt discovered the first zeolite mineral, stilbite.[61-66] Due to their intumescence when heated, Cronstedt gave the name zeolite to these materials, from the Greek ζέω (zéō), meaning "to boil" and λίθος (líthos), meaning "stone", therefore “boiling stone”.[61-63]

Zeolites are hydrated crystalline inorganic polymers constituted by TO_4 (T = Si or Al) tetrahedra linked to each other by the oxygen atoms, forming a three-dimensional framework.[67; 68] Due to the trivalence nature of aluminum ion, each AlO_4 tetrahedron present in the zeolitic framework produces a negative charge in the structure which is balanced by an extra-framework cation[63] to maintain the material charge neutrality.[64; 69] The generic chemical composition for the unit cell of zeolites is presented in Equation 1, and their generic structure is represented in Figure 2.

Equation 1 – General empirical formula of zeolite unit cell.[63]

$$M_{\frac{y}{m}}\left[(SiO_2)_x(AlO_2)_y\right] \cdot wH_2O$$

where **M** is the metallic — commonly alkaline (group 1) or alkaline earth (group 2) cations, although organic cations can be used — that counterbalances the negative charges in the zeolite structure, **m** is the cation charge, **w** is the number of water molecules contained in the unit cell, and **x** and **y** are the numbers of tetrahedra per unit cell and they depend on the zeolite type.[63; 64]

Figure 2 – Generic chemical structure of zeolites in which it is possible to observe Si and Al tetrahedra intercalation. The presence of Al atoms in the center of tetrahedra creates areas of electronic density concentration, therefore the presence of compensation cations is required to obtain electronic neutrality.

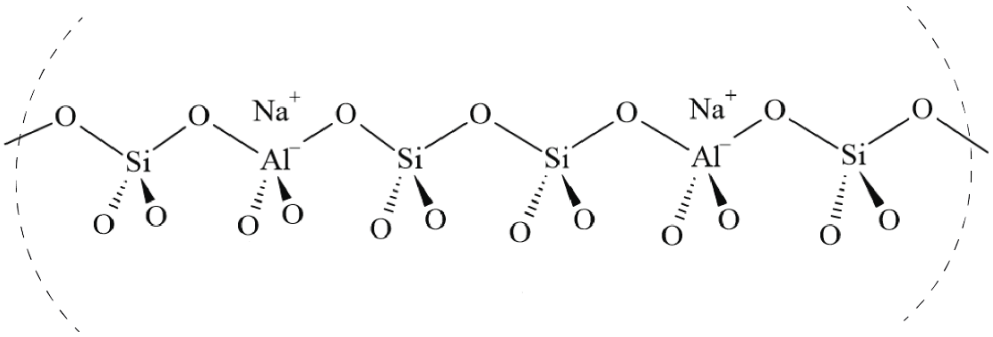

Source: The author (2022).

1.3.1 Building units

The primary building units (PBUs) in zeolitic structure is considered to be the TO_4 tetrahedra (T = Al or Si),[62; 63] these PBUs when assembled generates the secondary building units (SBUs). The framework structure of zeolite contains intracrystalline channels, formed by the covalent oxides of Al and Si, that are occupied by cations and water molecules. [70; 71]

Figure 3 – Representation of zeolite A unit cell. In orange the sodalite unit, in green the double 4-ring unit (D4R), and in blue the super cage formed by the assemble of eight sodalite units and twelve D4R units.

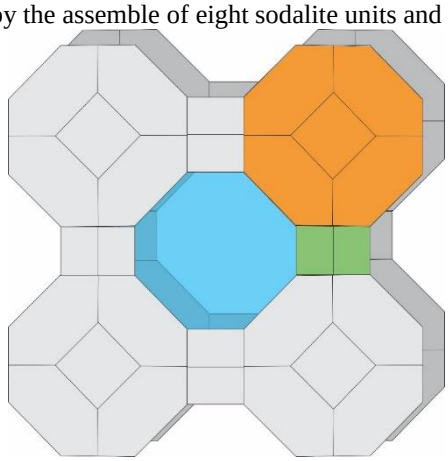

Source: The author (2022).

1.3.2 Syntheses of zeolitic materials

Although natural zeolites, such as clinoptilolite and chabazite, are widely adopted in environmental protection,[72] synthetic zeolites offer advantages when compared to them, once they tend to present higher crystallinity and homogeneous particle size distribution.[73]

Crystalline zeolites are can be synthesized via hydro/solvothermal methods under the appropriated conditions of time, temperature, type of mineralizing agent, source of silicon and aluminum, structure-directing agents (SDAs), etc.[74] Alternative routes of syntheses can include the integral or partial reuse of industrial waste, lowering the extraction of raw material

and the environmental liability deposited.[75] Environmental friendly syntheses of zeolites concerning a waste to resource strategy have been widely reported[76-78] using different sources of silicon and aluminum, such as rice husk ash,[79; 80] fly ashes,[81-84] kaolin,[85-87] diatomite,[88] sand and aluminum cans.[89]

Among the residues with economic and technological potential are the ones from thermoelectric plants, such as coal fly ash, which is a solid waste that is classified as a world-class problem.[90] If the coal fly ash is randomly stacked, serious problems related to soil, water and atmosphere pollution. With these problems in mind, it is necessary to develop a strategy to obtain high value-added applications for this waste, for example, the coal fly ash can be used as a source of alumina and silica for the synthesis of geopolymers and zeolites.[90]

1.3.3 Properties

The properties of zeolites make them attractive for various applications, such as water desalination and treatment,[25] catalysis,[67] molecular sieving,[91] and adsorption.[80; 91; 92]. Hence, the research on development of zeolitic materials aims the preparation of crystalline samples with well-defined characteristics according to their applications, some of the tailored characteristics are pore size, acidity, zeolite confinement effects, hydrothermal stability, and surface area.[68; 93]

High porosity as well as high active surface area have led to development of zeolites for

Considering the water softening process, zeolitic materials are promising agents[94] due to their high porosity, high surface area, and the presence of extra-framework cations (Figure 2). These characteristics potentialize the ion exchange property of zeolite.[68]

1.4 Hierarchical composites

The inherent microporosity of zeolites can result in limitations related to the diffusion of molecules and ions in active sites, what increases the difficulty of mass transfer in this type of material.[17; 67] The modification of the material by adding a second class of porosity can result in a distinctive structure, suitable to overcome limited access to active sites which helps to accelerate the diffusion,[95; 96] the combination of different degrees of porosity originating a hierarchical porous material is desirable to optimize the performance.[97] Different methods to introduce a secondary porosity have been reported,[97; 98] one strategy is to incorporate crystals of zeolite into a support, which can be inorganic, such as mineral fibers,[99; 100] or organic, like cellulose,[101-103] and chitosan.[104-107]

Biopolymeric materials are naturally occurring polymers that can be applied in different situations due to their unique properties, such as biodegradability, biocompatibility, non-toxicity, renewable and low price.[104; 108]

Figure 4 – Schematic representation of a generic hierarchical composite consisting of zeolitic crystals (green cubes – reinforcement phase) supported by polymeric fibers (blue – matrix phase), the interaction existent between matrix and reinforcement phases is physical.

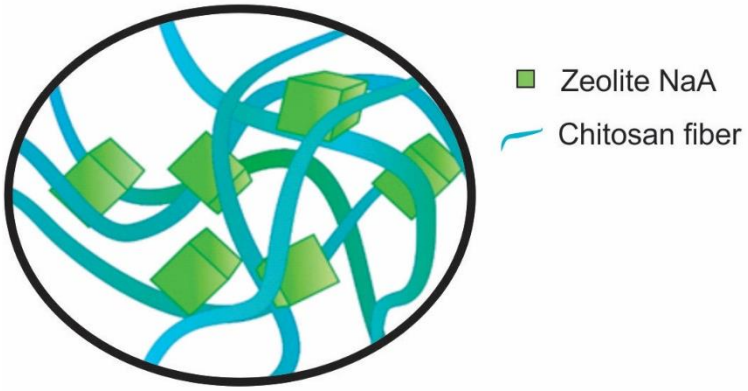

Source: The author (2022).

1.5 Chitosan

Chitosan is obtained via alkaline deacetylation of chitin, the second most common biopolymer found in crustaceans, insects, mollusks, and fungi,[109-111] and displays great advantages since it is a renewable, environmentally-safe, cost-effective, non-toxic, and biocompatible material.[112-115] Chitosan is a semi-crystalline, linear (1→4)-linked copolymer constituted by 2-amino-2-deoxy-β-D-glucopyranose and 2-acetamido-2-deoxy-β-D-glucopyranose units,[111; 116-118] and its chemical structure is presented in Figure 5.

Figure 5 – Representation of the chemical structure of chitosan consisting of β-1→4 linked D-glucosamine units (in red), and the N-acetyl-D-glucosamine unit (in blue).

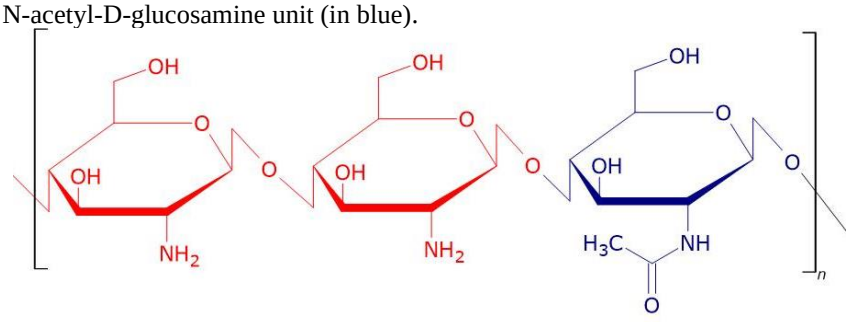

Source: The author (2022).

It is possible to observe in Figure 5 the presence of amino and hydroxyl groups in chitosan structure, which gives interesting properties to this material such as viscosity, solubility, swelling, and porosity,[113] making it suitable to a myriad of applications.[119]

Chitosan gelling properties allow it to be shaped as films, nanofibers, nanoparticles, nanocapsules, membranes, scaffolds, and hydrogels, according to its use therefore, this polymer is a suitable candidate as a matrix in composites with zeolites.[113; 114] Although chitosan is a versatile material and presents great potential and advantages, it is a compound with low mechanical strength, low thermal stability, and low porosity, therefore, modifications to improve chitosan properties are needed. Amongst the possible modification cross-linking is widely used,[120] and glutaraldehyde is one of the most used materials for this purpose, where it is used to obtain covalent cross-linked chitosan materials.[115]

Chemically cross-linked chitosan materials are based on the formation of an inter-chain covalent bonds network and characterized by high mechanical stability

Figure 6 – Representation of cross-linking reaction of glutaraldehyde and chitosan.

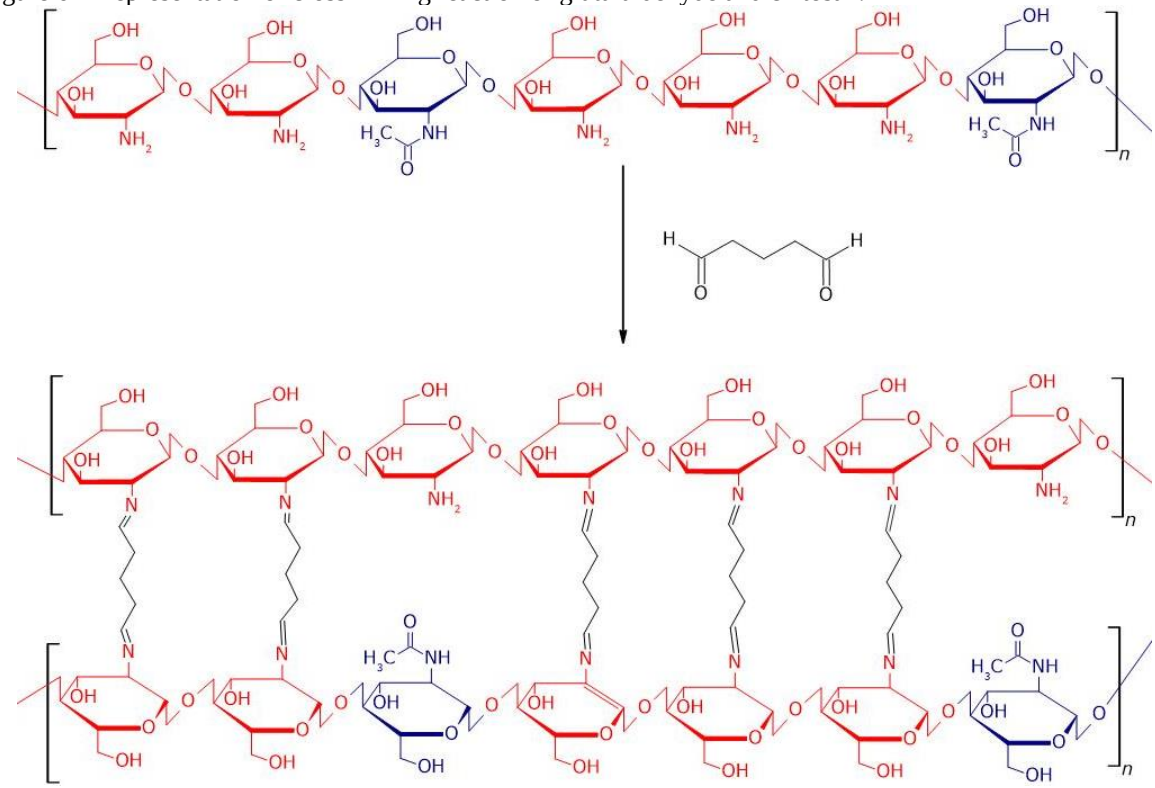

Source: The author (2022).

In this context, this research aims to present a suitable method for the preparation of magnetic and non-magnetic chitosan-supported fly ash-based zeolite NaA composites and to evaluate their effectiveness on water softening process.

2 OBJECTIVES

2.1 General objective

To produce composites of chitosan and zeolite NaA, synthesized from coal fly ashes as start material, and evaluate their capacity in Ca^{2+} removal from aqueous media.

2.2 Specific objectives

- To employ coal fly ashes as an alternative source of silicon for the efficient synthesis of zeolite NaA via hydrothermal route.
- To develop porous and homogeneous chitosan/zeolite NaA beads;
- To develop magnetic, porous, and homogeneous chitosan/zeolite NaA beads;
- To assess the performance of the obtained materials in Ca^{2+} removal from aqueous media, considering the influence of contact time and mass of the cation exchangers.

3 EXPERIMENTAL

Zeolite NaA was prepared via hydrothermal synthesis, and it was used to produce chitosan-supported porous composites shaped as beads. The prepared materials were characterized by employing different techniques to assess their structural, spectroscopic, and morphological properties. These materials were applied for water softening processes, in which their performance was evaluated by considering zeolite mass in the sample. In this section, the experimental procedures are presented in detail.

3.1 Reagents

Coal fly ash (FA) used in this study was supplied by the EDP group – Pecém II thermal power plant, located in São Gonçalo do Amarante, Ceará, Brazil. Chitosan (molecular weight = 1.29×10^6 g mol^{-1}, degree of deacetylation = 76.0%) was supplied by Polymar. The samples were collected from the thermoelectric sleeve filter. The other reagents used are listed in Table 3.

Table 3 – Reagents used in the preparation of the materials.

Name	Chemical formula	Purity / %	Supplier
Glutaraldehyde	$C_5H_8O_2$	25.0	Vetec
Acetic acid	$C_2H_4CO_2$	≥ 99.7	Synth
Calcium chloride	$CaCl_2$	≥ 96.0	Vetec
Ethanol	CH_3CH_2OH	≥ 95.0	Neon
Propanone	C_3H_6O	≥ 99.5	Dinâmica
Magnesium chloride hexahydrate	$MgCl_2 \cdot 6H_2O$	99 – 102	Vetec
Methanol	CH_4O	≥ 99.8	Êxodo Científica
Sodium aluminate	$NaAlO_2$	40 – 45	Sigma-Aldrich
Sodium hydroxide	NaOH	≥ 97.0	Neon

Source: The author (2022).

3.2 Fly ash treatment

FA underwent a sequence of treatments to remove impurities, following the methodology described by Amoni, et al.[121] First, FA had the granulometry homogenized using a 200 mesh sieve (74 μm). Then, 150.0 g of FA was transferred to a 2 L beaker containing 1.5 L of distilled water. The mixture was stirred mechanically for 1 h at room temperature (30 °C), and then kept under static condition for 24 h.

As a result, three fractions were identified: the light fraction (LF), which was concentrated on the mixture surface, the fraction containing water soluble salts (WSS) was obtained after the evaporation of the aqueous phase, and the heavy fraction (HF), deposited on the bottom. HF underwent a treatment, consisting of magnetic separation, which gave rise to two other fractions: the magnetic fraction (MF) and the non-magnetic fraction (NMF). The experimental sequence is depicted in Figure 7.

Figure 7 – Flowchart describing the fly ashes (FA) treatment, forming different fractions: water-soluble salts (WSS), light fraction (LF), and heavy fraction (HF). The magnetic extraction of HF produces the magnetic fraction (MF) and the non-magnetic fraction (NMF).

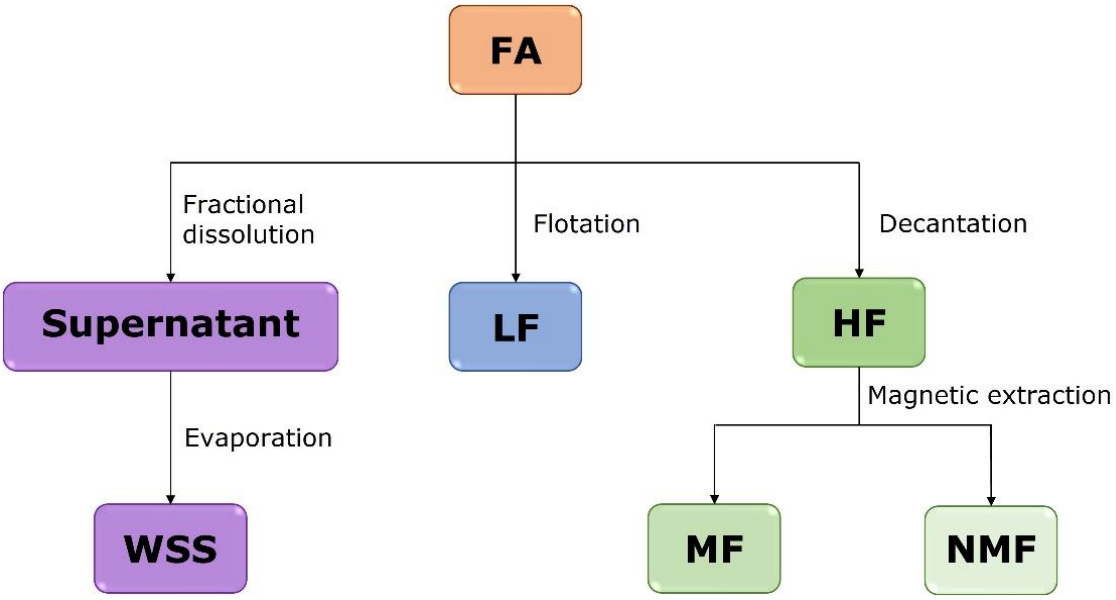

Source: The author (2022).

3.3 Synthesis of fly ash-based zeolite NaA

The synthesis of fly ash-based zeolite NaA (ZA) was carried out using the NMF as silicon source and as the main aluminum source. A hydrothermal route, based on the procedure described by Hui and Chao[81], was used.

Figure 8 – Schematic representation of the procedure to synthesize zeolite NaA using the fly ash non-magnetic fraction as the source of silicon.

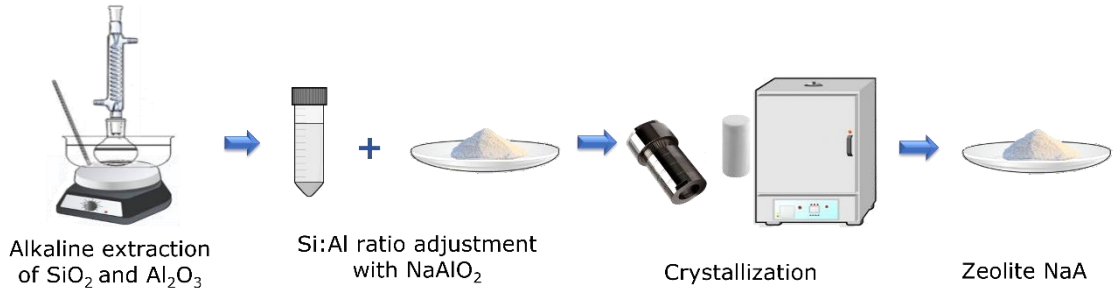

Source: The author (2022).

The extraction of Si and Al was performed in a closed flat-bottom flask, where 10.0 g of NMF sample was added to 65.5 mL of NaOH 4.3 mol L^{-1}. The mixture was heated at 90 °C in glycerin bath for 1 h under magnetic stirring (2,000 rpm). Then, the mixture was vacuum filtered, and to the supernatant, containing the extracted Si and Al, 1.34 g of $NaAlO_2$ was added, followed by the addition of NaOH 4.3 mol L^{-1} to a final volume of 65.5 mL. The reactional mixture formed a thick white gel, with molar composition consistent with the one commonly employed for the synthesis of the zeolite 4A, as indicated in Equation 2 – Batch molar composition for zeolite 4A synthesis [122].

Equation 2 – Batch molar composition for zeolite 4A synthesis [122].

$$3{,}165\ Na_2O : Al_2O_3 : 1{,}926 SiO_2 : 128 H_2O$$

The gel was transferred to a Teflon-lined reactor (Figure 9a) and attached to a stainless-steel autoclave (Figure 9b) and heated to 90 °C for 4 h. After cooling, the mixture was vacuum filtered and the solid was washed with distilled water until pH = 8.0, and then oven-dried at 90 °C, overnight. The granulometry was standardized in 200 mesh (74 µm).

Figure 9 – Photographs of (a) the Teflon-lined reactor used in the hydrothermal synthesis of zeolite NaA and (b) the stainless-steel autoclave.

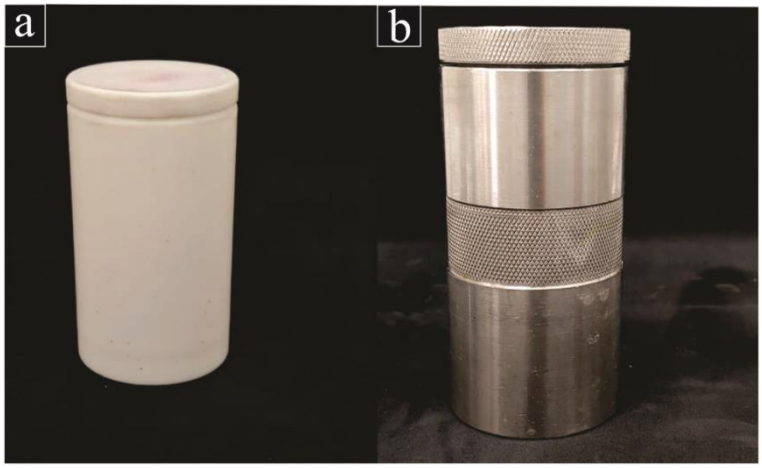

Source: The author (2022).

The synthetic route of zeolite NaA from FA as alternative source of Si and Al is shown in the flowchart in Figure 10.

Figure 10 – Flowchart of the fly ash-based zeolite NaA (ZA) synthesized from the non-magnetic fraction of fly ashes (NMF) as the only source of silicon.

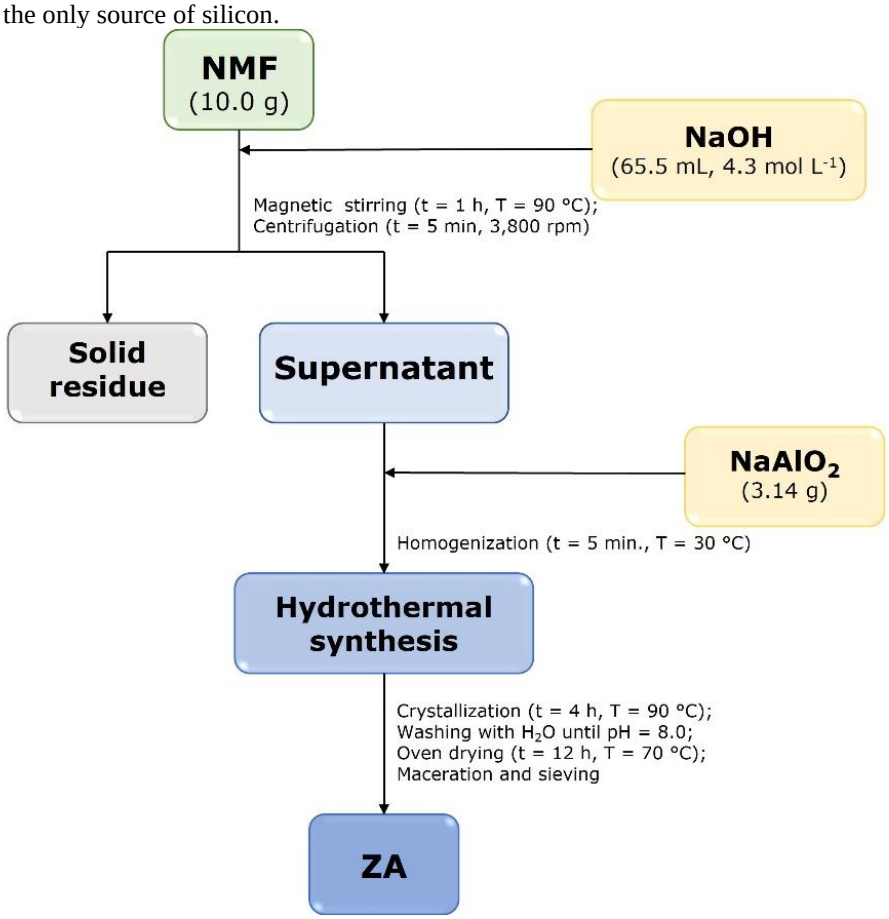

Source: The author (2022).

3.4 Chitosan materials

3.4.1 Chitosan purification

Chitosan was purified following the methodology described by Nasti et al. [123] with adaptation. 5.00 g of chitosan powder was dissolved in 400.0 mL of CH_3COOH 1.0% (v/v), in a 600 mL beaker, using a mechanical stirrer for 24 h. Then, the solution was heated to 95 °C for 15 min, for precipitation of impurities. The mixture was centrifuged for 5 min at 3,500 rpm and the supernatant collected. Chitosan was precipitated by pH adjustment to 9.0, with NaOH 1.0 mol L^{-1}.

Finally, the purified chitosan was washed with distilled water until pH = 7.0 and the solvent was exchanged by propanone. The chitosan was air-dried, macerated, and then stored in desiccator. The chitosan purification procedure is schematized in the flowchart presented in Figure 11.

Figure 11 – Flowchart of chitosan purification procedure.

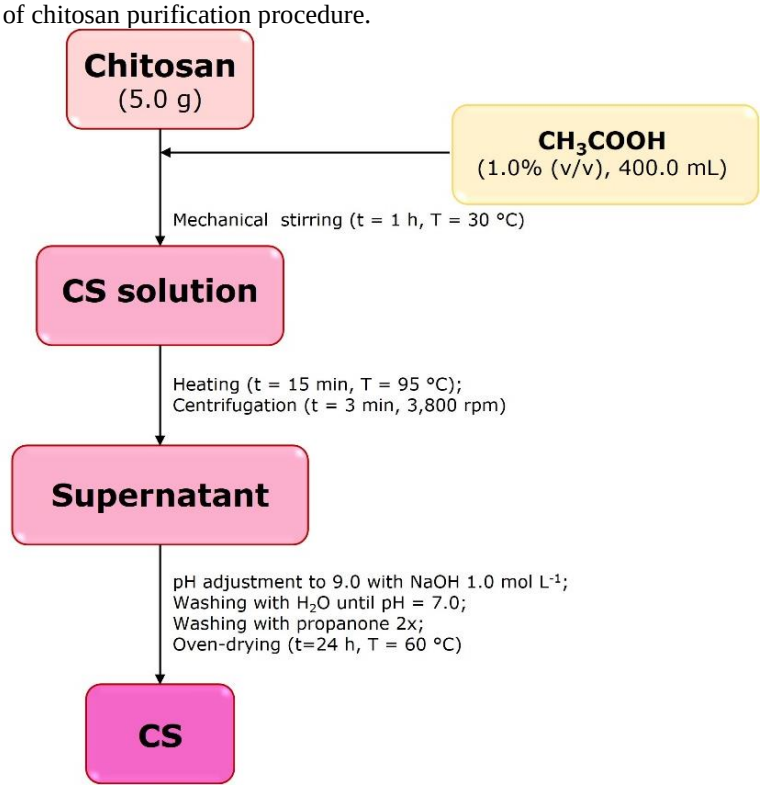

Source: The author (2022).

3.4.2 Preparation of pure chitosan beads (CSB)

The production of chitosan beads followed the methodology of Song, et al.[124] with adaptation. In a 250 mL beaker, 3.003 g of purified chitosan (CS) was dissolved in 100.0 mL of CH_3COOH 1.0% (v/v) using mechanical stirring for 24 h, at room temperature (32 °C), originating a solution of chitosan 3.0% (m/v). Then, the solution was added dropwise using a peristaltic pump Micronal B332, Tygon tube and a needle 18G, into a coagulant solution of NaOH 1.0 mol L^{-1} containing MeOH (1:1, in volume) under stirring. The beads of pure chitosan were kept under static conditions for 24 h at room temperature (32 °C) and then were washed with distilled water until pH = 7.0. Finally, the beads were freeze-dried (CSB) and stored in desiccator.

3.4.3 Preparation of cross-linked chitosan beads (CCSB)

Beads of cross-linked CS with GA were prepared according to the methodology of Monteiro, with adaptation[125]. Initially, CS solution 3.0% (m/v) was prepared by the dissolution of the compound in CH_3COOH 1.0% (v/v) using mechanical stirring for 24 h, at room temperature (32 °C). Then, the solution was dripped into the gelation solution of NaOH 1.0 mol L^{-1} and MeOH (1:1 in volume) under stirring. The spheres were kept under static conditions for 24 h at room temperature (32 °C), drained, and cross-linked with GA 3.0% (m/v)

in in water for 1.0 h at room temperature (32 °C) and then washed with distilled water until pH = 7.0. Finally, the obtained beads (CCSB), were freeze-dried and stored in desiccator.

Figure 12 – Flowchart describing the procedures performed to obtain the chitosan beads.

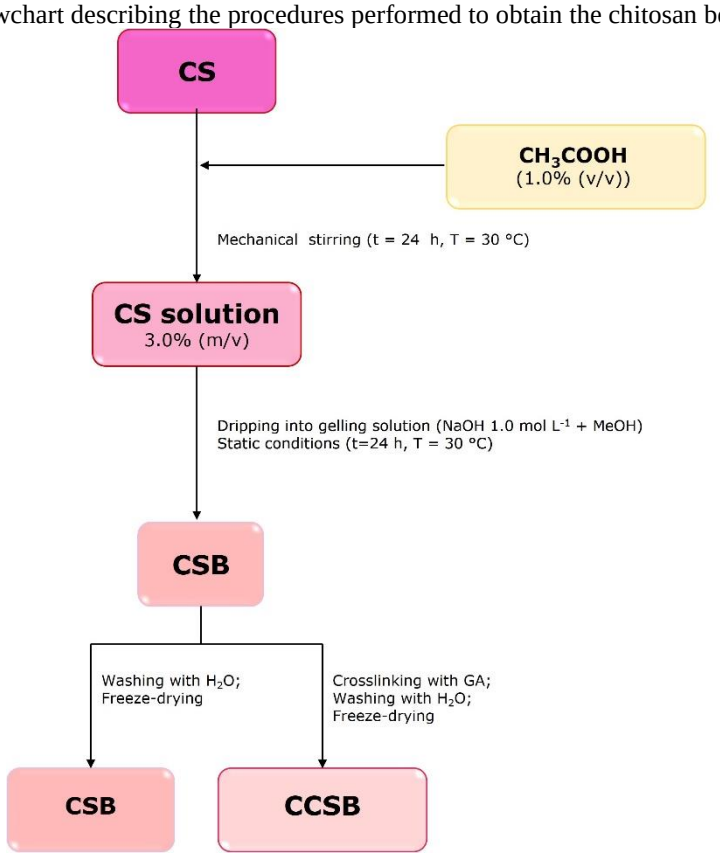

Source: The author (2022).

3.4.4 Preparation of chitosan-supported zeolite composites

The chitosan-supported composites were obtained via gelation of chitosan when it was dripped in an alkaline solution of NaOH, following the methodology of Monteiro[125]. Firstly, a solution of 3% (m/v) of chitosan in CH_3COOH 1% (m/v) was prepared, and, with a two-paddle mechanical stirrer, crystals of zeolite NaA were dispersed in it. The mixture was then dripped into an alkaline solution of NaOH 1.0 mol L^{-1} containing MeOH (1:1 in volume) under stirring. After the beads' formation, they were maintained under stable conditions for 24 h at room temperature (30 °C). Then, the beads were drained, cross-linked with glutaraldehyde, washed with distilled water until pH = 7.0, and freeze-dried.

The preparation of the magnetic composites followed a similar procedure, with the addition of the magnetic particles from the MF to the dispersion of zeolite in chitosan solution. The beads preparation occurred with the dripping of the mixture into a gelling solution, followed by crosslinking and freeze-drying.

Figure 13 illustrates the main procedures for the preparation of the magnetic and non-magnetic composites as a flowchart. The quantities used in the procedures are depicted in Table 4.

Figure 13 – Flowchart describing the main procedures of the composites manufacturing.

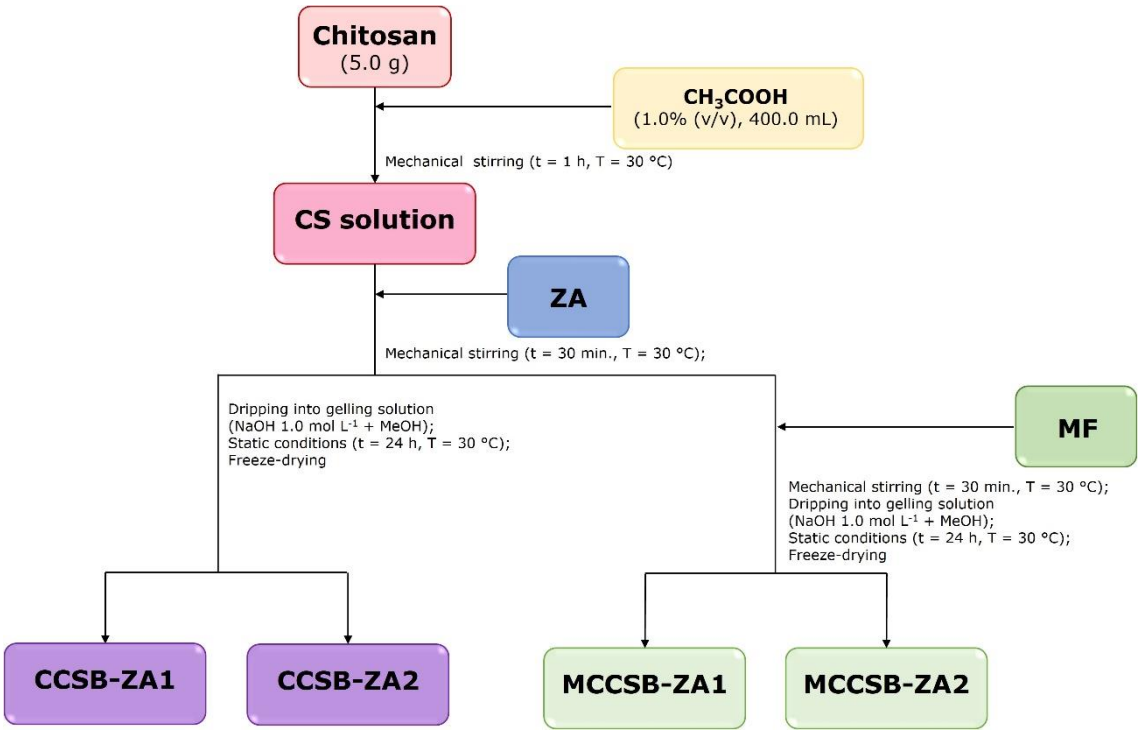

Source: The author (2022).

Table 4 – Quantities utilized for the preparation of the composites.

Composite	Volume of CS 3% (m/v) / mL	Mass of ZA / g	Mass of MF / g	Mass ratio CS:ZA:MF
CCSB-ZA1	100.0	0.750	-	4:1:0
CCSB-ZA2	100.0	1.500	-	2:1:0
MCCSB-ZA1	100.0	1.500	0.500	6:3:1
MCCSB-ZA2	100.0	1.500	1.000	6:3:2

Source: The author (2022).

3.5 Characterization

A comprehensive characterization of the obtained materials was conducted by employing different techniques, including X-ray fluorescence, X-ray diffractometry, Fourier-transform infrared spectroscopy, thermogravimetric analysis, magnetometry, and scanning electronic microscopy.

3.5.1 X-ray fluorescence (XRF)

XRF measurements were performed at the X-ray Laboratory (LRX) at the Department of Physics of the Federal University of Ceará (UFC), using a wavelength-dispersive X-ray (WDX) spectrometer Rigaku ZSX mini II, operating at 40 kV and 1.2 mA, with Pd tube.

3.5.2 X-ray powder diffractometry (XRD)

XRD measurements were performed in a Rigaku DMAXB diffractometer, with Bragg-Brentano geometry from LRX – UFC. The samples were prepared on a zero-background Si sample holder, and the X-ray diffractograms were obtained in the scan range of 2θ between 5 and 100°, with scan rate of $0.02°\ min^{-1}$, using Cu tube ($K\alpha_1 = 0.15406$ nm and $K\alpha_2 = 0.154439$ nm) at 40 kV and 30 mA. The crystalline phases identification was executed using the software X-PertHighScore (PANalytical) and the patterns were obtained using the Inorganic Crystal Structure Database (ICSD).

3.5.3 Fourier-transform infrared spectroscopy (FTIR)

FTIR analyses were performed in a Shimadzu IRTracer-100 equipment from Analytical Center of the Chemistry Graduate Program – UFC. The samples were dispersed in KBr pellets and analyzed in the scan range between 4000 and 400 cm^{-1}.

3.5.4 Scanning electron microscopy (SEM)

SEM analyses were performed using a Quanta 450 FEG-FEI microscope, with electronic beam acceleration voltage of 20.0 kV, and secondary electron and X-ray dispersive energy detectors. The non-magnetic samples were previously prepared on carbon tape, while the magnetic sample were prepared using silver glue, over aluminum stubs, coated with a 1 – 5 nm layer of gold in argon atmosphere and under vacuum, using a Quorum Q15DT ES equipment. The analyses were conducted at the Analytical Central of the UFC.

3.5.5 Thermogravimetric analysis (TGA)

Thermogravimetric analyses were performed by using a NETZSCH STA 449F3 equipment from the Foundry and Advanced Materials Laboratory from Metallurgic and Materials Engineering Department of the UFC. The analyses were performed putting the samples (5 mg) in an alumina pan and submitting them to heating from 30 to 600 ℃ under synthetic air atmosphere (50 mL min^{-1}) at a heating rate of 10 ℃ min^{-1}.

3.5.6 Vibrating Sample Magnetometry (VSM)

Static magnetization curves were recorded in a vibrating sample magnetometer of the Magnetic Nanostructures and Semiconductors Group (GNMS) of the Department of Theoretical and Experimental Physics (DFTE) of the Federal University of Rio Grande do Norte (UFRN). The magnetization curves (MxH) were obtained at room temperature under a magnetic field between -30 and 30 kOe.

3.6 Water softening tests

The performance of the obtained materials for water softening was assessed by putting them in contact with aliquots of hard water (Ca^{2+} 100 ppm) under different conditions of zeolite mass, to determine the optimum mass of adsorbent. The water softening tests were performed varying the adsorbate mass, from 10 to 100 mg of fly ash-based zeolite NaA.

4 RESULTS AND DISCUSSION

Here, we present the wide characterization of the prepared materials, confirming the efficiency of the employed methods and the performance of the zeolite-containing composites in the softening process of hard water.

4.1 X-ray fluorescence (XRF)

The XRF analyses were performed aiming to determine the chemical composition of non-magnetic and magnetic fractions extracted from coal fly ash. The oxide composition of NMF and MF samples are listed in Table 5.

Table 5 – X-ray fluorescence analyses results for the non-magnetic fraction (NMF) and the magnetic fraction (MF) obtained from the fly ashes (FA) treatment.

Oxide	Concentration (% m/m)	
	NMF	MF
MgO	-	1.76
Al_2O_3	19.09	14.16
SiO_2	57.27	47.02
SO_3		0.14
K_2O	3.43	2.26
CaO	6.40	4.71
TiO_2	1.68	2.25
MnO	-	0.46
V_2O_5	0.21	-
Fe_2O_3	11.53	26.82
ZnO	0.06	0.06
SeO_2	-	0.05
SrO	0.33	0.30

Source: The author (2022).

The results for the elemental analyses of fly ashes fractions, NMF and MF, revealed that silicon (Si), aluminum (Al), and iron (Fe) oxides are the major constituents of FA. It is also possible to observe in Table 5 that the concentration of iron oxide (Fe_2O_3) in the NMF sample is significantly minor than in the MF, indicating the efficiency of magnetic separation in the removal of Fe. The high concentration of Si and Al indicates the potential to use FA as starting materials in the syntheses of zeolitic materials,[126] and, considering the lower concentration of iron oxide, NMF is the most appropriate fraction for this purpose, once iron can interfere in the synthesis process.[127; 128]

4.2 X-ray powder diffractometry (XRD)

The XRD analyses were executed in order to obtain information about the crystallinity of the obtained materials, as well as the crystalline phases that constitute them.

4.2.1 Starting materials

The XRD patterns for the samples of purified chitosan, non-magnetic and magnetic fractions extracted from FA are showed in the diffractograms of Figure 14.

Figure 14 – XRD patterns for the starting materials samples: (a) chitosan – CS powder, (b) non-magnetic fraction of FA – NMF and (c) magnetic fraction of FA – MF. The image indicates the semicrystalline structure of CS and the presence of well-formed crystalline phases in NMF and MF samples.

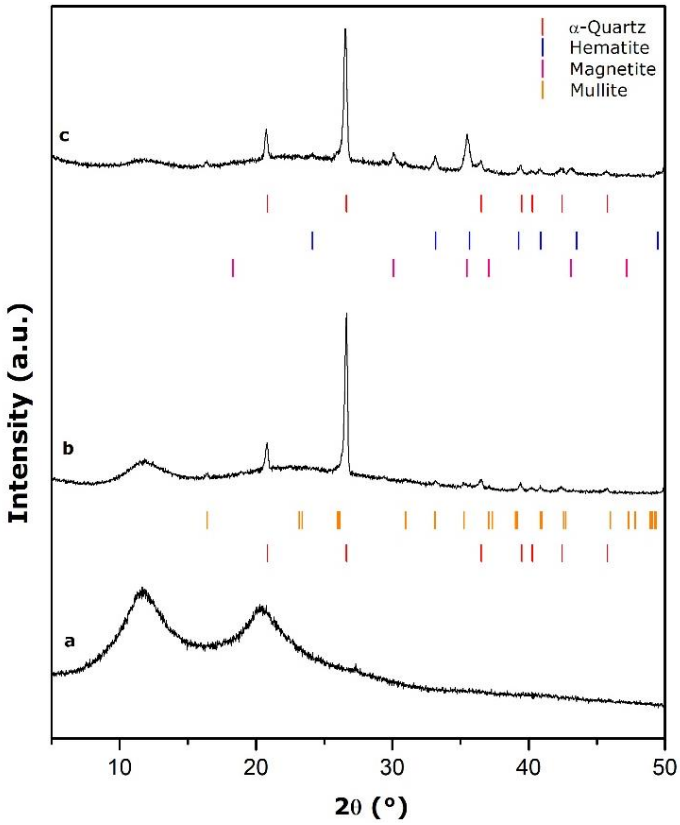

Source: The author (2022).

The X-ray powder diffractogram for the CS sample (Figure 14a) presents two broad peaks at 11.1 and 20.5°, indicating the semicrystalline nature of the sample. Taking into consideration the chitosan structure, represented in Figure 5, an amorphous behavior was already expected as result of its low order, and the semi-crystallinity is caused by the organization of fibrillar structures due to intra and intermolecular hydrogen bonds [129-134].

The XRD pattern for the sample of NMF (Figure 14b) shows the presence of intense, narrow peaks from two crystalline phases identified as α-quartz – SiO_2 (ICSD 34636)

and mullite – $Al_6Si_2O_{13}$ (ICSD 66448). The two peaks with higher relative intensity at 20.8 and 26.61° correspond to the α-quartz phase, and indicate a higher concentration of this phase in comparison with the mullite phase.[135] The identified phases are in accord with the XRF results in Table 5, once the latter indicated silica and alumina as the major composition of NMF and indicate the potential of this fraction of FA as starting material in the synthesis of zeolites.

The XRD pattern for the MF sample (Figure 14c) presents three crystalline phases: hematite (ICSD 66756), magnetite (ICSD 82435) and α-quartz (ICSD 89278). The sample presents narrow peaks, and it is mainly composed by iron oxides, with the most intense peak at 33.22° compatible with the hematite phase. It is also possible to observe the characteristic peaks of magnetite and α-quartz phases, at 35.58 and 26.58°, respectively.

4.2.2 Chitosan materials

Figure 15 presents the XRD patterns for the samples of chitosan-based materials.

Figure 15 – XRD results of the chitosan-based beads samples. (a) purified chitosan – CS powder, (b) pure chitosan beads – CSB, and (c) cross-linked chitosan beads – CCSB.

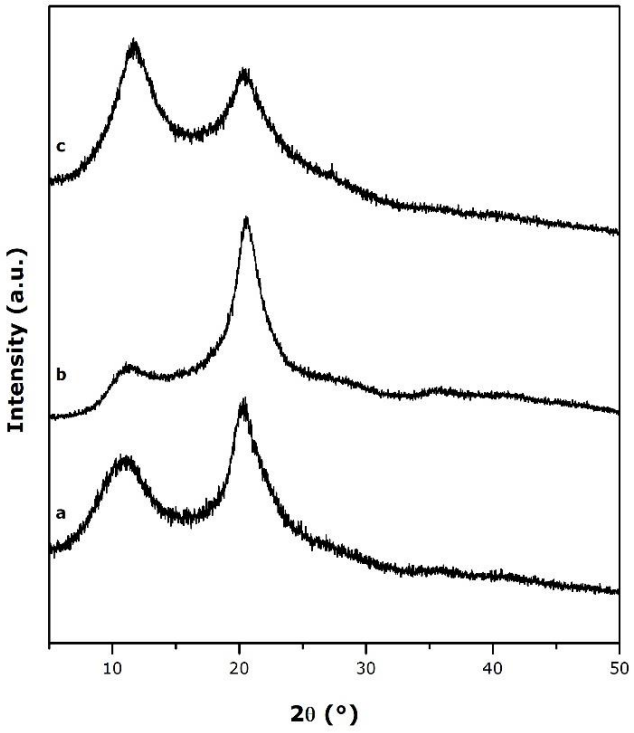

Source: The author (2022).

Figure 15b is the XRD pattern referent to the sample CSB, which is the freeze-dried bead of pure chitosan, and it presents two broad peaks with low intensity at 11.3 and 20.5°, matching the XRD pattern of CS powder (Figure 15a) as it was expected given that the composition was not altered. In Figure 15c, it is presented the XRD pattern for the CCSB

sample, as expected the amorphous behavior was maintained after the crosslinking of CS with GA due to low order of the structure (Figure 6). As a result of inter and intramolecular interactions, the semicrystalline nature of chitosan was preserved, originating two broad peaks at 11.7 and 20.5° in the XRD pattern.

4.2.3 Zeolite NaA

Figure 16 portrays the X-ray powder diffractograms for the samples of NMF (Figure 16a), and synthesized zeolite NaA from coal fly ashes (Figure 16b).

Figure 16 – X-ray powder diffractograms for the (a) non-magnetic fraction of FA – NMF and (b) fly ash-based zeolite NaA – ZA. The presence of characteristic peaks of zeolite LTA structure indicates the successful synthesis of this material using the NMF as source of SiO_2.

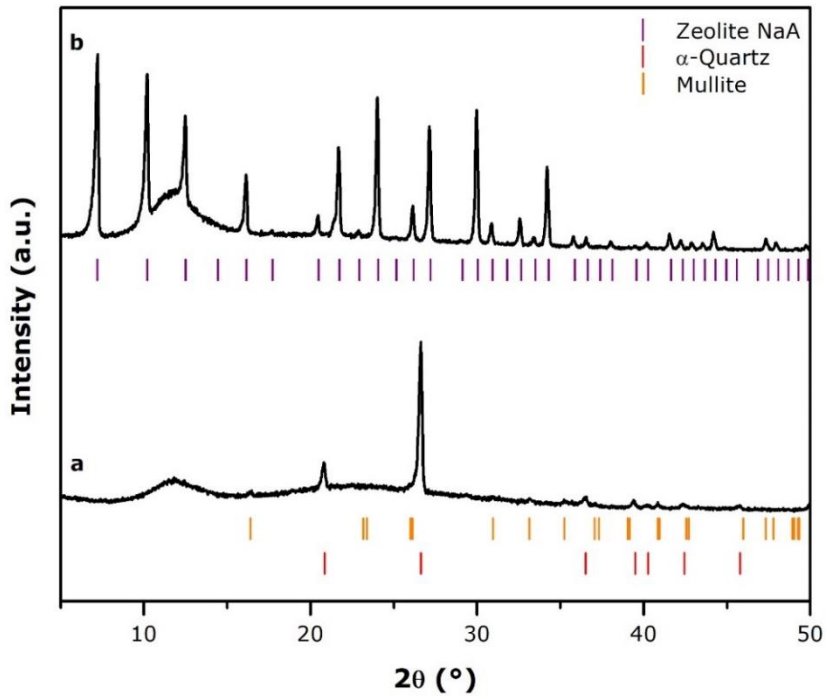

Source: The author (2022).

The XRD pattern for the sample of fly ash-based zeolite NaA shows narrow and intense peaks attributed to only one crystalline phase corresponding to zeolite LTA structure (ICSD 26911), with characteristic peaks at 7.22, 10.20, 12.48, and 16.14°, which corresponds to the expected product of the hydrothermal synthetic route, indicating the successful synthesis of the zeolite NaA.

4.2.4 Composites

The X-ray powder diffractograms for the non-magnetic composites are presented in Figure 17.

Figure 17 – XRD results for the samples: (a) cross-linked chitosan beads – CCSB, (b) cross-linked chitosan-supported zeolite NaA beads with CS:ZA mass ratio of 4:1 – CCSB-ZA1, (c) cross-linked chitosan-supported zeolite NaA beads with CS:ZA mass ratio of 2:1 – CCSB-ZA2, and (d) fly ash-based zeolite NaA – ZA.

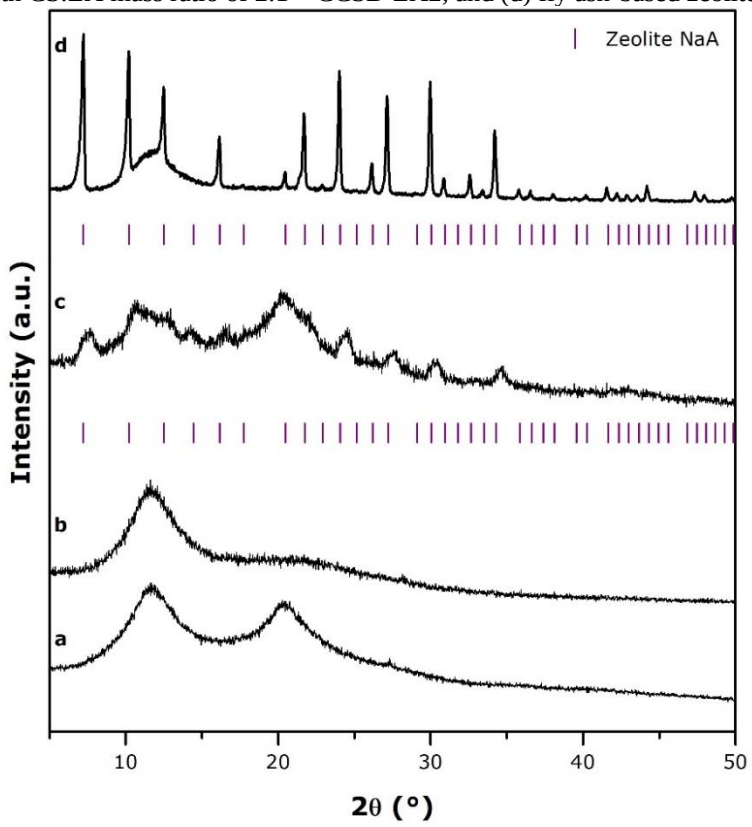

Source: The author (2022).

Figure 17 exhibits the XRD patterns for the non-magnetic composites and their components. The XRD pattern of CCSB-ZA1 sample (Figure 17b) presents a single, broad peak at 11.64°, consistent with the peak observed in the diffractogram of its matrix (Figure 17a). The non-existence of zeolitic peaks for this sample is a consequence of the low concentration of crystals of zeolite dispersed in the composite.

Although the CCSB-ZA2 XRD pattern (Figure 17c) shows the amorphous behavior from its chitosan matrix, it also displays peaks at 7.5, 10.6, 12.6, 14.3, 16.4, 20.3, 20.5, 21.9, 24.5, 27.6, 30.4, and 34.6°, which are consistent with the zeolite NaA structure (ICSD 10288), confirming the effective preparation of the composites. Notwithstanding, the peaks observed in Figure 17c are broader and exhibits lower intensity when compared with the pure zeolite NaA XRD pattern in Figure 17d, the decrease in the crystallinity and peak intensity of the zeolite NaA is a consequence of the introduction of chitosan polymeric chain.[136]

The XRD results for the magnetic composites are showed in Figure 18.

Figure 18: XRD results for the samples: (a) cross-linked chitosan beads – CCSB, (b) fly ash-based zeolite NaA – ZA, (c) magnetic cross-linked chitosan-supported zeolite NaA beads with CS:ZA:MF mass ratio of 6:3:1 – MCCSB-ZA1, (d) magnetic cross-linked chitosan-supported zeolite NaA beads with CS:ZA:MF mass ratio of 6:3:2 – MCCSB-ZA2, and (e) magnetic fraction of fly ash – MF.

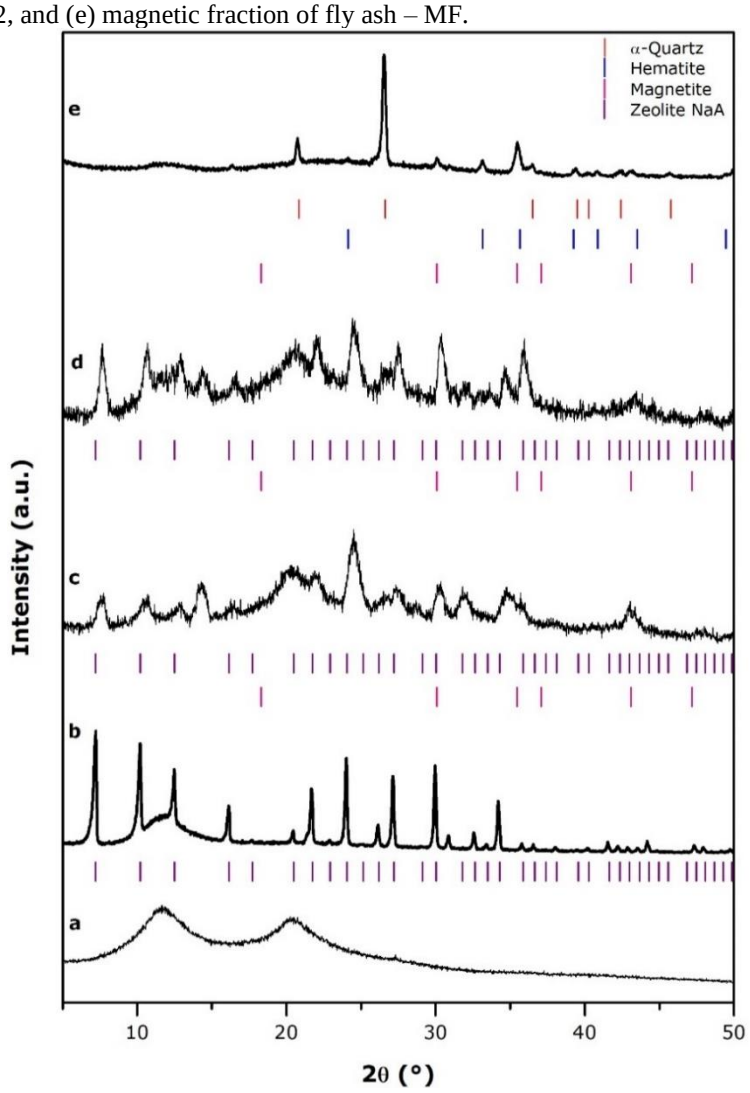

Source: The author (2022).

Similarly to the non-magnetic composite CCSB-ZA2 diffractogram (Figure 17c), the XRD patterns of the magnetic composites (Figure 18c-d), present lower intensity and crystallinity when compared to the diffractograms of ZA (Figure 18b) and MF (Figure 18e) samples, being a consequence of the introduction of chitosan matrix during the preparation of the composites.[136] The characteristic peaks of zeolite NaA are easily observed at 7.7, 10.6, 12.9, 14.3° in both composites. While the peaks at 30.4, 35.9, 43.9° are consistent with the magnetite phase from MF added in the composites.[137] The effective preparation of the magnetic composites was performed, and, as expected, the XRD pattern of MCCSB-ZA2 presents the peaks of magnetite with higher relative intensity, when compared to the sample of MCCSB-ZA1, due to the higher concentration of MF in the composite.

4.3 Fourier-transform infrared spectroscopy (FTIR)

4.3.1 Starting materials

The obtained FTIR spectra for the samples of purified chitosan powder, non-magnetic and magnetic fractions of fly ashes are displayed in Figure 19.

Figure 19 – FTIR spectra for the starting materials samples: (a) purified chitosan – CS powder; (b) non-magnetic fraction – NMF, and (c) magnetic fraction – MF.

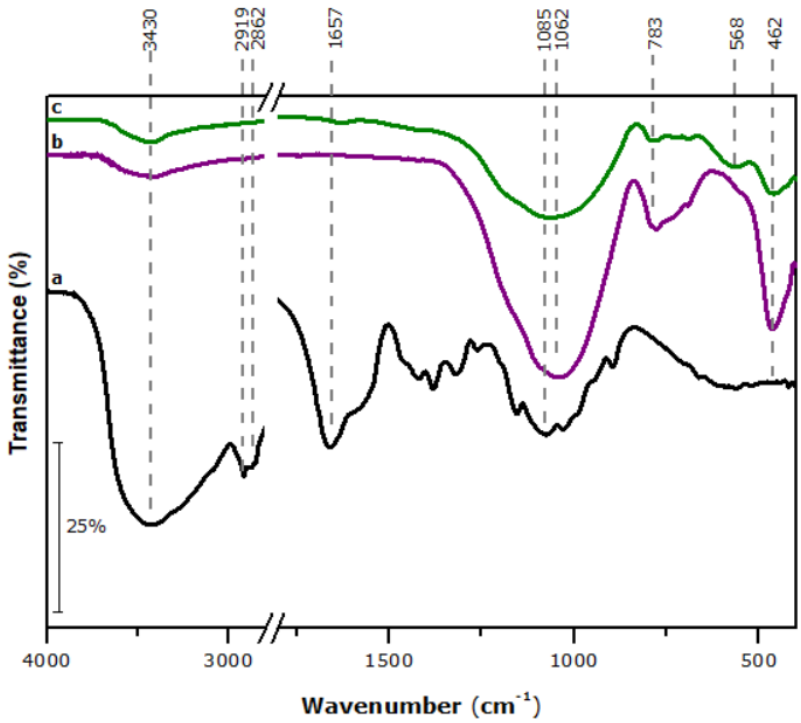

Source: The author (2022).

The CS powder infrared spectrum, Figure 19a, presents characteristic bands of chitosan structure (Figure 5). The major band located in the region between 3700 and 3000 cm^{-1}, with maximum at 3430 cm^{-1}, corresponds to the overlapped stretching vibrations of amino and hydroxyl groups.[138-140] The bands at 2919 and 2862 cm^{-1} are attributed to the asymmetric stretching of CH_3 and CH_2 groups in chitosan chain.[141-143] The band at 1657 cm^{-1} corresponds to stretching vibrations of amide groups present in chitosan structure.[143; 144] while the band at 1573 cm^{-1} is result of stretching vibration of N–H bond.[142; 143] The bands at 1382 and 1260 cm^{-1} are related to C–N axial deformations of amide and amine functions.[143-145] And the bands between 1154 and 897 cm^{-1} are characteristic of polysaccharide structure.[141; 143] The observed bands match the expected bands for the chitosan structure identified in the CS powder XRD pattern in Figure 14a.

Figure 19b presents the NMF FTIR spectrum with three well defined bands, being in consonance with the identified crystalline phases, α-quartz and mullite, in the XRD pattern in Figure 14b. The bands at 1062 and 778 cm^{-1} corresponds respectively to the asymmetric and symmetric stretching of T–O bonds (T = Si or Al), while the band at 461 cm^{-1} corresponds to deformation of O–T–O bonds.[146]

The MF spectrum presents bands at 1062 and 783 cm^{-1} related to the asymmetric and symmetric stretching of T–O bond.[147-150] The band at 568 cm^{-1} is attributed to vibrations of Fe–O from magnetite.[82; 143] And the band at 462 cm^{-1} corresponds to the deformation of O–T–O.[82] This result is consistent with the XRD pattern in Figure 14c that identifies α-quartz, magnetite and hematite as the components of MF.

The wavenumber attributions of the infrared absorption bands for the starting materials are available in the Table 6.

Table 6 – Attribution of infrared absorption bands to their respective wavenumber for the starting materials samples.

Identification of absorption bands	Wavenumber (cm^{-1})			
	CS	**NMF**	**MF**	**References**
ν (NH_2) in primary amines and ν (OH) in pyranose ring	3426		-	[105; 130; 138-143]
δ (C–H)	2919		-	[105; 130; 138-143]
ν (C–H) in pyranose ring	2862		-	[138-143]
β–1→4 glycosidic linkage	897, 1071		-	[130; 139; 141; 143]
ν (C–O) in $NHCOCH_3$ group	1657		-	[130; 138-144]
δ (N–H)	1573		-	[130; 138-143]
δ_s (CH_2) in CH_2OH group	1417		-	[105; 130; 138-143]
δ_{as} (C–N)	1382		-	[130; 138-140]
δ_{as} (CH_3)	1319		-	[138; 140-143]
ν (C–N) amide band	1260		-	[138; 140-145]
ν_{as} (C–O–C) (glycosidic linkage)	1154		-	[130; 138; 140-145]
ν(C–O) in CH_2OH group	1072		-	[105; 130; 138-141; 143]
ν_{as} T–O (T = Si or Al)	-	1062	1062	[82; 87; 91; 92; 107; 147-150]
ν_s T–O (T = Si or Al)	-	778	783	[82; 87; 91; 92; 148-151]
ν_{as} (Fe–O)	-	-	568	[82; 143; 152]
δ (O–T–O)	-	458	462	[82]

Source: The author (2022).

4.3.2 Chitosan materials

The obtained FTIR spectra for the chitosan-based materials are exhibited in Figure 20.

Figure 20 – FTIR spectra for the chitosan-based materials. (a) purified chitosan – CS powder, (b) freeze-dried chitosan beads – CSB, and (c) Glutaraldehyde cross-linked chitosan beads – CCSB.

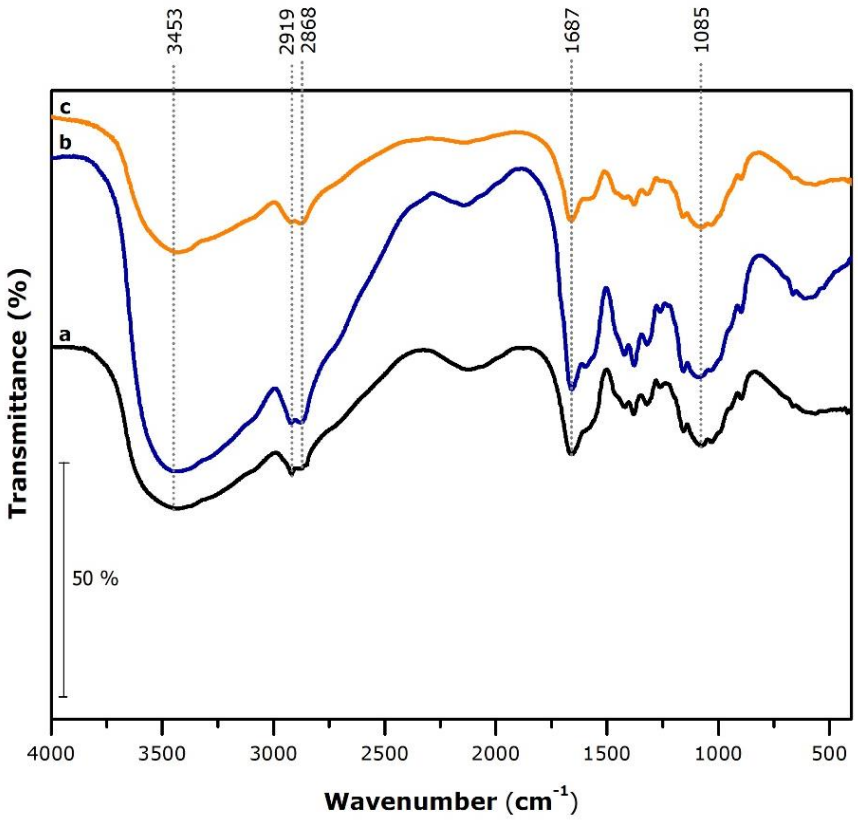

Source: The author (2022).

The spectrum of BCS sample (Figure 20 – FTIR spectra for the chitosan-based materials. (a) purified chitosan – CS powder, (b) freeze-dried chitosan beads – CSB, and (c) Glutaraldehyde cross-linked chitosan beads – CCSB.Figure 20b) has the same behavior as the spectrum for the CCSB sample (Figure 20c), and exhibits the same bands seen for the sample of purified chitosan (Figure 20a). Thus, it is possible to observe the maintenance of chitosan bands after the cross-linking with glutaraldehyde. The preservation of CS crystalline and spectroscopic characteristics indicates the integrity of the polymer chain, and therefore the potential of its use as the matrix in zeolitic composites.

4.3.3 Fly ash-based zeolite

Figure 21 presents the obtained FTIR spectrum for the zeolite NaA synthesized using the NMF as the main source of silicon and aluminum.

Figure 21 – FTIR spectra for the samples of (a) fly ash-based zeolite NaA – ZA, (b) non-magnetic fraction – NMF.

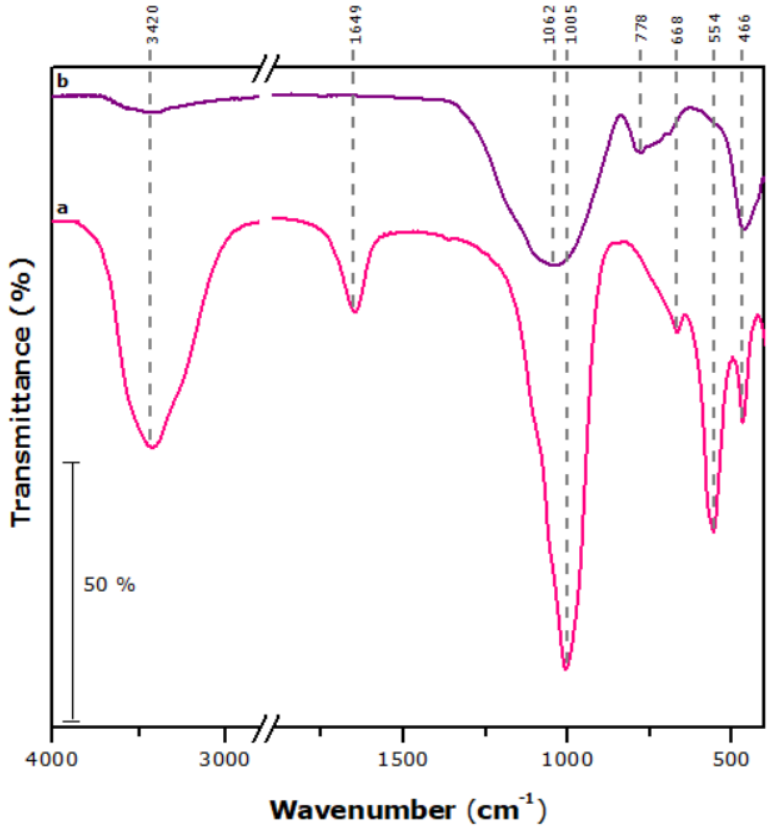

Source: The author (2022).

In the ZA spectrum presented in Figure 21a, it is possible to observe the presence of characteristic bands of the zeolitic structure, being in accord with the crystalline phase identified in Figure 16b. The bands at 3420 and 1649 cm^{-1} correspond to the stretching and deformation of O–H bond from the water molecules, and therefore indicate its presence [147-149]. The bands at 1005 and 668 cm^{-1} correspond to asymmetric and symmetric stretching of T–O bond (T = Si, Al) [147-149]. The stretching and deformation vibrations of the double 4-ring (D4R) structure are represented by bands at 554 and 466 cm^{-1}.[153; 154]

The wavenumber attributions of the infrared absorption bands for the samples of NMF and ZA are available in the Table 7.

Table 7 – Wavenumber attribution to their respective infrared absorption bands for the samples of NMF and ZA.

Identification of absorption bands	Wavenumber (cm^{-1})		
	NMF	ZA	References
ν (O–H) in H_2O	-	3420	[92; 147; 149]
δ (O–H) in H_2O	-	1649	[87; 92; 148; 149; 153]
ν_{as} T–O (T = Si or Al)	1062	1005	[82; 87; 91; 92; 107; 147-149]
ν_s T–O (T = Si or Al)	778	668	[82; 87; 91; 92; 148-151]
ν D4R (external vibration)	-	554	[87; 91; 147-149; 154]
δ (TO_4) D4R (internal vibration)	-	466	[87; 91; 92; 147; 148; 153]
δ (O–T–O)	458	-	[82]

Source: The author (2022).

4.3.4 Composites

FTIR spectra for the non-magnetic composites are presented in Figure 22.

Figure 22 – FTIR spectra for the samples of (a) cross-linked chitosan beads – CCSB, (b) cross-linked chitosan-supported zeolite NaA beads with CS:ZA mass ratio of 4:1 – CCSB-ZA1, (c) cross-linked chitosan-supported zeolite NaA beads with CS:ZA mass ratio of 2:1 – CCSB-ZA2, and (d) fly ash-base zeolite NaA – ZA. .

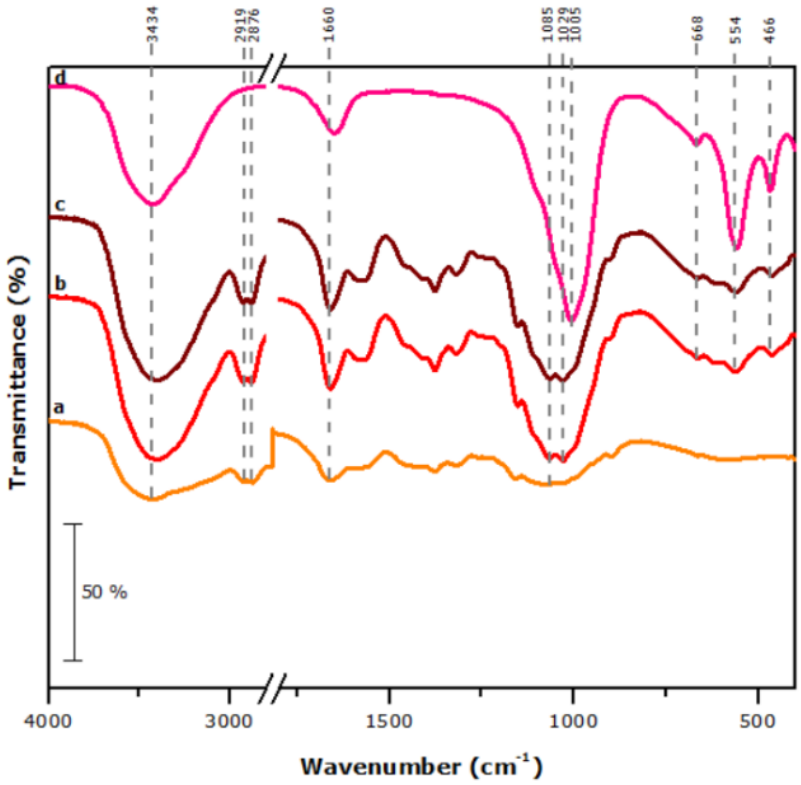

Source: The author (2022).

Figure 22b-c present the composites' FTIR spectra, and both present the same shape, corresponding to the resultant interaction of their components: chitosan and zeolite.

The FTIR spectra of CCSB-ZA1 (Figure 22b) and CCSB-ZA2 (Figure 22c) samples present a broad band at 1029 cm^{-1} attributed to the overlapping of asymmetric vibration of TO_4

tetrahedra from ZA,[87; 91; 92; 105; 107; 147-150] and C–O stretching, from CS.[105; 130; 138-141; 143] It is also possible to observe discrete bands at 668, 554, and 466cm^{-1}, corresponding to vibrations related to D4R structure of the zeolite NaA.[82; 87; 91; 92; 147-151; 154]

The broad band with maximum at 3438 cm^{-1} is attributed to stretching vibrations of amino and hydroxyl groups from CS,[105; 130; 138-143] and the hydroxyl groups from hydration water in ZA crystals.[92; 147; 149] The band at 1660 cm^{-1}, with higher relative intensity than the one observed in the CS spectra, was attributed to water of hydration in the zeolitic sample.[92; 147; 149]

The information extracted from the bands present in the FTIR spectra combined to the XRD patterns in Figure 17 indicate the successful preparation of zeolite NaA supported by chitosan composites.

The wavenumber attributions of the infrared absorption bands for the non-magnetic composites' samples are available in Table 8.

Table 8 – Attribution of infrared absorption bands to their respective wavenumber for the samples of CCSB, CCSB-ZA1, CCSB-ZA2, and ZA.

Identification of absorption bands	Wavenumber (cm^{-1})				
	CCSB	**CCSB-ZA1**	**CCSB-ZA2**	**ZA**	**References**
ν (NH_2) in primary amines and ν (OH) in pyranose ring	3428	3438	3438	-	[105; 130; 138-143]
δ (C–H)	2918	2919	2919	-	[105; 130; 138-143]
ν (C–H) in pyranose ring	2876	2881	2889	-	[138-143]
β–1→4 glycosidic linkage	897, 1071	898, 1028	801, 1028	-	[130; 139; 141; 143]
ν (C–O) in $NHCOCH_3$ group	1661	1661	1661	-	[130; 138-144]
δ (N–H)	1573	1571	1571	-	[130; 138-143]
δ_s (CH_2) in CH_2OH group	1417	1418	1415	-	[105; 130; 138-143]
δ_{as} (C–N)	1375	1383	1383	-	[130; 138-140]
δ_{as} (CH_3)	1319	1317	1317	-	[138; 140-143]
ν (C–N) amide band	1255	1260	1260	-	[138; 140-145]
ν_{as} (C–O–C) (glycosidic linkage)	1160	1155	1152	-	[130; 138; 140-145]
ν(C–O) in CH_2OH group	1085	1066	1066	-	[105; 130; 138-141; 143]
ν_{as} T–O (T = Si or Al)	-	1028	1028	1005	[82; 87; 91; 92; 107; 147-150]
ν_s T–O (T = Si or Al)	-	666	663	668	[82; 87; 91; 92; 148-151]
δ (O–H) in H_2O	-	1661	1661	1649	[87; 92; 148; 149; 153]
ν (O–H) in H_2O	-	3438	3438	3420	[92; 147; 149]
ν D4R (external vibration)	-	560	560	554	[87; 91; 147-149; 154]
δ (TO_4) D4R (internal vibration)	-	459	460	466	[87; 91; 92; 147; 148; 153]

Source: The author (2022).

The FTIR spectra for the magnetic composites and their components are available in Figure 23.

Figure 23 – FTIR spectra for the samples: (a) cross-linked chitosan beads – CCSB, (b) magnetic cross-linked chitosan-supported zeolite NaA beads with CS:ZA:MF mass ratio of 6:3:1 – MCCSB-ZA1, (c) magnetic cross-linked chitosan-supported zeolite NaA beads with CS:ZA:MF mass ratio of 6:3:2 – MCCSB-ZA2, (d) fly ash-based zeolite NaA – ZA, and (e) magnetic fraction of fly ash – MF.

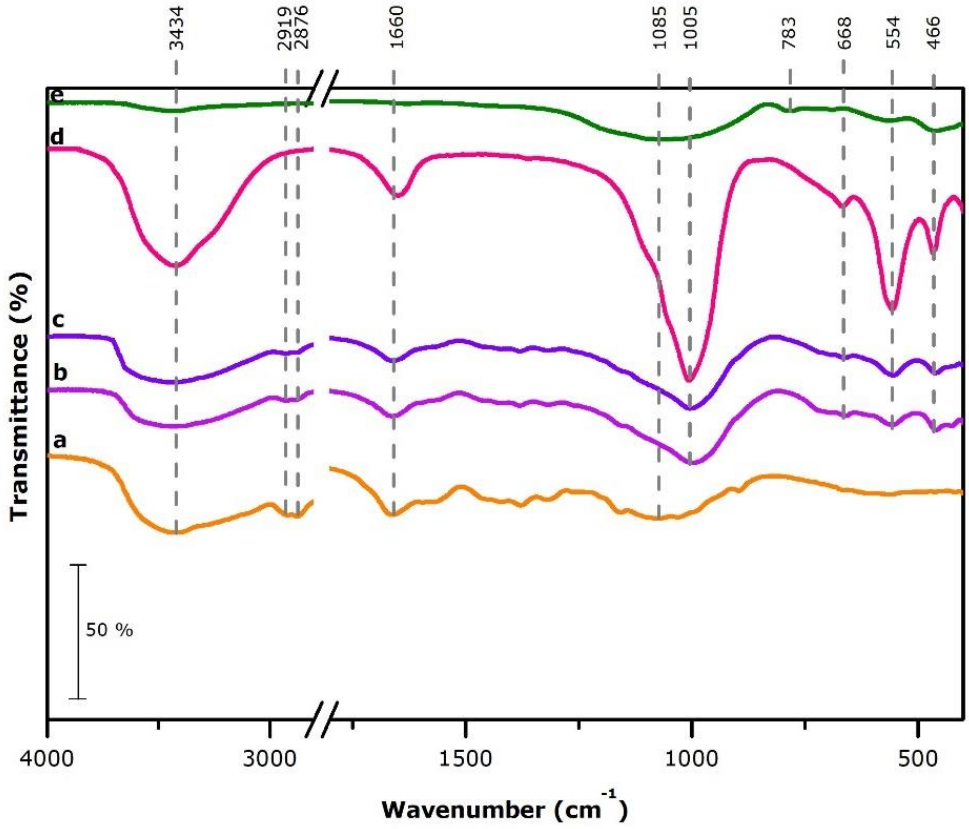

Source: The author (2022).

The FTIR spectra for the magnetic chitosan-supported zeolite NaA composites, Figure 23b-c, show significant differences from the spectra of their starting materials. The band at 3434 cm^{-1} corresponds to both hydroxyl groups stretching vibrations of hydration water found in the zeolitic structure,[92; 147; 149] and stretching vibrations of amino and hydroxyl groups present in CS,[105; 130; 138-141; 143] The bands at 2919 and 2876 cm^{-1} are related to the asymmetric stretching of CH_3 and CH_2 groups in chitosan,[105; 130; 138-143] while the bands at 1660 and 1565 cm^{-1} are caused by stretching vibrations of amide groups,[130; 138-144] and N–H stretching vibration of CS, respectively.[130; 138-143] The bands at 1379 and 1250 cm^{-1} are attributed to C–N the axial deformations of amide and amine functions.[130; 138-145] Both of the composite spectra present a broad band in the region between 1200 and 900 cm^{-1}, with maximum at 1003 cm^{-1}, this interval comprises bands related to vibrations of polysaccharide structure[130; 139; 141; 143] from CS matrix, and symmetric and asymmetric stretching vibrations of T–O bond presented

in ZA crystalline structure and in quartz phase of MF,[87; 91; 92; 105; 107; 147-150] the deformation observed is a result of overlapped vibration from the composites components.

Both composites present bands at 558 cm^{-1}, which correspond to Fe–O asymmetrical stretching, confirming the presence of MF fraction in the samples, overlapped with external vibration from D4R from ZA crystals. The band at 466 cm^{-1} is related to the overlapped deformation vibration from O–T–O present in the quartz phase of MF, with internal vibration from TO_4 tetrahedra from D4R from ZA. Bands at 1006 and 712 cm^{-1} are related to symmetric stretching occurred at T–O. The FTIR spectra indicate the presence of all the components added during the preparation of the composites and indicate the successful preparation of these materials.

The wavenumber attributions of the infrared absorption bands for the samples of magnetic composites are available in Table 9.

Table 9 – Attribution of wavenumber to the infrared absorption bands observed for the samples of CCSB, MCCSB-ZA1, MCCSB-ZA2, ZA, and MF.

Identification of absorption bands	Wavenumber (cm^{-1})					
	CS	**MCCSB-ZA1**	**MCCSB-ZA2**	**ZA**	**MF**	**References**
ν (NH_2) in primary amines and ν (OH) in pyranose ring	3415	3434	3434	-	-	[105; 130; 138-143]
δ (C–H)	2918	2919	2919	-	-	[105; 130; 138-143]
ν (C–H) in pyranose ring	2877	2876	2876	-	-	[138-143]
β–1→4 glycosidic linkage	897, 1071	889, 1073	889, 1073	-	-	[130; 139; 141; 143]
ν (C–O) in $NHCOCH_3$ group	1659	1660	1660	-	-	[130; 138-144]
δ (N–H)	1573	1565	1565	-	-	[130; 138-143]
δ_s (CH_2) in CH_2OH group	1417	1434	1434	-	-	[105; 130; 138-143]
δ_{as} (C–N)	1382	1379	1379	-	-	[130; 138-140]
δ_{as} (CH_3)	1319	1250	1250	-	-	[138; 140-143]
ν (C–N) amide band	1260	1268	1268	-	-	[138; 140-145]
ν_{as} (C–O–C) (glycosidic linkage)	1154	1164	1164	-	-	[130; 138; 140-145]
ν(C–O) in CH_2OH group	1039	1003	1003	-	-	[105; 130; 138-141; 143]
ν_{as} T–O (T = Si or Al)	-	1006	1006	1005	1062	[82; 87; 91; 92; 107; 147-150]
ν_s T–O (T = Si or Al)	-	668	668	668	783	[82; 87; 91; 92; 148-151]
ν_{as} (Fe–O)	-	558	558	-	568	[82; 143; 152]
δ (O–T–O)	-	466	466	-	462	[82]
δ (O–H) in H_2O	-	1660	1660	1649	-	[87; 92; 148; 149; 153]
ν (O–H) in H_2O	-	3434	3434	3420	-	[92; 147; 149]
ν D4R (external vibration)		554	554	554	-	[87; 91; 147-149; 154]
δ (TO_4) D4R (internal vibration)		466	466	466	-	[87; 91; 92; 147; 148; 153]

Source: The author (2022).

4.4 Scanning electron microscopy (SEM)

4.4.1 Magnetic fraction

Scanning electron micrographs of the particles that constitutes the MF obtained from coal fly ashes are shown in Figure 24.

Figure 24 – Scanning electron micrographs of magnetic fraction (MF).

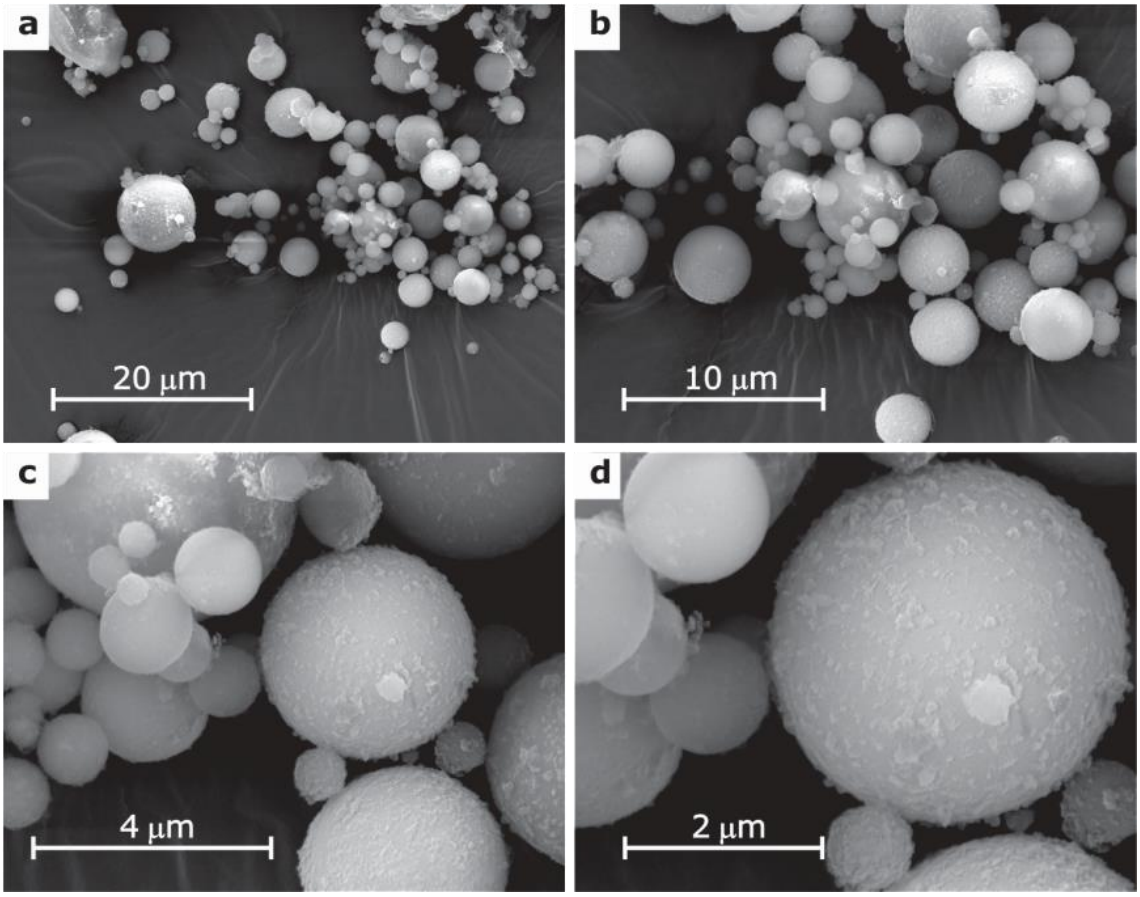

Source: The author (2022).

The SEM images of the magnetic fraction show spherical particles, characteristic of fly ash,[155] consisting of aluminosilicate and magnetite.[156] In Figure 24a-b, it is possible to observe the heterogeneous size distribution of MF particles.[157] In Figure 24c-d, it is possible to observe the rough features of the particles surfaces,[158] these irregularities are result of the presence of iron oxide crystals, hematite and magnetite,[159] consistent with the XRF results (Table 5), XRD pattern (Figure 14c) and FTIR result (Figure 19c).

The irregularities observed on the surface of the spheres have asymmetrical shape and correspond to the iron oxides, identified as hematite and magnetite with the XRD analyses. These particles are originated by the transformations suffered during the fusion and melting of

the coal components during its burn, as the iron components condense over the surface of the silicate cenospheres.[160; 161]

4.4.2 Non-magnetic fraction

Figure 25 exhibits the SEM images for the sample of NMF extracted from coal fly ash.

Figure 25 – SEM images of the NMF sample obtained from the coal fly ash treatment. (b) cenosphere, with approximately 30 μm of diameter, filled with smaller particles, exposing the hollow feature of these particles

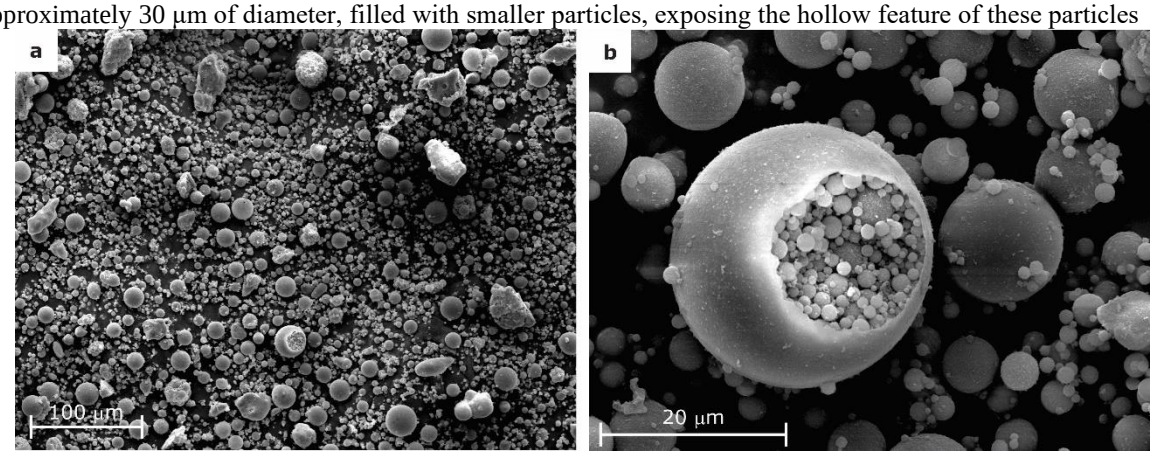

Source: The author (2022).

Similar to the MF, the NMF presents heterogeneous size distribution of particles, as it can be seen in Figure 25a.[161] Unlike the MF particles, the NMF spheres present uniform surfaces, as it can be perceived in Figure 25b, it is also noticed the hollow feature of these aluminosilicate particles, characteristic of the FA cenospheres[162] produced as a consequence of the expansion of the gases during the burning of the mineral coal.[163] The sample's morphology indicates the effective magnetic separation, with uniform composition, matching the results of XRF (Table 5), XRD (Figure 14b) and FTIR (Figure 19b) analyses.

4.4.3 Chitosan materials

The SEM images for the samples of pure chitosan, pure chitosan beads, and crosslinked chitosan beads in Figure 26, it is easily seen the diverse morphologies of each produced sample.

Figure 26 – Scanning electron micrographs for the chitosan-based materials: (a-b) purified chitosan powder – CS powder, (c-d) pure chitosan beads – CSB and (e-f) cross-linked chitosan beads – CCSB.

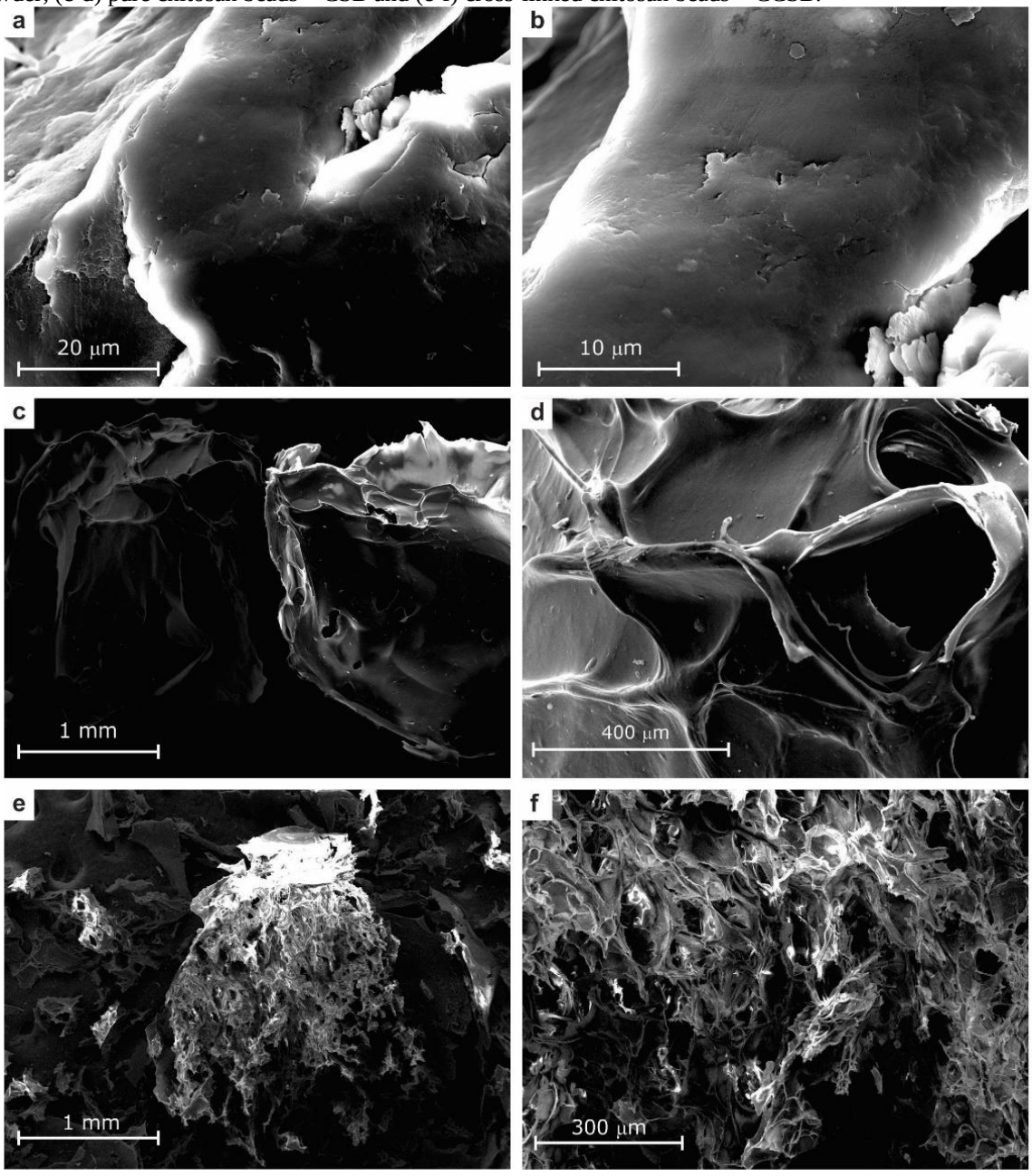

Source: The author (2022).

Figure 26 presents the diverse morphologies of the prepared chitosan-based materials. It is possible to recognize the homogeneous surface of CS powder grains (Figure 26a-b), the low porosity and rugosity of this material.[164; 165] In contrast with the morphology of CS powder, the CSB sample exhibits beads with diameter of approximately 1 mm (Figure 26c), homogeneous surface[165] and cavities (Figure 26d) that indicate the macroporous nature of this material.[166]

The SEM images of the CCSB sample present a bead with 1 mm diameter (Figure 26e), it also presents interconnected cavities (Figure 26e-f), characteristic of interest in the production of hierarchical porous composites.[165-167]

4.4.4 Fly ash-based zeolite NaA

The SEM images of the synthesized zeolite NaA employing the non-magnetic fraction of coal fly ash are available in Figure 27.

Figure 27 – SEM images of fly ash-based zeolite NaA.

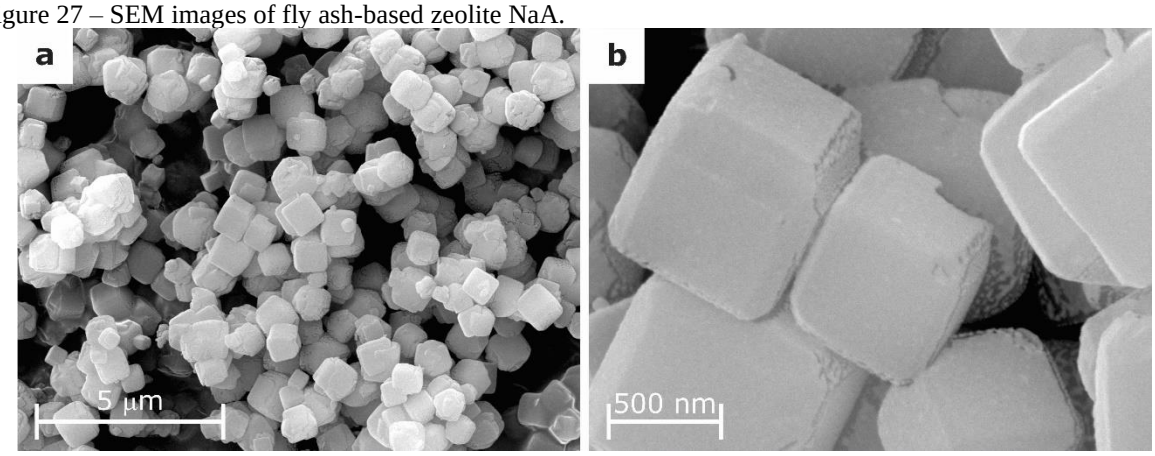

Source: The author (2022).

The SEM analysis of the synthesized sample of zeolite NaA using the NMF as source of silicon and aluminum revealed the expected morphology for the materal. Figure 27a shows the homogeneous size distribution of zeolite NaA crystals, in Figure 27b it can be observed that the material is composed of cubic crystals, very different from the spheroidal particles of NMF in Figure 25. The cubic crystalline habit with chamfered edges is characteristic of zeolite LTA as expected from the samples' XRD pattern (Figure 16b).[121; 163] The SEM images show results compatible with the other characterization results, indicating the successful synthesis of zeolite NaA using the NMF of FA as starting material.

4.4.5 Non-magnetic composites

Figure 28 presents the SEM images for the sample of CCSB-ZA2, porous hierarchical composite prepared via the dispersion of zeolite NaA crystals in chitosan matrix.

Figure 28 – SEM images of chitosan-supported zeolite NaA with mass ratio of 2:1 – CCSB-ZA2.

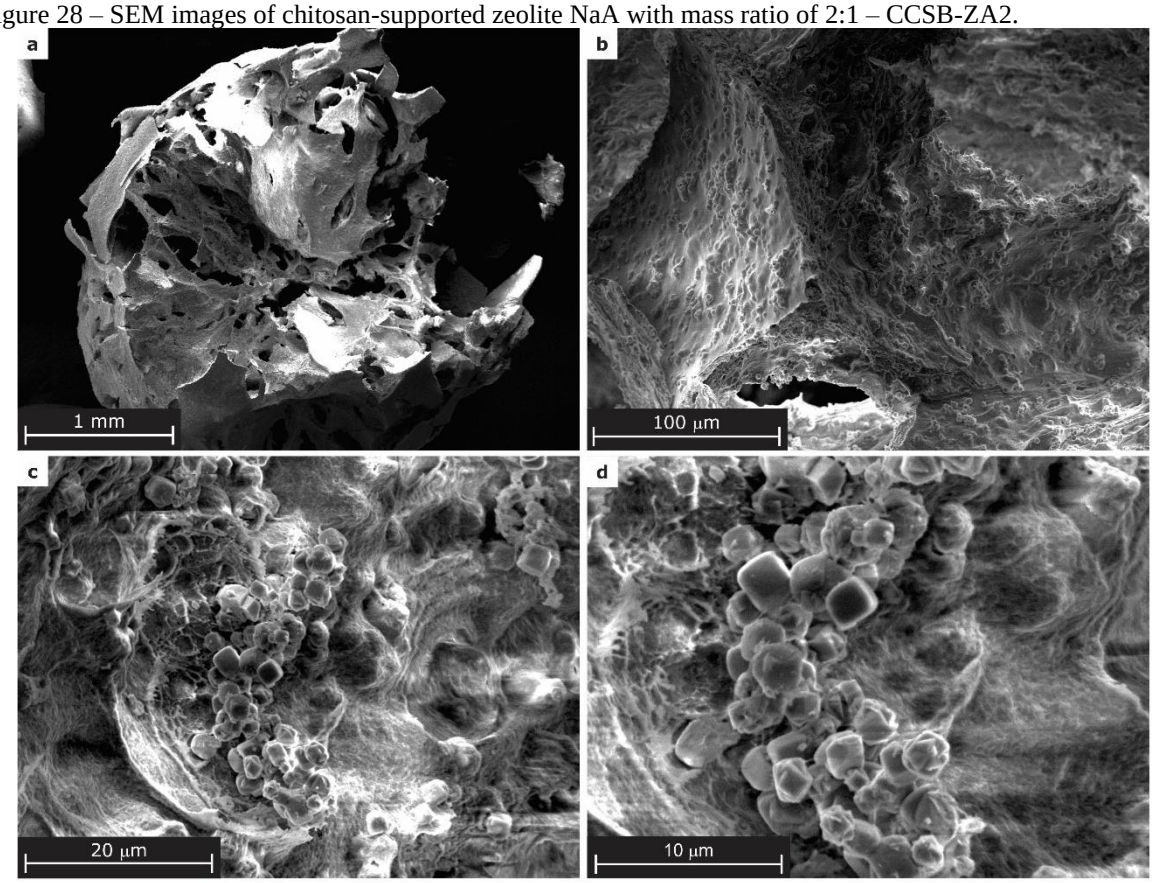

Source: The author (2022).

Figure 28a shows a CCSB-ZA1 bead with 1 mm diameter, similar to the CCSB bead in Figure 26e, it is easily observed the interconnected cavities of chitosan matrix.[166] In Figure 28b, it is possible to see the dispersion of cubic crystals in the polymeric matrix, indicating a good distribution of zeolite in the composite. Figure 28c shows the zeolite NaA crystals on the surface of chitosan, indicating the interconnectivity between the porous of the composite components, which is a desirable feature for the composite. It is also possible to observe that some zeolite crystals are covered by a layer of chitosan, indicating the crystals are supported by physical interactions between the polymer and zeolite.[168]

4.5 Thermogravimetric analyses (TGA)

The curves resulted from the thermogravimetric analyses for the samples of pure chitosan beads, fly ash-based zeolite NaA, and the magnetic fraction of fly ash are presented in Figure 29.

Figure 29 – TGA results for the samples of starting materials: (a) CSB, (b) MF, and (c) zeolite NaA.

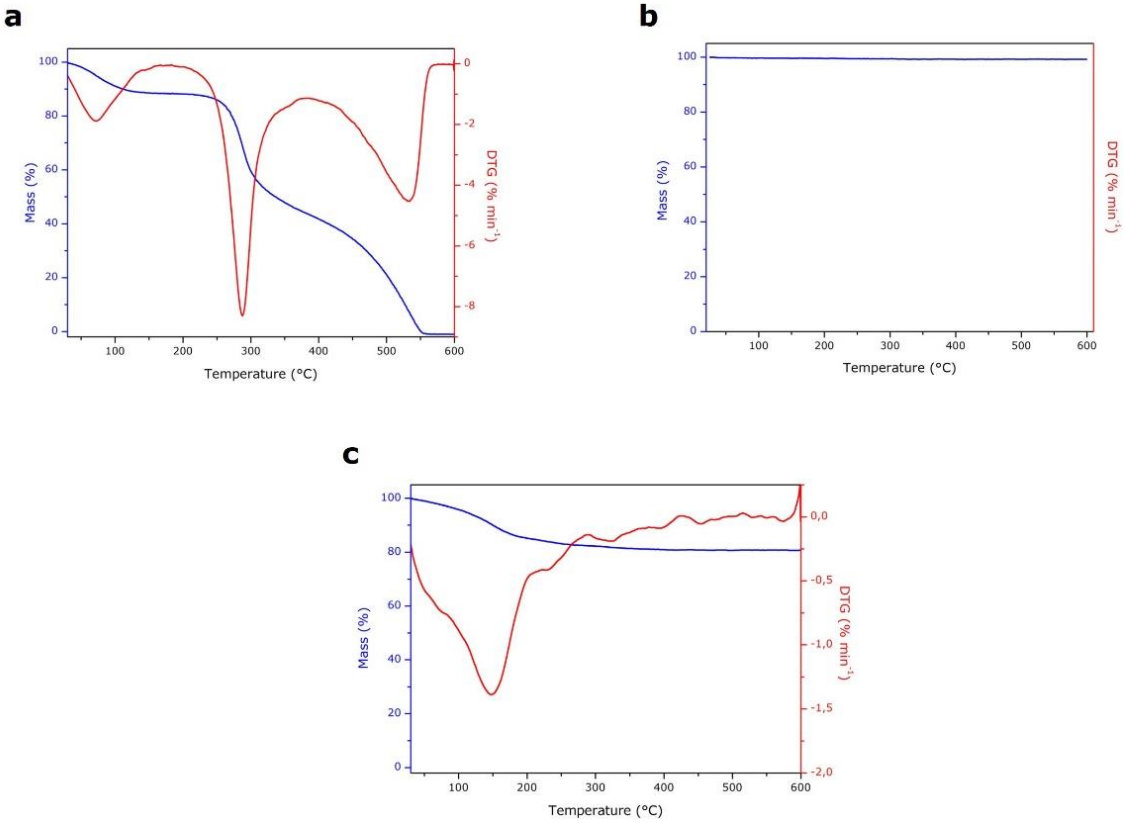

Source: The author (2022).

CSB shows a mass loss of 11.81% in the temperature range of 30.0 to 222.4 °C, with a maximum degradation temperature at 71.9 °C, corresponding to the evaporation of adsorbed water present in the sample.[169; 170] A second step in the TGA curve occurs between 222.4 °C and 414.8 °C, and it is related to the oxidative decomposition of the polymeric chain of chitosan, including the dehydration of the saccharide rings, depolymerization and decomposition of acetylated and deacetylated units of the polymer with vaporization of volatile compounds, CSB sample presented a mass loss of 44.59% with a maximum degradation temperature at 287.5 °C. Finally, a third degradation event can be observed between 414.8 and 600.0 °C, with maximum peak at 533.4 °C, corresponding to the residual cross-linked degradation of chitosan,[171-173] the mass loss associated to this phenomenon is 43.60%. The residual mass of CSB for this analysis was of 0.95% at 600.0 °C.

For the ZA sample, it is observed only one step in the TGA curve, from 30.0 to 304.1 °C, with a mass loss of 17.96%, corresponding to the evaporation of water molecules present in the sample.[174-176] At 600.0 °C, the zeolite sample showed a residual mass of 80.73%, indicating its thermal stability at the heating rate employed.

For the sample of MF, no thermodegradative events were observed.

4.5.1 Chitosan materials

Figure 30 shows the thermograms for the samples of pure chitosan beads and the glutaraldehyde cross-linked chitosan beads.

Figure 30 – TGA curves for the samples of pure chitosan beads (CSB), and chitosan beads cross-linked with glutaraldehyde (CCSB).

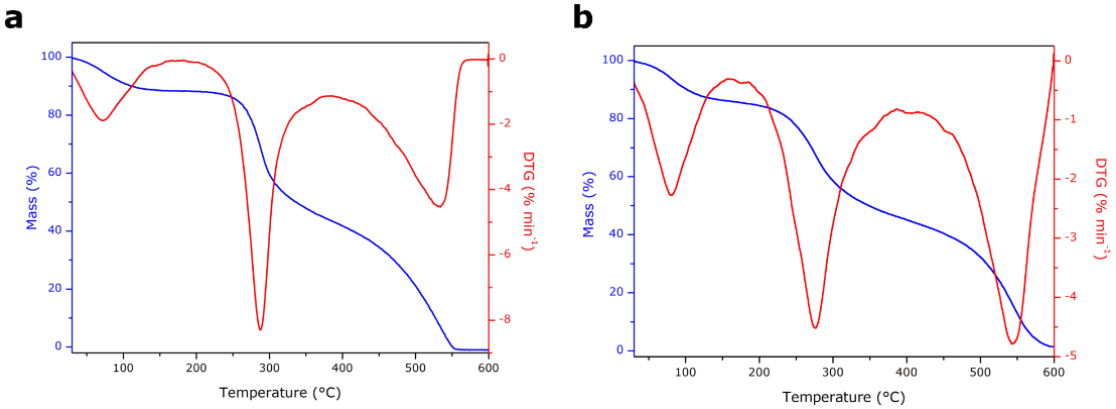

Source: The author (2022).

The curves resulted from the thermogravimetric analyses of the samples of CSB and the CCSB in Figure 30 present the same shape, and they indicate the occurrence of three degradation events for both materials.

CCSB presents 15.40% of mass loss at the temperature range of 30.0 – 195.6 °C, with a maximum degradation at 80.8 °C. Similarly, to the sample of CSB, this step corresponds to the evaporation of adsorbed water in sample. The second degradation event occurs in the temperature range between 195.6 °C to 433.5 °C and it is related to the oxidative decomposition of the polymeric chain of chitosan, including the dehydration of the saccharide rings, depolymerization and decomposition of acetylated and deacetylated units of the polymer with vaporization of volatile compounds, the sample presented a mass loss of 38.42% with a maximum peak of degradation at 276 °C.[177] The last step of the TGA curve can be observed from 433.5 to 600.0 °C, with a maximum peak at 545.4 °C, representing the residual cross-linked degradation of chitosan,[171-173] the mass loss associated to this phenomenon is 46.13%.

The CCSB sample presented a residual mass of 1.40 %, slightly higher than the residual mass of CSB at the same parameters. Therefore, the cross-linking had showed effect in the thermo stability of the chitosan polymeric chain.

4.5.2 Composites

Figure 31 illustrates the thermograms for the samples of glutaraldehyde cross-linked chitosan beads, zeolite NaA and the non-magnetic composites.

Figure 31 – TGA curves for the samples of the chitosan beads crosslinked with glutaraldehyde (CCSB), zeolite NaA (ZA), and the non-magnetic composites.

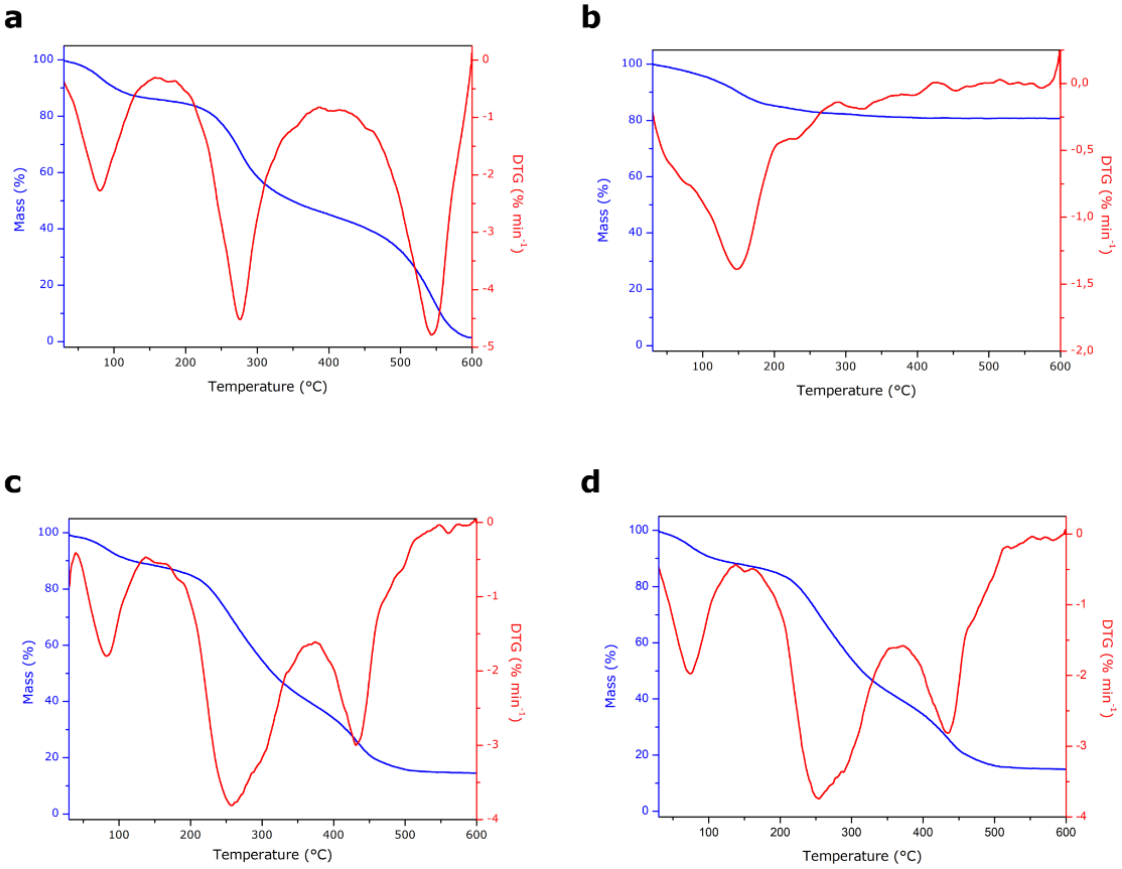

Source: The author (2022).

The thermodegradative curves for the non-magnetic composites are similar to the CCSB thermodegradative curve, three distinguished events of degradation. The first one, related to the desorption of water from chitosan and zeolite which constitute the composites,[178] is observed in the temperature range of 30.0 – 169.7 °C for the CCSB-ZA1 sample and 30.0 – 161.8 °C for the CCSB-ZA2 sample, with mass losses of 11.33% and 11.58%, respectively.

The second mass loss region in the temperature ranges of 169.7 – 380.9 °C and 161.8 – 372.6 °C for the CCSB-ZA1 and CCSB-ZA2, respectively, correspond to the degradation of the matrix polymeric chains. In general, the presence of zeolite 4A crystals dispersed in chitosan barely affected the thermal stability of CS.[179]

After the second stage of degradation, the composites went under a third step of degradation, corresponding to the further oxidation of the materials, in the temperature ranges of 380.9 to 600.0 °C for the sample of CCSB-ZA1 and 372.6 to 600.0 °C for the CCSB-ZA2.[180] When the char temperature reached 600 °C the residual masses of the composites was 14.98% for the CCSB-ZA1 and 14.59% for the CCSB-ZA2, indicating the complete burn of the polymer matrix and the zeolite being the residue.[181]

Figure 32 exhibits the thermograms for the samples of ZA, MF and the magnetic chitosan-supported composites.

Figure 32 – TGA curves for the magnetic composites.

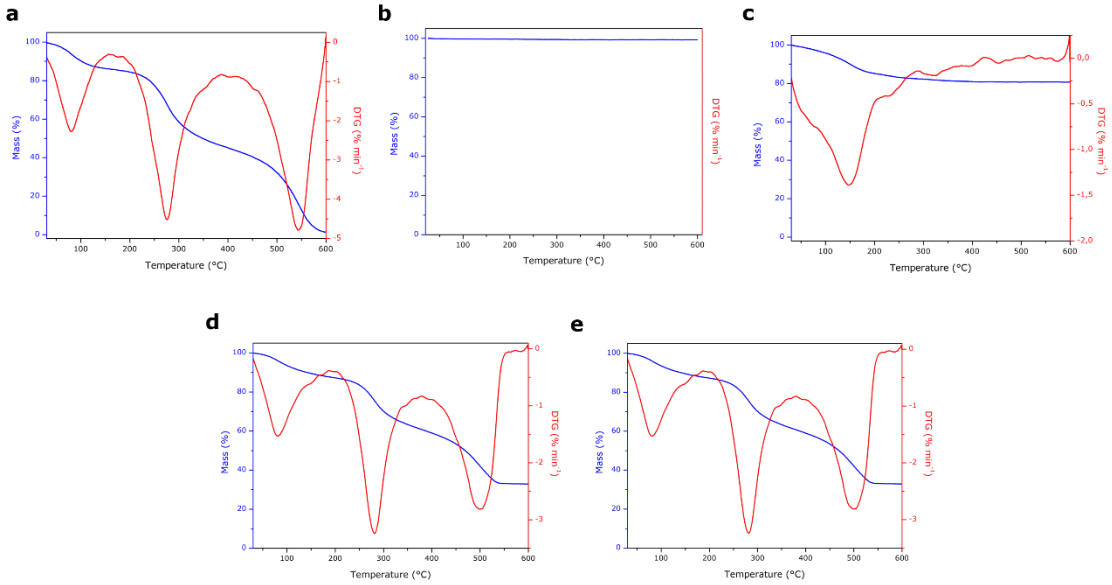

Source: The author (2022).

The TGA curves for the magnetic composites present three well distinguished thermodegradative events. The first degradation event happens in the temperature range of 30.0 – 193.0 °C for the MCCSB-ZA1 and 30.0 – 197.9 °C for the MCCSB-ZA2, with mass losses of 12.60 and 10.91%, respectively, corresponding to the evaporation of moisture in the samples.[182; 183] The major loss of mass for both material happens in the second step of TGA curve which takes place between 193.0 and 398.4 °C for MCCSB-ZA1 and 197.9 and 379.9 °C for MCCSB-ZA2. This event is related to the decomposition of chitosan chain from the matrix of the composite.[184; 185] The last step happens in the temperature range of 398.4 – 600 °C for MCCSB-ZA1, and 379.9 – 600 °C for MCCSB-ZA2, with mass losses of 25.85 and 22.84%, respectively. The magnetic composites present higher quantities of residues, indicates the reinforcement of these composites, MF and ZA, are highly stable when exposed to elevated temperatures, which was already expected from their individual TGA results (Figure 29).

The TGA information of all the analyzed samples is displayed in Table 10.

Table 10 – Thermal events for the analyzed samples.

Sample	Step	Temperature range (°C)	Peak temperature (°C)	Mass loss (%)	Residual Mass (%)
CSB	I	30.0 – 222.4	71.9	11.81	0.0
	II	222.4 – 414.8	287.5	44.59	
	III	414.8 – 600.0	533.4	43.60	
CCSB	I	30.0 – 209.8	80.8	13.98	1.40
	II	209.8 – 402.5	276.0	38.42	
	III	402.5 – 600.0	545.4	46.13	
ZA	I	30.0 – 304.1	149.3	17.69	80.5
CCSB-ZA1	I	30.0 – 169.7	82.74	11.33	14.77
	II	169.7 – 380.9	257.2	50.41	
	III	380.9 – 600.0	431.2	23.67	
CCSB-ZA2	I	30.0 – 161.8	74.9	11.58	15.25
	II	161.8 – 372.6	254.0	49.33	
	III	372.6 – 600.0	434.9	23.94	
MCCSB-ZA1	I	30.0 – 193.0	80.8	12.60	33.20
	II	193.0 – 398.4	279.8	28.53	
	III	398.4 – 600.0	500.4	25.85	
MCCSB-ZA2	I	30.0 – 197.9	88.6	10.91	42.39
	II	197.9 – 379.9	279.4	24.00	
	III	379.9 – 600.0	502.0	22.84	

Source: The author (2022).

4.6 Vibrating sample magnetometry (VSM)

The VSM measures the magnetic moment of the entire sample as a function of applied magnetic field, as well as other information such as coercivity, switching fields, and their distribution.[186] The analyses of VSM were performed in order to determine the variation of the magnetization of the samples in function of the concentration of MF in the composites.

The curves of magnetization versus magnetic field for the applied samples of CCSB, ZA, and MF are illustrated in Figure 33.

Figure 33 – Magnetization curve for the samples of cross-linked chitosan beads (CCSB), fly ash-based zeolite NaA (ZA), and magnetic fraction from fly ashes (MF).

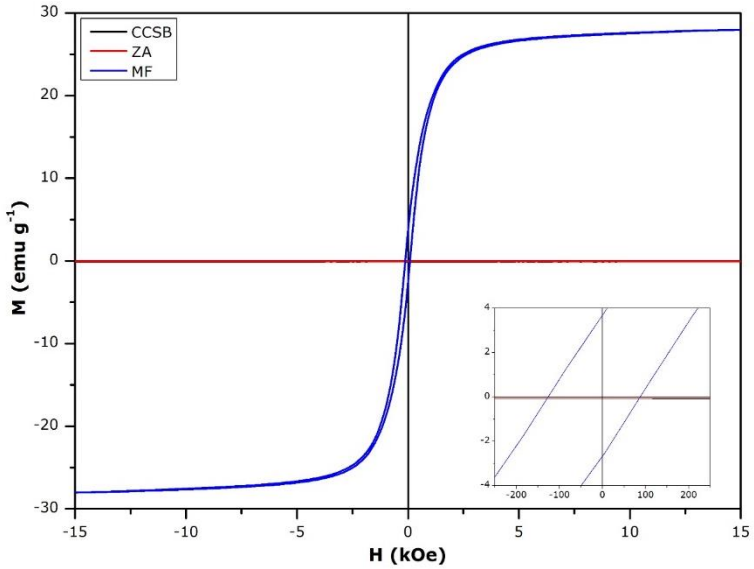

Source: The author (2022).

As expected, Figure 33 – Magnetization curve for the samples of cross-linked chitosan beads (CCSB), fly ash-based zeolite NaA (ZA), and magnetic fraction from fly ashes (MF).only the MF sample magnetization curve in Figure 33 presents a hysteresis character due to the presence of ferromagnetic components.[187]

Considering the magnetic behavior of chitosan and zeolite, the expected behavior of the CCSB-ZA2 beads is similar as it is seen in Figure 34.

Figure 34 – Magnetization curves for the samples of CCSB, ZA, and CCSB-ZA2.

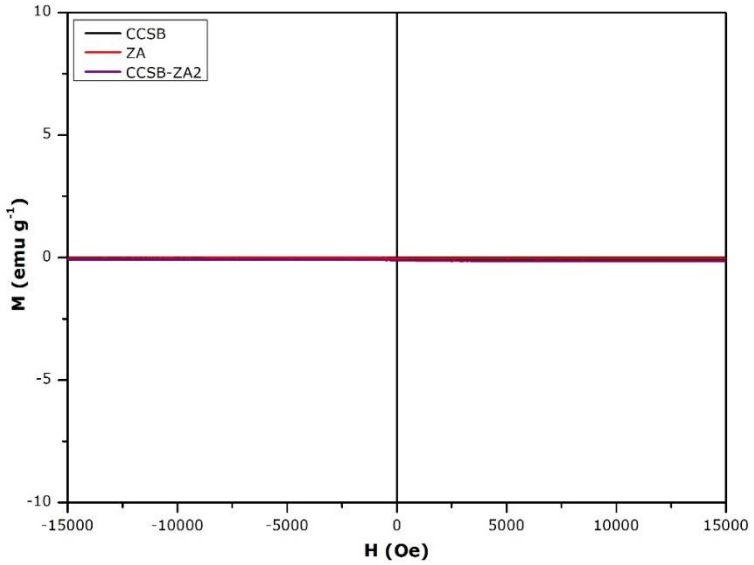

Source: The author (2022).

The magnetization curves for the magnetic composites MCCSB-ZA1 and MCCSB-ZA2 are available in Figure 35.

Figure 35 – Magnetization curves for the MF, CCSB-ZA2, MCCSB-ZA1, and MCCSB-ZA2.

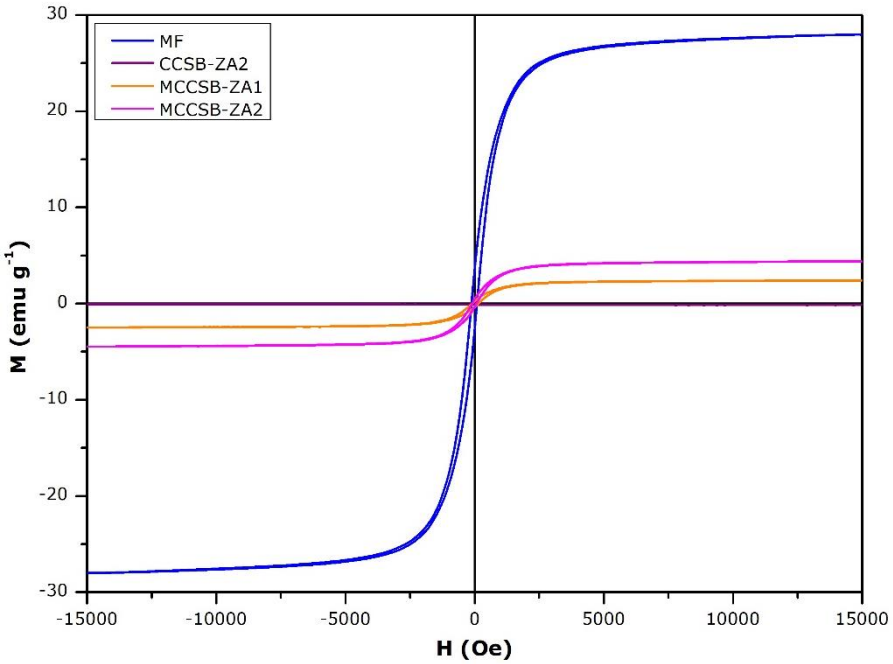

Source: The author (2022).

The magnetization curves for the magnetic composites show similar tendencies when exposed to a magnetic field, but the magnetic response reduces with the reduction of MF concentration in the composites.

Table 11 displays the values obtained in the magnetic analysis for all of the analyzed samples.

Table 11 – Magnetization values of the samples obtained by the VSM analyses at room temperature.

Sample	Ms (emu g^{-1})	hc (Oe)	Mr (emu g^{-1})
CCSB	0	0	0
CCSB-ZA2	0	0	0
ZA	0	0	0
MCCSB-ZA1	2.39	95.0	0.475
MCCSB-ZA2	4.39	102.7	0.266
MF	28.0	126.5	3.69

Source: The author (2022).

In Table 11, it is possible to observe the variation of saturation magnetization in function of the concentration of MF present in the magnetic.[188]

4.7 Water softening tests

First, to evaluate the capability of Ca^{2+}removal from aqueous media, two samples of CCSB were put in contact with an aqueous solution of 110 ppm Ca^{2+} for 1 h. The Ca^{2+} removal results showed no considerable removal of the ions from water, which means that

chitosan does not present significant removal of calcium cations, which was expected once the chitosan have only presents weak interactions with these ions.[21] Therefore, the chitosan will mainly act as support for the zeolite in the composites for process of water softening.

By considering the characterization results, the selected samples to perform the water softening tests were: ZA, CCSB-ZA1, CCSB-ZA2, and MCCSB-ZA2. The mass effect was studied varying the ZA mass in the samples from 10 to 100 mg The obtained results of Ca^{2+} to removal from the samples of hard water are available in Figure 36.

Figure 36 – Water softening results for (a) zeolite NaA, (b) CCSB-ZA1, (c) CCSB-ZA2, and (d) MCCSB-ZA2.

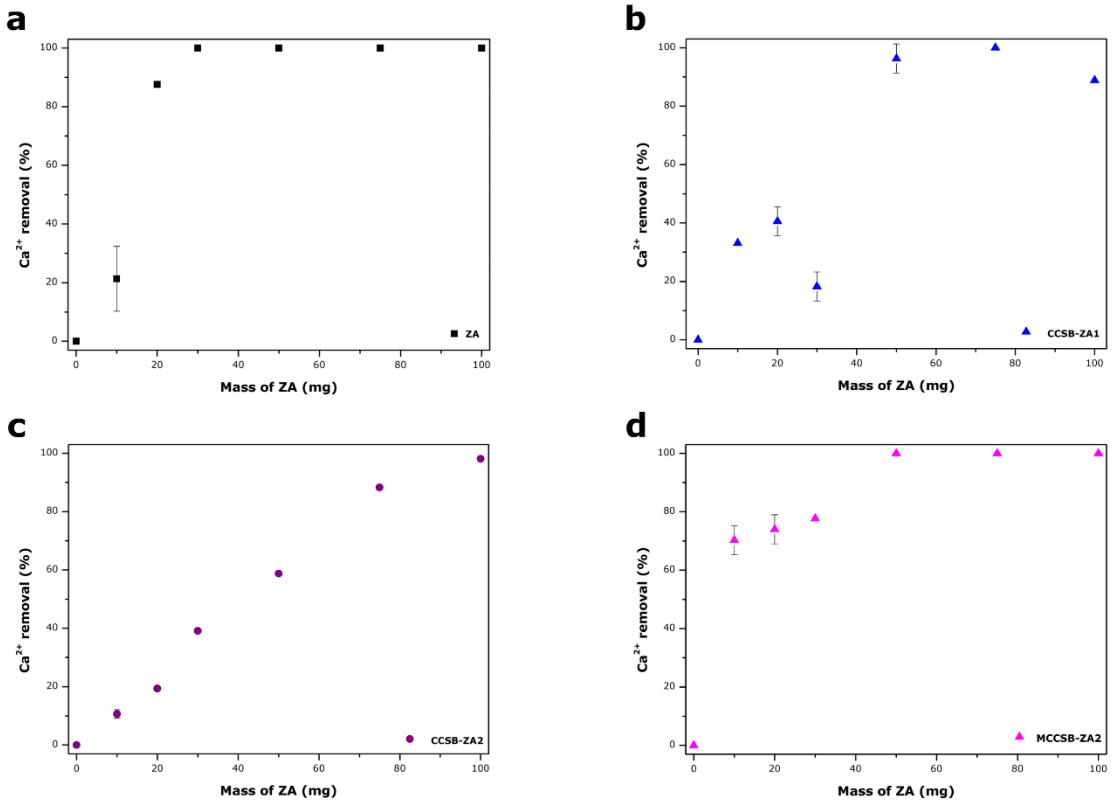

Source: The author (2022).

The percentual values of Ca^{2+} removal obtained for the applied materials are depicted in Table 12

Table 12 – Results of Ca^{2+} removal from the solution after the water softening tests varying the mass of zeolite in the sample.

Mass of Zeolite in the sample / mg	**Ca^{2+} removal / %**			
	ZA	CCSB-ZA1	CCSB-ZA2	MCCSB-ZA2
0	0	0	0	0
10	21.3±11.4	33.1	10.6±1.4	70,3±4.9
20	87.6	40.5±4,9	19.4	73.9±4.9
30	100	18.3±4.9	39.1	77.7
50	100	96.3±4.9	58.7	100
75	100	100	88.3	100
100	100	88.8	98.1	100

Source: The author (2022).

Although the ZA sample presented, in Figure 36a, the expected behavior of removing completely the calcium cations with minor quantity of material used, a few aspects are of interest. It is easily seen in Figure 36 the best softening performance is of the pure zeolite NaA sample, once zeolite in its powder presents more active sites available thanks to its higher surface area for ion exchange than its composites.[16; 189; 190]

As expected, the composites presented intermediary behavior in the cation removal once the concentration of zeolite crystals is reduced because they are dispersed in a polymer. Hence, a higher quantity of zeolite is necessary to achieve to remove completely the hardness. The addition of the MF did not bring any negative interference in the water softening process, and it accomplished the goal of facilitating the removal of the material from the medium.

Table 13 – Values of optimum mass for each sample tested in the water softening tests.

Sample	**Optimum mass of zeolite / mg**	**Ca^{2+} removal / %**
ZA	30	100
MCCSB-ZA2	50	100
CCSB-ZA1	50	96
MCCSB-ZA2	100	100

Source: The author (2022).

From the results of optimum mass of zeolite in Table 13, the MCCSB-ZA2 sample showed the necessity of a higher quantity when compared to the other composites, which can be an indicator of agglomerates or the formation of thicker chitosan layers covering the crystals that can difficult the access of the ions of interest to the active sites.

The water softening tests using the composites showed great potential of these materials in the removal of hardness of water, with complete exchange of calcium ions for sodium ions.

5 CONCLUSIONS

Zeolite NaA was successfully synthesized via hydrothermal route from coal fly ash as the main source of silicon and aluminum. This compound was dispersed in an organic matrix of chitosan, previously purified and widely characterized via XRD and SEM. The composite materials showed effective performance in the removal of Ca^{2+} from aqueous solution. The incorporation of magnetic particles, extracted from fly ash, gave the composites magnetic properties that enabled them to be easily separated from the aqueous media, after the softening processes.

XRD analyses attested the efficiency in the syntheses and also the stability of the crystalline materials when dispersed in the morganic matrix. SEM results showed that the prepared beads have spherical shape, with interconnected porosity, and zeolite crystals homogeneously dispersed in the fibrillar structure of chitosan.

The use of fly ash, a residual product, both as raw material for zeolite synthesis and as a source of magnetic particles, made possible the preparation of low-cost composites together with chitosan, a natural and abundant polymer. The results presented here indicate that the composites present enormous potential to be applied in large scale processes of water softening.

REFERENCES

1 EL-NAHAS, S. *et al*. Facile and affordable synthetic route of nano powder zeolite and its application in fast softening of water hardness. **Journal of Water Process Engineering,** v. 33, p. 101104. Amsterdam: Elsevier, 2020. Disponível em: https://doi.org/10.1016/j.jwpe.2019.101104. Acesso em: 15 jul. 2021.

2 ATI, E. M. *et al*. Water pollution and its relationship to human health: A review. **Eurasian Journal of Biosciences,** v. 14, n. 2, p. 7473-7476. Bangalore: Indian Academy of Sciences, 2020. Disponível em: https://www.proquest.com/openview/c51adca082d0b88769d6b6edd14c5da5/1?pq-origsite=gscholar&cbl=2042720. Acesso em: 15 jul. 2021.

3 SAUVÉ, S. *et al*. Circular economy of water: Tackling quantity, quality and footprint of water. **Environmental Development**, p. 100651. Amsterdam: Elsevier, 2021. Disponível em: https://doi.org/10.1016/j.envdev.2021.100651. Acesso em: 16 jul. 2021.

4 SUZDALEVA, A. *et al*. **Importance of water objects for the sustainable development of megalopolises**. E3S Web of Conferences, p. 04013. Vesennyaya: EDP Sciences, 2021. Disponível em: https://www.researchgate.net/publication/352094096_Importance_of_water_objects_for_the_sustainable_development_of_megalopolises. Acesso em: 16 jul. 2021.

5 TEOW, Y. H.; MOHAMMAD, A. W. New generation nanomaterials for water desalination: A review. **DESALINATION,** v. 451, p. 2-17. Amsterdam: Elsevier, 2019. Disponivel em: https://doi.org/10.1016/j.desal.2017.11.041. Acesso em: 17 ago. 2021.

6 ISMAEL, M. *et al.* Assessing drinking water quality based on physical, chemical and microbial parameters in the Red Sea State, Sudan using a combination of Water Quality Index and Artificial Neural Network Model. **Groundwater for Sustainable Development**, p. 100612. Amsterdam: Elsevier, 2021. Disponível em: https://doi.org/10.1016/j.gsd.2021.100612. Acesso em: 16 jul. 2021.

7 HEGARTY, S. *et al*. Using citizen science to understand river water quality while filling data gaps to meet United Nations Sustainable Development Goal 6 objectives. **Science of the Total Environment,** v. 783. Amsterdam: Elsevier, 2021. Disponível em: https://www.sciencedirect.com/science/article/pii/S0048969721020234. Acesso em: 05 mar. 2022.

8 GATTINONI, P.; SCESI, L. Short review of some methods for groundwater flow assessment in fractured rock masses. **Acque Sotterranee-Italian Journal of Groundwater,** v. 7, n. 3, p. 7-17. Pavia: PAGEpress, 2018. Disponível em: https://doi.org/10.7343/as-2018-342. Acesso em: 05 jan. 2021.

9 ESTERHUYSE, S.; VERMEULEN, D.; GLAZEWSKI, J. Regulations to protect groundwater resources during unconventional oil and gas extraction using fracking. **Wiley**

Interdisciplinary Reviews: Water, v. 6, n. 6, p. 19. New Jersey: Wiley, 2019. Disponível em: https://doi.org/10.1002/wat2.1382. Acesso em: 05 jan. 2022.

10 FAMIGLIETTI, J. S. The global groundwater crisis. **Nature Climate Change,** v. 4, n. 11, p. 945-948. London: Nature Publishing Group, 2014. Disponível em: https://www.nature.com/articles/nclimate2425.pdf. Acesso em: 05 jan. 2022.

11 ADIMALLA, N. *et al*. Appraisal of groundwater quality for drinking and irrigation purposes in Central Telangana, India. **Groundwater for Sustainable Development,** v. 10, p. 100334. Amsterdam: Elsevier, 2020. Disponível em: https://doi.org/10.1016/j.gsd.2020.100334. Acesso em: 16 jul. 2021.

12 SULAIMAN, S. K. *et al*. Which Type of Water Is Recommended for Patients with Stone Disease (Hard or Soft Water, Tap or Bottled Water): Evidence from a Systematic Review over the Last 3 Decades. **Current Urology Reports,** v. 21, n. 1, p. 6. New York: Springer, 2020. Disponível em: https://pubmed.ncbi.nlm.nih.gov/32016596/. Acesso em: 15 jul. 2021.

13 SALAM, M. A. *et al*. Effective decontamination of Ca2+ and Mg2+ hardness from groundwater using innovative muscovite based sodalite in batch and fixed-bed column studies; dynamic and equilibrium studies. **Journal of Contaminant Hydrology,** v. 241, p. 103817. Amsterdam: Elsevier, 2021. Disponível em: https://www.sciencedirect.com/science/article/pii/S0169772221000565. Acesso em: 15 jul. 2021.

14 LIU, W. *et al*. Evaluation of groundwater hardness removal using activated clinoptilolite. **Environmental Science and Pollution Research,** v. 27, n. 15, p. 17541-17549. New York: Springer, 2020. Disponível em: https://doi.org/10.1007/s11356-019-06193-9. Acesso em: 15 jul. 2021.

15 GIESE, M.; BARTHEL, R. Review: Saltwater intrusion in fractured crystalline bedrock. **Hydrogeology Journal,** v. 29, n. 7, p. 2313-2328. New York: Springer, 2021. Disponível em: https://link.springer.com/article/10.1007/s10040-021-02396-y. Acesso em: 05 jan. 2022.

16 ARAGAW, T. A.; AYALEW, A. A. Removal of water hardness using zeolite synthesized from Ethiopian kaolin by hydrothermal method. **Water Practice and Technology,** v. 14, n. 1, p. 145-159. London: IWA Publishing, 2019. Disponível em: https://iwaponline.com/wpt/article/14/1/145/65064/Removal-of-water-hardness-using-zeolite. Acesso em: 15 jul. 2021.

17 COLLINS, F. *et al*. A critical review of waste resources, synthesis, and applications for Zeolite LTA. **Microporous and Mesoporous Materials**, p. 109667. Amsterdam: Elsevier, 2019. Disponível em: https://www.sciencedirect.com/science/article/abs/pii/S1387181119305244. Acesso em: 15 jul. 2021.

18 WILLIS, S. *et al*. Water to prevent kidney stones: tap vs bottled; soft vs hard–does it matter? **BJU international,** v. 124, n. 6, p. 905-906. New York: Wiley, 2019. Disponível em: https://pubmed.ncbi.nlm.nih.gov/31310699/. Acesso em: 15 jul. 2021.

19 ALAHMMED, L. M. *et al*. Scanning electron microscopy study of hair shaft changes related to hardness of water. **Indian Journal of Dermatology, Venereology, and Leprology,** v. 83, n. 6, p. 740. New York: Scientific Scholar, 2017. Disponível em: https://ijdvl.com/scanning-electron-microscopy-study-of-hair-shaft-changes-related-to-hardness-of-water/. Acesso em: 15 jul. 2021.

20 LIANG, J. *et al*. The use of graphene oxide membranes for the softening of hard water. **Science China Technological Sciences,** v. 57, n. 2, p. 284-287. New York: Springer, 2014. Disponível em: https://doi.org/10.1007/s11431-014-5467-7. Acesso em: 27 jul. 2021.

21 ALI, K.; Hassan, M.; Elnashar, M.. Development of functionalized carrageenan, chitosan and alginate as polymeric chelating ligands for water softening. **International Journal of Environmental Science and Technology,** v. 14, n. 9, p. 2009-2014. New York: Springer, 2017. Disponível em: https://link.springer.com/article/10.1007/s13762-017-1298-y. Acesso em: 15 jul. 2021.

22 MAZUMDER, M.J.A. A Review of Green Scale Inhibitors: Process, Types, Mechanism and Properties. **COATINGS,** v. 10, n. 10. Basel: MPDI, 2020. Disponível em: https://www.mdpi.com/2079-6412/10/10/928. Acesso em: 17 aug. 2021.

23 AL-HADIDI, M.M.; ATEF, A.; R.A. Impact of Over-Pumping on the Groundwater Quality of the Dead Sea Basin/Jordan. **Current World Environment,** v. 8, n. 3, p. 365. Madhya Pradesh: CWE Journal, 2013. Disponível em: http://dx.doi.org/10.12944/CWE.8.3.04. Acesso em: 15 jul. 2021.

24 GHADAMNAN, E.; NABAVI, S.R.; ABBASI, M. Nano LTA Zeolite in Water Softening Process: Synthesis, Characterization, Kinetic studies and process optimization by Response Surface Methodology (RSM). **Journal of Water and Environmental Nanotechnology,** v. 4, n. 2, p. 119-138. Babol: JWEN, 2019. Disponível em: http://www.jwent.net/article_35822.html. Acesso em: 15 jul. 2021.

25 SHAHMIRZADI, M.A. *et al*. Significance, evolution and recent advances in adsorption technology, materials and processes for desalination, water softening and salt removal. **Journal of Environmental Management,** v. 215, p. 324-344. Amsterdam: Elsevier, 2018. Disponível em: https://www.sciencedirect.com/science/article/pii/S0301479718302676. Acesso em: 26 jul. 2021.

26 SALEEM, H. *et al*. Recent advances in nanofibrous membranes: Production and applications in water treatment and desalination. **DESALINATION,** v. 478. Amsterdam: Elsevier, 2020. Disponível em: https://www.sciencedirect.com/science/article/abs/pii/S0011916419314353. Acesso em: 27 jul. 2021.

27 PANAGOPOULOS, A.; HARALAMBOUS, K. J. Environmental impacts of desalination and brine treatment - Challenges and mitigation measures. **Marine Pollution Bulletin,** v. 161. Amsterdam: Elsevier, 2020. Disponível em: https://pubmed.ncbi.nlm.nih.gov/33128985/. Acesso em: 05 jan. 2022.

28 BEEFTINK, M. *et al*. Carbon footprint of drinking water softening as determined by life cycle assessment. **Journal of Cleaner Production,** v. 278, p. 123925. Amsterdam: Elsevier, 2021. Disponível em: https://www.sciencedirect.com/science/article/pii/S0959652620339706. Acesso em: 05 jan. 2022.

29 TANG, C. *et al*. Softening of drinking water by the pellet reactor - Effects of influent water composition on calcium carbonate pellet characteristics. **Science of The Total Environment,** v. 652, p. 538-548. Amsterdam: Elsevier, 2019. Disponível em: https://www.sciencedirect.com/science/article/pii/S0048969718340403. Acesso em: 05 jan. 2022.

30 TANG, C.; MERKS, C. W.; ALBRECHTSEN, H. J.. Water softeners add comfort and consume water – comparison of selected centralised and decentralised softening technologies. **Water Supply,** v. 19, n. 7, p. 2088-2097. London: IWA Publishing, 2019. Disponível em: https://doi.org/10.2166/ws.2019.088. Acesso em: 05 jan. 2022.

31 ANIS, S.F.; HASHAIKEH, R.; HILAL, N. Functional materials in desalination: a review. **Desalination,** v. 468, p. 114077. Amsterdam: Elsevier, 2019. Disponível em: https://www.sciencedirect.com/science/article/abs/pii/S0011916419311385. Acesso em: 16 jul. 2021.

32 QASIM, M. *et al*. Reverse osmosis desalination: A state-of-the-art review. **Desalination,** v. 459, p. 59-104. Amsterdam: Elsevier, 2019. Disponível em: https://www.sciencedirect.com/science/article/abs/pii/S0011916418325037. Acesso em: 15 jul. 2021.

33 RIOYO, J. *et al*. Research on 'high-pH precipitation treatment' for RO concentrate minimization and salt recovery in a municipal groundwater desalination facility. **Desalination,** v. 439, p. 168-178. Amsterdam: Elsevier 2018. Disponível em: https://www.sciencedirect.com/science/article/pii/S001191641732204X. Acesso em: 05 jan. 2022.

34 SIM, L.N. *et al*. A review of fouling indices and monitoring techniques for reverse osmosis. **Desalination,** v. 434, p. 169-188. Amsterdam: Elsevier, 2018. Disponível em: https://www.sciencedirect.com/science/article/abs/pii/S0011916417306410. Acesso em: 15 jul. 2021.

35 KAZI, S.N. Fouling and fouling mitigation of calcium compounds on heat exchangers by novel colloids and surface modifications. **REVIEWS IN CHEMICAL ENGINEERING,** v. 36, n. 6, p. 653-685. Munich: De Gruyter, 2020. Disponível em: https://www.degruyter.com/document/doi/10.1515/revce-2017-0076/html. Acesso em: 17 aug. 2021.

36 WANG, L. *et al.* Microwave synthesis of NaA zeolite membranes on coarse macroporous α-Al2O3 tubes for desalination. **Microporous and Mesoporous Materials,** v. 306, p. 110360. Amsterdam: Elsevier, 2020. Disponível em: https://www.sciencedirect.com/science/article/abs/pii/S1387181120303632. Acesso em: 15 jul. 2021.

37 JIN, H.; YU, Y.; CHEN, X. Membrane-based electrochemical precipitation for water softening. **Journal of Membrane Science,** v. 597, p. 117639. Amsterdam: Elsevier, 2020. Disponível em: https://www.sciencedirect.com/science/article/pii/S0376738819323889. Acesso em: 22 dez. 2021.

38 WANG, Y. *et al*. Effective removal of calcium and magnesium sulfates from wastewater in the rare earth industry. **RSC advances,** v. 9, n. 58, p. 33922-33930. Cambridge: RSC 2019. Disponível em: https://pubs.rsc.org/en/content/articlelanding/2019/RA/C9RA05615G. Acesso em: 22 dez. 2021.

39 YU, Y. *et al*. Current pulsated electrochemical precipitation for water softening. **Industrial & Engineering Chemistry Research,** v. 57, n. 18, p. 6585-6593. Washington: ACS publications, 2018. Disponível em: https://pubs.acs.org/doi/10.1021/acs.iecr.8b00448. Acesso em: 22 dez. 2021.

40 ENTEZARI, M.H.; TAHMASBI, H. Water softening by combination of ultrasound and ion exchange. **Ultrasonics sonochemistry,** v. 16, n. 3, p. 356-360. Amsterdam: Elsevier, 2009. Disponível em: https://www.sciencedirect.com/science/article/abs/pii/S1350417708001582?via%3Dihub. Acesso em: 22 dez. 2021.

41 HU, M. *et al*. Catalytic reduction for water treatment. **Frontiers of Environmental Science & Engineering,** v. 12, n. 1, p. 1-18. New York: Springer, 2018. Disponível em: https://link.springer.com/article/10.1007/s11783-017-0972-0. Acesso em: 22 dez. 2021.

42 LUK, G.; AU-YEUNG, W. Experimental investigation on the chemical reduction of nitrate from groundwater. **Advances in environmental research,** v. 6, n. 4, p. 441-453. Amsterdam: Elsevier, 2002. Dispnível em: https://www.sciencedirect.com/science/article/abs/pii/S1093019101000727. Acesso em: 22 dez. 2021.

43 MOGHADDAM, S.S.; MOGHADDAM, M.A.; ARAMI, M. Coagulation/flocculation process for dye removal using sludge from water treatment plant: optimization through response surface methodology. **Journal of hazardous materials,** v. 175, n. 1-3, p. 651-657. Amsterdam: Elsevier, 2010. Disponível em: https://www.sciencedirect.com/science/article/abs/pii/S0304389409017099. Acesso em: 22 dez. 2021.

44 PRAKASH, N.;V. SOCKAN;P. JAYAKARAN. Waste water treatment by coagulation and flocculation. **International Journal of Engineering Science and Innovative Technology (IJESIT),** v. 3, n. 2, p. 479-484. Bhopal: IJESIT, 2014. Disponível em: https://www.researchgate.net/profile/Prakash-Nanjan-Bellie-2/publication/273638362_Waste_Water_Treatment_by_Coagulation_and_Flocculation/links/556eb5ec08aec2268308cbbc/Waste-Water-Treatment-by-Coagulation-and-Flocculation.pdf. Acesso em: 22 dez. 2021.

45 ARRIGO, I. *et al*. Use of zeolitized pumice waste as a water softening agent. **Journal of hazardous materials,** v. 147, n. 1-2, p. 513-517. Amsterdam: Elsevier, 2007. Disponível em: https://linkinghub.elsevier.com/retrieve/pii/S0304389407001069. Acesso em: 22 dez. 2021.

46 PERVOV, A.; EFREMOV, R. Membrane techniques in groundwater treatment. **IOP Conference Series: Materials Science and Engineering,** v. 365, n. 6, p. 062025, 2018/06 2018.. Disponível em: http://dx.doi.org/10.1088/1757-899X/365/6/062025. Acesso em: 15 jul. 2021.

47 SUWAILEH, W.; JOHNSON, D.; HILAL, N. Membrane desalination and water re-use for agriculture: State of the art and future outlook. **DESALINATION,** v. 491. Amsterdam: Elsevier, 2020. Disponível em: https://linkinghub.elsevier.com/retrieve/pii/S0011916420310213. Acesso em: 17 aug. 2021.

48 TANG, F. *et al*. Preparation of porous materials with controlled pore size and porosity. **Journal of the European Ceramic Society,** v. 24, n. 2, p. 341-344. Amsterdam: Elsevier, 2004. Disponível em: https://www.sciencedirect.com/science/article/pii/S0955221903002231. Acesso em: 06 jan. 2022.

49 ZDRAVKOV, B. *et al*. Pore classification in the characterization of porous materials: A perspective. **Open Chemistry,** v. 5, n. 2, p. 385-395. New York: Springer, 2007. Disponível em: https://doi.org/10.2478/s11532-007-0017-9. Acesso em: 06 jan. 022.

50 BARTON, T.J. *et al*. Tailored Porous Materials. **Chemistry of Materials,** v. 11, n. 10, p. 2633-2656. United States of America: OSTI, 1999. Disponível em: https://doi.org/10.1021/cm9805929. Acesso em: 06 jan. 2022.

51 AQUINO, C.; MASCHMEYER, T. Chapter 1 - A New Family of Mesoporous Oxides—Synthesis, Characterisation and Applications of TUD-1. *In:* **Ordered Porous Solids,** p.3-30. Amsterdam: Elsevier, 2009. Disponível em: https://www.sciencedirect.com/science/article/pii/B9780444531896000019. Acesso em: 07 jan. 2022.

52 SANTOS, A.V. *et al*. O incrível mundo dos materiais porosos–características, propriedades e aplicações. **Química nova na escola,** v. 38 São Paulo: SBQ, 2016. Disponível em: http://qnesc.sbq.org.br/online/qnesc38_1/03-QS-75-14.pdf. Acesso em: 07 jan. 2022.

53 XIN, Y. *et al*. Continuous flow synthesis of porous materials. **Chinese Chemical Letters,** v. 31, n. 6, p. 1448-1461. Amsterdam: Elsevier, 2020. Disponível em: https://www.sciencedirect.com/science/article/pii/S1001841719306011. Acesso em: 08 jan. 2022.

54 CAI, G. *et al*. Metal–Organic Framework-Based Hierarchically Porous Materials: Synthesis and Applications. **Chemical Reviews,** v. 121, n. 20, p. 12278-12326. Washington: ACS Publications, 2021. Disponível em: https://doi.org/10.1021/acs.chemrev.1c00243. Acesso em: 06 jan. 2022.

55 LI, J.; SCULLEY, R.; ZHOU, H. Metal–Organic Frameworks for Separations. **Chemical Reviews,** v. 112, n. 2, p. 869-932. Washington: ACS Publications, 2012. Disponível em: https://doi.org/10.1021/cr200190s. Acesso em: 08 jan. 2022.

56 ROUQUEROL, J. *et al*. Recommendations for the characterization of porous solids (Technical Report). **Pure and Applied Chemistry,** v. 66, n. 8, p. 1739-1758. Munich: De Gruyter, 1994. Disponível em: https://www.degruyter.com/document/doi/10.1351/pac199466081739/html. Acesso em: 30 ago. 2021.

57 THOMMES, M. *et al*. Physisorption of gases, with special reference to the evaluation of surface area and pore size distribution (IUPAC Technical Report). **Pure and applied chemistry,** v. 87, n. 9-10, p. 1051-1069. Munich: De Gruyter, 2015. Disponpivel em: https://www.degruyter.com/document/doi/10.1515/pac-2014-1117/html. Acesso em: 30 ago. 2021.

58 GOETTMANN, F.;SANCHEZ, C. How does confinement affect the catalytic activity of mesoporous materials? **Journal of Materials Chemistry,** v. 17, n. 1, p. 24-30. Cambridge: RSB Publishing, 2007. Disponível em: http://dx.doi.org/10.1039/B608748P. Acesso em: 31 jul. 2021.

59 CHEUNG, O.;HEDIN, N. Zeolites and related sorbents with narrow pores for CO2 separation from flue gas. **RSC Advances,** v. 4, n. 28, p. 14480-14494. Cambridge: RSB Publishing, 2014. Disponível em: http://dx.doi.org/10.1039/C3RA48052F. Acesso em: 31 jul. 2021.

60 BANDURA, L. *et al*. Zeolites in Phenol Removal in the Presence of Cu (II) Ions—Comparison of Sorption Properties after Chitosan Modification. **Materials,** v. 13, n. 3, p. 643. Basel: MPDI, 2020. Disponível em: https://www.mdpi.com/1996-1944/13/3/643. Acesso em: 15 jul. 2021.

61 Cronstedt, A.F. **Rön och beskrifning om en obekant bärg art, som kallas Zeolites**. Stockholm: Svenska, 1756.

62 FLANIGEN, E.M.; BROACH, R. W.; WILSON, S. T. Zeolites in industrial separation and catalysis. **Chapter,** v. 1, p. 1-26. New York: Wiley, 2010. Disponível em: https://onlinelibrary.wiley.com/doi/book/10.1002/9783527629565. Acesso em: 30 jul. 2021.

63 LIMA, R.C. *et al*. Zeolites: What Are They?. *In:* **Environmentally Friendly Zeolites**, p.1-19. New York: Springer, 2019. Disponível em: https://link.springer.com/chapter/10.1007/978-3-030-19970-8_1. Acesso em: 07 ago. 2021.

64 PAYRA, P.; DUTTA, P.K. Zeolites: a primer. *In*: **Handbook of zeolite science and technology**, p.13-36. London: CRC press, 2003. Disponível em: https://www.taylorfrancis.com/chapters/edit/10.1201/9780203911167-7/zeolites-primer-pramatha-payra-prabir-dutta. Acesso em: 07 ago. 2021.

65 GHOBARKAR, H.; SCHAF, O.; GUTH, U. Zeolites - from kitchen to space. **Progress in Solid State Chemistry,** v. 27, n. 2-4, p. 29-73. Amsterdam: Elsevier, 1999. Disponível em:

https://www.sciencedirect.com/science/article/abs/pii/S0079678600000029. Acesso em: 07 aug. 2021.

66 MASTERS, A.F.; MASCHMEYER, T. Zeolites - From curiosity to cornerstone. **Microporous And Mesoporous Materials,** v. 142, n. 2-3, p. 423-438. Amsterdam: Elsevier, 2011. Disponível em: https://linkinghub.elsevier.com/retrieve/pii/S1387181110004592. Acesso em: 10 jul. 2021.

67 PENG, P. *et al*. Unraveling the diffusion properties of zeolite-based multicomponent catalyst by combined gravimetric analysis and IR spectroscopy (AGIR). **ACS Catalysis,** v. 10, n. 12, p. 6822-6830. Washington: ACS Publications, 2020. Disponível em: https://pubs.acs.org/doi/10.1021/acscatal.0c01021. Acesso em: 15 jul. 2021.

68 ZHANG, K. *et al*. Organotemplate-Free β Zeolites: From Zeolite Synthesis to Hierarchical Structure Creation. **ACS Omega,** v. 3, n. 12, p. 18935-18942. Washington: ACS Publications, 2018. Disponível em: https://doi.org/10.1021/acsomega.8b02762. Acesso em: 15 jul. 2021.

69 GHOBARKAR, H.; SCHAF, O.; GUTH, U. Zeolites - from kitchen to space. **Progress in Solid State Chemistry,** v. 27, n. 2-4, p. 29-73. Amsterdam: Elsevier, 1999. Disponível em: https://www.sciencedirect.com/science/article/abs/pii/S0079678600000029. Acesso em: 07 aug. 2021.

70 WISE, W.S. **Minerals - Zeolites**, *In:* Encyclopedia of Geology, p. 591-600. Amsterdam: Elsevier, 2005. Disponível em: https://www.sciencedirect.com/science/article/pii/B9780124095489029067?via%3Dihub. Acesso em: 16 ago. 2021.

71 LIU, L.J.; LI, J.H.; WANG, X. Investigation on design of porous structure composite material monoliths based on 4A zeolite/magnesia phosphate. **Chemical Physics Letters,** v. 731. Amsterdam: Elsevier, 2019. Disponível em: https://www.sciencedirect.com/science/article/abs/pii/S0009261419305883?via%3Dihub. Acesso em: 08 jan. 2022.

72 KRÓL, M. Natural vs. Synthetic Zeolites. **Crystals,** v. 10, n. 7, p. 622. Basel: MPDI, 2020. Disponível em: https://www.mdpi.com/2073-4352/10/7/622. Acesso em: 10 jan. 2022.

73 KHALEQUE, A. *et al*. Zeolite synthesis from low-cost materials and environmental applications: A review. **Environmental Advances,** v. 2, p. 100019. Amsterdam: Elsevier, 2020. Disponível em: https://www.researchgate.net/publication/345814858_Zeolite_synthesis_from_low-cost_materials_and_environmental_applications_A_review. Acesso em: 11 jan. 2022.

74 KOOHSARYAN, E.; ANBIA, M.. Nanosized and hierarchical zeolites: A short review. **Chinese Journal of Catalysis,** v. 37, n. 4, p. 447-467. Amsterdam: Elsevier, 2016. Disponível em: https://www.sciencedirect.com/science/article/pii/S1872206715610385. Acesso em: 07 aug. 2021.

75 BORTOLATTO, L.B. *et al*. Synthesis and characterization of Y zeolites from alternative silicon and aluminium sources. **Microporous and Mesoporous Materials,** v. 248, p. 214-221. Amsterdam: Elsevier, 2017. Disponível em: https://www.sciencedirect.com/science/article/pii/S1387181117302706. Acesso em: 23 jul. 2021.

76 ROZHKOVSKAYA, A.; RAJAPAKSE, J.; MILLAR, G.J. Synthesis of high-quality zeolite LTA from alum sludge generated in drinking water treatment plants. **Journal of Environmental Chemical Engineering,** v. 9, n. 2, p. 104751. Amsterdam: Elsevier, 2021. Disponível em: https://doi.org/10.1016/j.jece.2020.104751. Acesso em: 15 jul. 2021.

77 MAGHfiRAH, A. *et al*. A review on the green synthesis of hierarchically porous zeolite. **Materials Today Chemistry,** v. 17, p. 100348. Amsterdam: Elsevier, 2020. Disponível em: https://doi.org/10.1016/j.mtchem.2020.100348. Acesso em: 15 jul. 2021.

78 BORTOLATTO, L.B. *et al*. Synthesis and characterization of Y zeolites from alternative silicon and aluminium sources. **Microporous and Mesoporous Materials,** v. 248, p. 214-221. Amsterdam: Elsevier, 2017. Disponível em: https://www.sciencedirect.com/science/article/pii/S1387181117302706. Acesso em: 26 ago. 2021.

79 ZHANG, C.;S. LI;S. BAO. Sustainable synthesis of ZSM-5 zeolite from rice husk ash without addition of solvents. **Waste and Biomass Valorization,** v. 10, n. 10, p. 2825-2835. New York: Springer, 2019. Disponível em: https://link.springer.com/article/10.1007/s12649-018-0356-0. Acesso em: 30 ago. 2021.

80 KLUNK, M.A. *et al*. Synthesis of ZSM-5 Zeolite from Metakaolin and Rice Husk Ash to CO2 Adsorption. **ECS Journal of Solid State Science and Technology,** v. 10, n. 1, p. 013001. Lausanne: Frontiers Media, 2021. Disponível em: https://www.frontiersin.org/articles/10.3389/fchem.2019.00505/full. Acesso em: 15 jul. 2021.

81 HUI, K.; CHAO, C.Y.H. Effects of step-change of synthesis temperature on synthesis of zeolite 4A from coal fly ash. **Microporous and Mesoporous Materials,** v. 88, n. 1-3, p. 145-151. Amsterdam: Elsevier, 2006. Disponível em: https://www.sciencedirect.com/science/article/pii/S1387181105004270. Acesso em: 15 jul. 2021.

82 YAMAURA, M.; FUNGARO, D.A. Synthesis and characterization of magnetic adsorbent prepared by magnetite nanoparticles and zeolite from coal fly ash. **Journal of materials science,** v. 48, n. 14, p. 5093-5101. New York: Springer, 2013. Disponível em: https://www.ipen.br/biblioteca/2013/18832.pdf. Acesso em: 30 ago. 2021.

83 SUPELANO, G. *et al*. Study of fly ash based zeolite by using slow positrons. **Materials Science and Engineering: B,** v. 263, p. 114890. Amsterdam: Elsevier, 2021. Disponível em: https://www.sciencedirect.com/science/article/pii/S0921510720303974. Acesso em: 31 out. 2021.

84 GOLLAKOTA, A.R. *et al*. Synthesis of novel ZSM-22 zeolite from Taiwanese coal fly ash for the selective separation of Rhodamine 6G. **Journal of Materials Research and Technology,** v. 9, n. 6, p. 15381-15393. Amsterdam: Elsevier, 2020. Disponível em: https://doaj.org/article/d5d4608634c8443a9047e552c8c8fb58. Acesso em: 23 jul. 2021.

85 KIRDECILER, S.K.;AKATA, B. One pot fusion route for the synthesis of zeolite 4A using kaolin. **Advanced Powder Technology,** v. 31, n. 10, p. 4336-4343. Amsterdam: Elsevier, 2020. Disponível em: https://www.sciencedirect.com/science/article/pii/S0921883120304313. Acesso em: 23 jul. 2021.

86 BESSA, R. A. *et al*. Kaolin-based magnetic zeolites A and P as water softeners. **Microporous and Mesoporous materials,** v. 245, p. 64-72. Amsterdam: Elsevier, 2017. Disponível em: https://www.sciencedirect.com/science/article/pii/S1387181117301610. Acesso em: 05 aug. 2021.

87 LOIOLA, A.R. **Diagênese acelerada de caulim à zeólita NaA para uso no abrandamento de águas** (Dissertação). Fortaleza , 2006. Disponível em: https://repositorio.ufc.br/bitstream/riufc/943/3/2006_dis_Ad Loiola.pdf. Acesso em: 05 ago. 2021.

88 SUN, L. *et al*. Controlled synthesis of Zeolite adsorbent from low-grade diatomite: A case study of self-assembled sodalite microspheres. **Journal of Environmental Sciences,** v. 91, p. 92-104. Amsterdam: Elsevier, 2020. Disponível em: https://www.sciencedirect.com/science/article/pii/S1001074220300061. Acesso em: 23 jul. 2021.

89 PALOMARES-HERNANDEZ, A.; MALDONADO, Y.G.; ESPEJEL-AYALA, F. Sustainable route for the synthesis of SAPO-34 zeolites. **Journal of Solid State Chemistry,** v. 288, p. 121442. Amsterdam: Elsevier, 2020. Disponível em: https://www.sciencedirect.com/science/article/pii/S0022459620302723. Acesso em: 23 jul. 2021.

90 WANG, C. *et al*. High value-added applications of coal fly ash in the form of porous materials: A review. **Ceramics International,** v. 47, n. 16, p. 22302-22315. Amsterdam: Elsevier, 2021. Disponível em: https://www.sciencedirect.com/science/article/pii/S0272884221014565. Acesso em: 09 ago. 2021.

91 POUR, A.A. *et al*. Adsorption separation of CO2/CH4 on the synthesized NaA zeolite shaped with montmorillonite clay in natural gas purification process. **Journal of Natural Gas Science and Engineering,** v. 36, p. 630-643. Amsterdam: Elsevier, 2016. Disponível em: https://www.sciencedirect.com/science/article/pii/S1875510016308101. Acesso em: 15 jul. 2021.

92 NETTO, M.S. *et al.* Analysis of adsorption isotherms of Ag+, Co+ 2, and Cu+ 2 onto zeolites using computational intelligence models. **Journal of Environmental Chemical Engineering**, p. 104960. Amsterdam: Elsevier, 2020. Disponível em:

https://www.sciencedirect.com/science/article/pii/S2213343720313099. Acesso em: 15 jul. 2021.

93 BACARIZA, M.C. *et al*. Tuning Zeolite Properties towards CO2 Methanation: An Overview. **ChemCatChem,** v. 11, n. 10, p. 2388-2400. Nova Jersey: John Wiley & Sons, 2019. Disponível em: https://chemistry-europe.onlinelibrary.wiley.com/doi/abs/10.1002/cctc.201900229. Acesso em: 10 jan. 2022.

94 KINČL, J. *et al*. Characteristics of ion exchange and filtration processes in the zeolite-enhanced membrane microfiltration. **Desalination and Water Treatment,** v. 14, n. 1-3, p. 21-29. London: Taylor & Francis Group, 2010. Disponível em: https://doi.org/10.5004/dwt.2010.1007. Acesso em: 10 jan. 2022.

95 DELIERE, L. *et al*. Adsorption in heterogeneous porous media: hierarchical and composite solids. **Microporous and Mesoporous Materials,** v. 229, p. 145-154. Amsterdam: Elsevier, 2016. Disponível em: https://www.sciencedirect.com/science/article/pii/S1387181116301032. Acesso em: 31 jul. 2021.

96 WU, L. *et al*. Hierarchically structured porous materials: Synthesis strategies and applications in energy storage. **National Science Review,** v. 7, p. 1667-1701. Oxford: Oxford University Press, 2020. Disponível em: https://academic.oup.com/nsr/article/7/11/1667/5896477?login=true. Acesso em: 31 jul. 2021.

97 ANDERSON, M.W. *et al*. Hierarchical pore structures through diatom zeolitization. **Angewandte Chemie International Edition,** v. 39, n. 15, p. 2707-2710. New York: Wiley, 2000. Disponível em: https://onlinelibrary.wiley.com/doi/abs/10.1002/1521-3773%2820000804%2939%3A15%3C2707%3A%3AAID-ANIE2707%3E3.0.CO%3B2-M. Acesso em: 31 jul. 2021.

98 SUN, M. *et al*. Hierarchically porous materials: synthesis strategies and emerging applications. **Frontiers of Chemical Science and Engineering,** v. 10, n. 3, p. 301-347. New York: Springer, 2016. Disponível em: https://link.springer.com/article/10.1007/s11705-016-1578-y. Acesso em: 30 ago. 2021.

99 ANGGITA, R.W. *et al*. **The influence of hydrothermal temperature and time toward crystallinity of zeolite X supported on glass wool for CO2 adsorption**. AIP Conference Proceedings: AIP Publishing LLC. 020094 p. Melville: AIP Publishing LLC, 2016. Disponível em: https://aip.scitation.org/doi/abs/10.1063/1.4945548. Acesso em: 30 ago. 2021.

100 OLIVEIRA, E.S. *et al*. Zeólita NaA sintetizada sobre fibra de vidro como estratégia para otimização do abrandamento de águas duras. **Química Nova**, p. 7. São Paulo: SBQ, 2021. Disponível em: https://www.scielo.br/j/qn/a/vPzpTMvPjtgcRmjbfs7mXTs/. Acesso em: 30 fev. 2022.

101 YADAV, H.M. *et al*. Cellulose Nanofiber Composite with Bimetallic Zeolite Imidazole Framework for Electrochemical Supercapacitors. **Nanomaterials,** v. 11, n. 2, p. 395. Basel: MPDI, 2021. Disponível em: https://www.mdpi.com/2079-4991/11/2/395. Acesso em: 30 ago. 2021.

102 BESSA, R.A. *et al*. Hierarchical zeolite based on multiporous zeolite A and bacterial cellulose: An efficient adsorbent of Pb2+. **Microporous and Mesoporous Materials,** v. 312, p. 110752. Amsterdam: Elsevier, 2021. Disponível em: https://www.sciencedirect.com/science/article/pii/S1387181120307526?via%3Dihub. Acesso em: 03 jan. 2022.

103 BESSA, R.A. *et al*. Hierarchization of Zeolites A and X Using Bacterial Cellulose as Macroporous Support. **Journal of the Brazilian Chemical Society**, v. 32, n. 9. Campinas: Scielo, 2021. Disponível em: https://www.scielo.br/j/jbchs/a/Xdr4Nx3XwbVPk8JHD3QDjvv/. Acesso em: 02 jan. 2022.

104 DJELAD, A. *et al*. Sorption of Cu (II) ions on chitosan-zeolite X composites: Impact of gelling and drying conditions. **Molecules,** v. 21, n. 1, p. 109. Basel: MDPI, 2016. Disponível em: https://www.mdpi.com/1420-3049/21/1/109. Acesso em: 30 set. 2021.

105 FATHI, P. *et al*. Zeolite ‐ loaded alginate ‐ chitosan hydrogel beads as a topical hemostat. **Journal of Biomedical Materials Research Part B: Applied Biomaterials,** v. 106, n. 5, p. 1662-1671. New Jersey: Wiley, 2018. Disponível em: https://onlinelibrary.wiley.com/doi/10.1002/jbm.b.33969. Acesso em: 30 set. 2021.

106 MAHMODI, G. *et al*. From microporous to mesoporous mineral frameworks: An alliance between zeolite and chitosan. **Carbohydrate Research,** v. 489, p. 107930. Amsterdam: Elsevier, 2020. https://www.sciencedirect.com/science/article/abs/pii/S0008621519306834. Acesso em: 30 ago. 2021.

107 WAN NGAH, W. *et al*. Preparation and characterization of chitosan–zeolite composites. **Journal of applied polymer science,** v. 125, n. 3, p. 2417-2425. New Jersey: Wiley, 2012. Disponível em: https://onlinelibrary.wiley.com/doi/10.1002/app.36503. Acesso em: 30 ago. 2021.

108 PAKDEL, P.M.; PEIGHAMBARDOUST, S.J. Review on recent progress in chitosan-based hydrogels for wastewater treatment application. **Carbohydrate polymers,** v. 201, p. 264-279. Amsterdam: Elsevier, 2018. Disponível em: https://www.sciencedirect.com/science/article/abs/pii/S0144861718309809. Acesso em: 01 ago. 2021.

109 DRAGAN, E.S.; DINU, M.V. Advances in porous chitosan-based composite hydrogels: Synthesis and applications. **Reactive and Functional Polymers,** v. 146, p. 104372. Amsterdam: Elsevier, 2020. Disponível em: https://www.sciencedirect.com/science/article/abs/pii/S1381514819308132. Acesso em: 02 set. 2021.

110 AL-MANHEL, A.J.; AL-HILPHY, A.R.S.; NIAMAH, A.J. Extraction of chitosan, characterisation and its use for water purification. **Journal of the Saudi Society of agricultural sciences,** v. 17, n. 2, p. 186-190. Amsterdam: Elsevier, 2018. Disponível em:

https://www.sciencedirect.com/science/article/pii/S1658077X16300224?via%3Dihub. Acesso em: 02 set. 2021.

111 LUO, Q. *et al*. Comparison of the physicochemical, rheological, and morphologic properties of chitosan from four insects. **Carbohydrate Polymers,** v. 209, p. 266-275. Amsterdam: Elsevier, 2019. Disponível em: https://www.sciencedirect.com/science/article/abs/pii/S0144861719300438. Acesso em: 02 set. 2021.

112 KASIRI, M.B. 14 - Application of chitosan derivatives as promising adsorbents for treatment of textile wastewater. In: **The Impact and Prospects of Green Chemistry for Textile Technology**. Sawston: Woodhead Publishing, 2019. p.417-469. Disponível em: https://www.sciencedirect.com/science/article/pii/B9780081024911000149. Acesso em: 14 jan. 2021.

113 SHOUEIR, K.R. *et al*. Chitosan based-nanoparticles and nanocapsules: Overview, physicochemical features, applications of a nanofibrous scaffold, and bioprinting. **International Journal of Biological Macromolecules,** v. 167, p. 1176-1197. Amsterdam: Elsevier, 2021. https://www.sciencedirect.com/science/article/abs/pii/S0141813020349977?via%3Dihub. Acesso em: 14 jan. 2021.

114 GONG, Y. *et al*. Synthesis and Characterization of Graphene Oxide/Chitosan Composite Aerogels with High Mechanical Performance. **Polymers,** v. 11, n. 5. Basel: MDPI, 2019. Disponível em: https://www.mdpi.com/2073-4360/11/5/777. Acesso em: 14 jan. 2021.

115 LIPATOVA, I.M. *et al*. Gelation in solutions of low deacetylated chitosan initiated by high shear stresses. **International Journal of Biological Macromolecules,** v. 139, p. 550-557. Amsterdam: Elsevier, 2019. Disponpivel em: https://pubmed.ncbi.nlm.nih.gov/31356948/. Acesso em: 14 jan. 2021.

116 FACCHINATTO, W.M. *et al*. Evaluation of chitosan crystallinity: A high-resolution solid-state NMR spectroscopy approach. **Carbohydrate Polymers,** v. 250. Amsterdam: Elsevier, 2020. Disponível em: https://reader.elsevier.com/reader/sd/pii/S014486172031064X?token=3211AC79BA115DD4BEE0D733070AAAFF1FEA625891645DCF6C47A642291AAE38F3FF1B18957DA2C00376876098E41CB3&originRegion=us-east-1&originCreation=20220902104808. Acesso em: 01 set. 2021.

117 GATTO, M. *et al*. Study of chitosan with different degrees of acetylation as cardboard paper coating. **Carbohydrate Polymers,** v. 210, p. 56-63. Amsterdam: Elsevier, 2019. Disponível em: https://www.sciencedirect.com/science/article/pii/S0144861719300669. Acesso em: 01 set. 2021.

118 LU, H.T. *et al.* Development of genipin-crosslinked and fucoidan-adsorbed nano-hydroxyapatite/hydroxypropyl chitosan composite scaffolds for bone tissue engineering. **International Journal of Biological Macromolecules,** v. 128, p. 973-984. Amsterdam:

Elsevier, 2019. Disponível em: https://www.sciencedirect.com/science/article/abs/pii/S0141813018366078. Acesso em: 02 set. 2021.

119 CHEN, Y. *et al*. Graphene oxide–chitosan composite hydrogels as broad-spectrum adsorbents for water purification. **Journal of Materials Chemistry A,** v. 1, n. 6, p. 1992-2001. Cambridge: RSC Publishing, 2013. Disponível em: https://pubs.rsc.org/en/content/articlelanding/2013/ta/c2ta00406b. Acesso em: 02 set. 2021.

120 MOHAMED, N.; MADIAN, N.G. Enhancement of the dynamic mechanical properties of chitosan thin films by crosslinking with greenly synthesized silver nanoparticles. **Journal of Materials Research and Technology,** v. 9, n. 6, p. 12970-12975. Amsterdam: Elsevier, 2020. Disponível em: https://www.sciencedirect.com/science/article/pii/S223878542031749X?via%3Dihub. Acesso em: 05 aug. 2021.

121 AMONI, B.C. *et al*. Effect of coal fly ash treatments on synthesis of high-quality zeolite A as a potential additive for warm mix asphalt. **Materials Chemistry and Physics,** v. 275, p. 125197. Amsterdam: Elsevier, 2022. Disponível em: https://www.sciencedirect.com/science/article/pii/S0254058421009809. Acesso em: 23 nov. 2021.

122 ROBSON, H. **Verified synthesis of zeolitic materials**. Amsterdam: Gulf Professional Publishing, 2001. Disponível em: https://www.sciencedirect.com/book/9780444507037/verified-syntheses-of-zeolitic-materials. Acesso em: 15 jul. 2021.

123 NASTI, A. *et al*. Chitosan/TPP and chitosan/TPP-hyaluronic acid nanoparticles: systematic optimisation of the preparative process and preliminary biological evaluation. **Pharmaceutical research,** v. 26, n. 8, p. 1918-1930. New York: Springer, 2009. Disponível em: https://link.springer.com/article/10.1007/s11095-009-9908-0. Acesso em: 15 jul. 2021.

124 SONG, W. *et al.* Preparation of Freeze-Dried Porous Chitosan Microspheres for the Removal of Hexavalent Chromium. **Applied Sciences-Basel,** v. 11, n. 9, p. 19. Basel: MDPI, 2021. Disponível em: https://www.mdpi.com/2076-3417/11/9/4217. Acesso em: 22 jul. 2021.

125 MONTEIRO, A.A.S. **Microesferas flutuantes e não flutuantes à base de goma do cajueiro e quitosana como potencial matriz para liberação de fármacos**. 2013. 168 p. (Doctorate). Organic and Inorganic Chemistry Department, Federal University of Ceará, Fortaleza.

126 DENEYER, A. *et al*. Zeolite Synthesis under Nonconventional Conditions: Reagents, Reactors, and Modi Operandi. **Chemistry of Materials,** v. 32, n. 12, p. 4884-4919. Washington: ACS Publications, 2020. Disponível em: https://pubs.acs.org/doi/10.1021/acs.chemmater.9b04741. Acesso em: 29 dez. 2021.

127 YADAV, V.K. *et al*. A Short Review on the Utilization of Incense Sticks Ash as an Emerging and Overlooked Material for the Synthesis of Zeolites. **Crystals,** v. 11, n. 10, p. 1255. Basel:

MDPI 2021. Disponível em: https://www.mdpi.com/2073-4352/11/10/1255. Acesso em: 29 dez. 2021.

128 LÄNGAUER, D. *et al*. Preparation of Synthetic Zeolites from Coal Fly Ash by Hydrothermal Synthesis. **Materials,** v. 14, n. 5, p. 1267. Basel: MDPI, 2021. Disponível em: https://www.mdpi.com/1996-1944/14/5/1267. Acesso em: 29 dez. 2021.

129 HUSSAIN, S. *et al*. Adsorption, kinetics and thermodynamics studies of methyl orange dye sequestration through chitosan composites films. **International Journal of Biological Macromolecules,** v. 168, p. 383-394. Amsterdam: Elsevier, 2021. Disponível em: https://www.sciencedirect.com/science/article/abs/pii/S0141813020352120. Acesso em: 05 aug. 2021.

130 PAULA, H.C. *et al*. Eco-friendly synthesis of an alkyl chitosan derivative. **International Journal of Biological Macromolecules,** v. 163, p. 1591-1598. Amsterda: Elsevier, 2020. Disponível em: https://www.sciencedirect.com/science/article/pii/S0141813020341386. Acesso em: 05 aug. 2021.

131 MA, G. *et al*. Synthesis and properties of photosensitive chitosan derivatives (1). **International Journal of Biological Macromolecules,** v. 46, n. 5, p. 558-561. Amsterdam: Elsevier, 2010. Disponível em: https://www.sciencedirect.com/science/article/abs/pii/S0141813010000590. Acesso em: 05 aug. 2021.

132 JIAO, T.F. *et al*. Synthesis and characterization of chitosan-based Schiff base compounds with aromatic substituent groups. **Carbohydrate Polymers**, v. 145, p. 37-47. Amsterdam: Elsevier, 2011. Disponível em: https://www.sciencedirect.com/science/article/abs/pii/S0144861716301412. Acesso em: 05 aug. 2021.

133 QIAO, C. *et al*. Structure and properties of chitosan films: Effect of the type of solvent acid. **Lwt,** v. 135, p. 109984. Amsterdam: Elsevier, 2021. Disponível em: https://www.sciencedirect.com/science/article/abs/pii/S0023643820309737. Acesso em: 05 aug. 2021.

134 SAMUELS, R.J. Solid state characterization of the structure of chitosan films. **Journal of polymer science: polymer physics edition,** v. 19, n. 7, p. 1081-1105. New Jersey: John Wiley & Sons, 1981. Disponível em: https://onlinelibrary.wiley.com/doi/10.1002/pol.1981.180190706. Acesso em: 05 aug. 2021.

135 SARKAR, A. *et al*. A comprehensive characterisation of fly ash from a thermal power plant in Eastern India. **Fuel Processing Technology,** v. 87, n. 3, p. 259-277. Amsterdam: Elsevier, 2006. Disponível em: https://www.sciencedirect.com/science/article/pii/S0378382005001670. Acesso em: 10 jan. 2022.

136 MUTHU PRABHU, S.; MEENAKSHI, S. Enriched fluoride sorption using chitosan supported mixed metal oxides beads: Synthesis, characterization and mechanism. **Journal of Water Process Engineering,** v. 2, p. 96-104, 2014/06/01/ 2014. Disponível em:

https://www.sciencedirect.com/science/article/pii/S2214714414000439. Acesso em: 28 dez. 2021.

137 HASAN, K. *et al*. Magnetic Chitosan-Supported Silver Nanoparticles: A Heterogeneous Catalyst for the Reduction of 4-Nitrophenol. **Catalysts,** v. 9, n. 10, p. 839, 2019. ISSN 2073-4344. Disponível em: https://www.mdpi.com/2073-4344/9/10/839. Acesso em: 28 dez. 2021.

138 PAWLAK, A.;M. MUCHA. Thermogravimetric and FTIR studies of chitosan blends. **Thermochimica acta,** v. 396, n. 1-2, p. 153-166. Amsterdam: Elsevier, 2003. Disponível em: https://www.sciencedirect.com/science/article/abs/pii/S0040603102005233. Acesso em: 28 dez. 2021.

139 ALI, N. *et al*. Chitosan-based green sorbent material for cations removal from an aqueous environment. **Journal of Environmental Chemical Engineering**, p. 104064. Amsterdam: Elsevier, 2020. Disponível em: https://www.sciencedirect.com/science/article/abs/pii/S2213343720304127. Acesso em: 29 dez. 2021.

140 MELO, M.N. *et al*. Immobilization and characterization of horseradish peroxidase into chitosan and chitosan/PEG nanoparticles: A comparative study. **Process Biochemistry,** v. 98, p. 160-171. Amsterdam: Elsevier, 2020. Disponível em: https://www.sciencedirect.com/science/article/abs/pii/S1359511320310886. Acesso em: 29 dez. 2021.

141 COURA, J.C.;PROFETI, D.; PROFETI, L.P.R. Eco-friendly chitosan/quartzite composite as adsorbent for dye removal. **Materials Chemistry and Physics,** v. 256, p. 123711. Amsterdam: Elsevier, 2020. Disponível em: https://www.sciencedirect.com/science/article/abs/pii/S0254058420310713?via%3Dihub. Acesso em: 28 dez. 2021.

142 KAYA, M. *et al*. Extraction and characterization of α-chitin and chitosan from six different aquatic invertebrates. **Food biophysics,** v. 9, n. 2, p. 145-157. New York: Springer, 2014. Disponível em: https://link.springer.com/article/10.1007/s11483-013-9327-y. Acesso em: 28 dez. 20021.

143 CHAGAS, P.M.B.C. *et al*. Nanostructured oxide stabilized by chitosan: Hybrid composite as an adsorbent for the removal of chromium (VI). **Journal of Environmental Chemical Engineering,** v. 6, p. 1008-1019. Amsterdam: Elsevier, 2018. Disponível em: https://www.sciencedirect.com/science/article/abs/pii/S2213343718300265. Acesso em: 29 dez. 2021.

144 HUANG, J. *et al*. Facile preparation of a strong chitosan-silk biocomposite film. **Carbohydrate polymers,** v. 229, p. 115515. Amsterdam: Elsevier, 2020. Disponível em: https://www.sciencedirect.com/science/article/abs/pii/S014486171931183X. Acesso em: 30 dez. 2021.

145 GU, Z. *et al*. Preparation of chitosan/silk fibroin blending membrane fixed with alginate dialdehyde for wound dressing. **International journal of biological macromolecules,** v. 58, p. 121-126. Amsterdam: Elsevier, 2013. Disponível em: https://www.sciencedirect.com/science/article/abs/pii/S0141813013001591. Acesso em: 02 jan. 2022.

146 KAZANCIOGLU, M. *et al*. FTIR studies on plasticization of silicate glass with ionic liquids (conversion to silicate polymers). **Journal of Non-Crystalline Solids,** v. 561, p. 120757. Amsterdam: Elsevier, 2021. Disponível em: https://www.sciencedirect.com/science/article/pii/S0022309321001162. Acesso em: 09 jan. 2022.

147 ALKAN, M. *et al*. The effect of alkali concentration and solid/liquid ratio on the hydrothermal synthesis of zeolite NaA from natural kaolinite. **Microporous and Mesoporous Materials,** v. 86, n. 1-3, p. 176-184. Amsterdam: Elsevier, 2005. Disponível em: https://www.sciencedirect.com/science/article/abs/pii/S138718110500291X. Acesso em: 03 jan. 2022.

148 MOISÉS, M.P. *et al*. Synthesis of zeolite NaA from sugarcane bagasse ash. **Materials Letters,** v. 108, p. 243-246. Amsterdam: Elsevier, 2013. Disponível em: https://www.sciencedirect.com/science/article/abs/pii/S0167577X13008975?via%3Dihub. Acesso em: 03 jan. 2022.

149 SAPAWE, N. *et al*. Cost-effective microwave rapid synthesis of zeolite NaA for removal of methylene blue. **Chemical Engineering Journal,** v. 229, p. 388-398. Amsterdam: Elsevier, 2013. Disponível em: https://www.sciencedirect.com/science/article/abs/pii/S1385894713007651. Acesso em: 05 jan. 2022.

150 HAN, X. *et al*. Facile synthesis of mesoporous silica derived from iron ore tailings for efficient adsorption of methylene blue. **Colloids and Surfaces A: Physicochemical and Engineering Aspects**, p. 126391. Amsterdam: Elsevier, 2021. Disponível em: https://www.sciencedirect.com/science/article/abs/pii/S0927775721002600. Acesso em: 04 jan. 2022.

151 LEKGOBA, T.; NTULI, F.; FALAYI, T. Application of coal fly ash for treatment of wastewater containing a binary mixture of copper and nickel. **Journal of Water Process Engineering**, p. 101822. Amsterdam: Elsevir, 2020. Disponível em: Application of coal fly ash for treatment of wastewater containing a binary mixture of copper and nickel - ScienceDirect. Acesso em: 02 jan. 2022.

152 YADAV, M. *et al*. Mechanical properties of Fe3O4/GO/chitosan composites. **Composites: Part B,** v. 66, p. 89-96. Amsterdam: Elsevier, 2014. Disponível em: https://www.sciencedirect.com/science/article/abs/pii/S1359836814001905. Acesso em: 30 ago. 2021.

153 GORDINA, N.E. *et al*. Synthesis of granulated binder-free LTA zeolite from metakaolin using ultrasonic treatment. **Journal of Porous Materials,** v. 24, n. 3, p. 667-678. New York:

Springer, 2017. Disponível em: https://link.springer.com/article/10.1007/s10934-016-0303-z. Acesso em: 30 dez. 2021.

154 GENG, H. *et al*. Rapid and efficient synthesis of CHA-type zeolite by interzeolite conversion of LTA-type zeolite in the presence of N, N, N-trimethyladamantammonium hydroxide. **Journal of Solid State Chemistry,** v. 265, p. 193-199. Amsterdam: Elsevier, 2018. Disponível em: https://www.sciencedirect.com/science/article/abs/pii/S0022459618302457. Acesso em: 02 fev. 2021.

155 LI, M. *et al*. Coal-fly-ash magnetic sphere based magnetic adsorbent for multiple-dye adsorption. **Materials Research Express,** v. 8, n. 1. Philadelphia: IOP Publishing, 2021. Disponível em: https://iopscience.iop.org/article/10.1088/2053-1591/abd6a2/meta. Acesso em: 10 jan. 2022.

156 VALEEV, D. *et al*. Magnetite and Carbon Extraction from Coal Fly Ash Using Magnetic Separation and Flotation Methods. **Minerals,** v. 9, n. 5, p. 320. Basel: MDPI, 2019. Disponível em: https://www.mdpi.com/2075-163X/9/5/320. Acesso em: 10 jan. 2022.

157 FREITAS, A.D.L. **Zeólitas A, Y, Chabazita e seus compósitos magnéticos sintetizados a partir de cinzas volantes**. 62 p. (Master's Degree). Departamento de Química Orgânica e Inorgânica, Universidade Federal do Ceará, Fortaleza, 2019.

158 CZUMA, N. *et al*. **The process of fly ash magnetic separation impact on hydrothermal synthesis of zeolites**. E3S Web of Conferences: EDP Sciences, 2016. 00009 p. Disponível em: https://www.e3s-conferences.org/articles/e3sconf/abs/2016/05/e3sconf_seed2016_00009/e3sconf_seed2016_00009.html. Acesso em: 03 jan. 2021.

159 VALEEV, D. *et al*. Magnetite and Carbon Extraction from Coal Fly Ash Using Magnetic Separation and Flotation Methods. **Minerals,** v. 9, n. 5. Basel: MDPI, 2019. Disponível em: https://www.mdpi.com/2075-163X/9/5/320. Acesso em: 10 jan. 2022.

160 WANG, X.S. Mineralogical and chemical composition of magnetic fly ash fraction. **Environmental Earth Sciences,** v. 71, n. 4, p. 1673-1681. New York: Springer, 2014. Disponível em: https://link.springer.com/article/10.1007/s12665-013-2571-0. Acesso em: 10 jan. 2022.

161 VU, D.-H. *et al*. Composition and Morphology Characteristics of Magnetic Fractions of Coal Fly Ash Wastes Processed in High-Temperature Exposure in Thermal Power Plants. **Applied Sciences,** v. 9, n. 9, p. 1964. Basel: MDPI, 2019. Disponível em: https://www.mdpi.com/2076-3417/9/9/1964. Acesso em: 10 jan. 2022.

162 PETRUS, H.T.B.M. *et al*. Cenospheres characterization from Indonesian coal-fired power plant fly ash and their potential utilization. **Journal of Environmental Chemical Engineering,** v. 8, n. 5, p. 104116, 2020/10/01/ 2020. ISSN 2213-3437. Disponível em: https://www.sciencedirect.com/science/article/pii/S2213343720304644. Acesso em: 10 jan. 2022.

163 AMONI, B.C. *et al*. A method for NaA zeolite synthesis from coal fly ash and its application in warm mix asphalt. **Road Materials and Pavement Design,** v. 20, n. sup2, p. S558-S567. London: Taylor & Francis Group, 2019. Disponível em: https://www.tandfonline.com/doi/abs/10.1080/14680629.2019.1633766?journalCode=trmp20. Acesso em: 11 jan. 2022.

164 PATEL, N.K.; SINHA, V.K. Synthesis, Characterization and Optimization of Water-Soluble Chitosan Derivatives. **International Journal of Polymeric Materials and Polymeric Biomaterials,** v. 58, n. 11, p. 548-560. London: Taylor & Francis Group, 2009. Disponível em: https://www.tandfonline.com/doi/abs/10.1080/00914030903035394. Acesso em: 11 jan. 2022.

165 REKIK, S.B. *et al*. Development and characterization of porous membranes based on kaolin/chitosan composite. **Applied Clay Science,** v. 143, p. 1-9. Amsterdam: Elsevier, 2017. Disponível em: https://www.sciencedirect.com/science/article/pii/S0169131717301096. Acesso em: 11 jan. 2022.

166 RUBINA, M.S. *et al*. Chitosan aerogel containing silver nanoparticles: From metal-chitosan powder to porous material. **Polymer Testing,** v. 86, p. 106481. Amsterdam: Elsevier, 2020. 0142-9418. Disponível em: https://www.sciencedirect.com/science/article/pii/S0142941819322093. Acesso em: 11 jan. 2022.

167 ZHU, C. *et al*. Effects of Chitosan on Properties of Novel Human-like Collagen/Chitosan Hybrid Vascular Scaffold. **Journal of Bioactive and Compatible Polymers,** v. 24, n. 6, p. 560-576. Thousand Oaks: Sage Journals, 2009. Disponível em: https://doi.org/10.1177/0883911509349689. Acesso em: 11 jan. 2022.

168 MO, H. *et al*. Porous biochar/chitosan composites for high performance cellulase immobilization by glutaraldehyde. **Enzyme and Microbial Technology,** v. 138, p. 109561, 2020/08/01/ 2020. Disponível em: https://www.sciencedirect.com/science/article/pii/S0141022920300545. Acesso em: 11 jan. 2022.

169 FRICK, J.M. *et al*. Influence of Glutaraldehyde Crosslinking and Alkaline Post-treatment on the Properties of Chitosan-Based Films. **Journal of Polymers and the Environment,** v. 26, n. 7, p. 2748-2757. United States of America: OSTI, 2018. Disponível em: https://www.osti.gov/biblio/22788085. Acesso em: 04 dez. 2021.

170 EL-SAYED, E.M. *et al*. Development of novel chitosan schiff base derivatives for cationic dye removal: methyl orange model. **Desalination and Water Treatment,** v. 57, n. 47, p. 22632-22645. London: Taylor & Francis Group, 2016. Disponível em: https://www.tandfonline.com/doi/abs/10.1080/19443994.2015.1136694?journalCode=tdwt20. Acesso em: 04 dez. 2021.

171 LOPEZ, F.A. *et al*. A kinetic study on the thermal behaviour of chitosan. **Journal of Thermal Analysis and Calorimetry,** v. 91, n. 2, p. 633-639. New York: Springer, 2008.

Disponível em: https://link.springer.com/article/10.1007/s10973-007-8321-3. Acesso em: 04 dez. 2021.

172 VILLAR-CHAVERO, M.M. *et al*. Thermal and kinetics of the degradation of chitosan with different deacetylation degrees under oxidizing atmosphere. **Thermochimica Acta,** v. 670, p. 18-26. Amsterdam: Elsevier, 2018. Disponível em: https://www.sciencedirect.com/science/article/pii/S0040603118305033. Acesso em: 04 dez. 2021.

173 JAYANUDIN, *et al*. Preparation of Chitosan Microcapsules Containing Red Ginger Oleoresin Using Emulsion Crosslinking Method. **Journal of Applied Biomaterials & Functional Materials,** v. 17, n. 1. Thousand Oaks: Sage Journals, 2019. Disponível em: https://pubmed.ncbi.nlm.nih.gov/30803278/. Acesso em: 04 dez. 2021.

174 GEBRETSADIK, T.T.; GEBREMEDHIN, T. K. Structural studies of natural zeolites and optimizations for water hardness softening media. **Journal of Metals Materials and Minerals,** v. 30, n. 1, p. 109-118. Tailândia: https://www.scimagojr.com/journalsearch.php?q=Chulalongkorn%20University&tip=pub, 2020. Disponível em: https://pdfs.semanticscholar.org/38f5/9a4105b184e838af37e967227427933e36ef.pdf?_ga=2.99272854.980582300.1661815229-560661047.1655311761. Acesso em: 05 dez. 2021.

175 CASTRO, P.R.D.; MAIA, A.A.B.; ANGELICA, R.S. Study of the Thermal Stability of Faujasite Zeolite Synthesized from Kaolin Waste from the Amazon. **Materials Research-Ibero-American Journal of Materials,** v. 22, n. 5. Johanesburgo: Scielo, 2019. Disponível em: https://www.scielo.br/j/mr/a/Pv7JvCzBs4zT8VfRnVsyfZq/. Acesso em: 05 dez. 2021.

176 NGAH, W.S.W. *et al*. Preparation and characterization of chitosan-zeolite composites. **Journal of Applied Polymer Science,** v. 125, n. 3, p. 2417-2425. New Jersey: Springer, 2012. Disponível em: https://link.springer.com/content/pdf/10.1007/s10973-015-5227-3.pdf. Acesso em: 04 dez. 2021.

177 LAL, S.;ARORA, S.; SHARMA, C. Synthesis, thermal and antimicrobial studies of some Schiff bases of chitosan. **Journal of Thermal Analysis and Calorimetry,** v. 124, n. 2, p. 909-916. Thousand Oaks: Sage Publishing, 2016. Disponível em: https://journals.sagepub.com/doi/10.1177/2280800018809917. Acesso em: 04 dez. 2021.

178 GHOSH, A.; MA, L.; GAO, C.Y. Zeolite molecular sieve 5A acts as a reinforcing filler, altering the morphological, mechanical, and thermal properties of chitosan. **Journal of Materials Science,** v. 48, n. 11, p. 3926-3935. New Jersey: Springer, 2013. Disponível em: https://link.springer.com/article/10.1007/s10853-013-7194-z. Acesso em: 04 dez. 2021.

179 WANG, J. *et al*. Effect of zeolites on chitosan/zeolite hybrid membranes for direct methanol fuel cell. **Journal of Power Sources,** v. 178, n. 1, p. 9-19. Amsterdam: Elsevier, 2008. Disponível em: https://www.sciencedirect.com/science/article/pii/S0378775307027693. Acesso em: 04 dez. 2021.

180 PRASAD, C.V. *et al*. Preparation and characterization of 4A zeolite-filled mixed matrix membranes for pervaporation dehydration of isopropyl alcohol. **Journal of Applied Polymer Science,** v. 121, n. 3, p. 1521-1529. New Jersey: Wiley, 2011. Disponível em: https://doi.org/10.1002/app.33688. Acesso em: 04 dez. 2021.

181 SHAFIEE, M. *et al*. Effect of zeolite hydroxyl active site distribution on adsorption of Pb(II) and Ni(II) pollutants from water system by polymeric nanofibers. **Separation Science and Technology,** v. 55, n. 11, p. 1994-2011. London: Taylor & Francis Group, 2020. Disponível em: https://www.tandfonline.com/doi/abs/10.1080/01496395.2019.1624572. Acesso em: 04 dez. 2021.

182 SONG, M.M. *et al*. Research on WPU-RGO/ATP-Fe3O4/chitosan composites with excellent electrical and magnetic properties. **Polymers for Advanced Technologies,** v. 31, n. 5, p. 1164-1171. New Jersey: Wiley, 2020. Disponível em: https://onlinelibrary.wiley.com/doi/10.1002/pat.4850. Acesso em: 04 dez. 2021.

183 HUANG, L. *et al*. Facile preparation of taurine modified magnetic chitosan nanocomposites as biodegradable adsorbents toward methylene blue. **Environmental Technology,** v. 42, n. 20, p. 3191-3204. Taylor & Francis Group, 2021. Disponível em: https://pubmed.ncbi.nlm.nih.gov/32003648/. Acesso em: 04 dez. 2021.

184 PERALTA, M.E. *et al*. Highly efficient removal of heavy metals from waters by magnetic chitosan-based composite. **Adsorption-Journal of the International Adsorption Society,** v. 25, n. 7, p. 1337-1347. Amsterdam: Elsevier, 2019. Disponível em: https://link.springer.com/article/10.1007/s10450-019-00096-4. Acesso em: 04 dez. 2021.

185 MANDAVINASAB, M.; HAMZEHLOUEIAN, M.; SARRAFI, Y. Preparation and application of magnetic chitosan/graphene oxide composite supported copper as a recyclable heterogeneous nanocatalyst in the synthesis of triazoles. **International Journal of Biological Macromolecules,** v. 138, p. 764-772. Amsterdam: Elsevier, 2019. Disponível em: https://www.sciencedirect.com/science/article/pii/S0141813019331071?via%3Dihub. Acesso em: 04 dez. 2021.

186 ADEYEYE, A.O.; SHIMON, G. Chapter 1 - Growth and Characterization of Magnetic Thin Film and Nanostructures. *In*: **Handbook of Surface Science**: North-Holland, v.5, p.1-41. Amsterdam: Elsevier, 2015. Disponível em: https://www.sciencedirect.com/science/article/abs/pii/B9780444626349000011. Acesso em: 23 nov. 2021.

187 SHOUMKOVA, A.S. Magnetic separation of coal fly ash from Bulgarian power plants. **Waste Management & Research, v. 29, n. 10, p. 1078-1089.** Thousand Oaks: Sage Journals, 2011. Disponível em: https://journals.sagepub.com/doi/10.1177/0734242X10379494. Acesso em: 19 dez. 2021.

188 TONG, R. *et al*. Study of preparation and properties on polymer-modified magnetite nanoparticles. **South African Journal of Chemistry,** v. 68, n. 0, p. 99-104. Johanesburgo: Scielo, 2015. Disponível em:

http://www.scielo.org.za/scielo.php?script=sci_arttext&pid=S0379-43502015000100015. Acesso em: 27 dez. 2021.

189 BESSA, R. A. *et al*. Kaolin-based magnetic zeolites A and P as water softeners. **Microporous and Mesoporous materials,** v. 245, p. 64-72. Amsterdam: Elsevier, 2017. Disponível em: https://www.sciencedirect.com/science/article/pii/S1387181117301610. Acesso em: 02 dez. 2021.

190 LOIOLA, A. *et al*. Structural analysis of zeolite NaA synthesized by a cost-effective hydrothermal method using kaolin and its use as water softener. **Journal of colloid and interface science,** v. 367, n. 1, p. 34-39. Amsterdam: Elsevier, 2012. Disponível em: https://www.sciencedirect.com/science/article/pii/S0021979710013044. Acesso em: 30 dez. 2021.

191 SAGAN, C. **O mundo assombrado pelos demônios**: a ciência vista como uma vela no escuro. 509 p. São Paulo: Companhia das Letras, 2006.